Aβ Amyloid Scaffolds the Accumulation of Matrisome and Additional Proteins in Alzheimer's Disease.

Yona Levites*[1,4,5], Eric B. Dammer*[2,4,5], Yong Ran[1,4,5], Wangchen Tsering[6,7,8], Duc Duong[2,4,5], Measho Abreha[2,4,5], Joshna Gadhavi[2,4,5], Kiara Lolo[6,7,8], Jorge Trejo-Lopez[6,7,8], Jennifer Phillips[6,7,8], Andrea Iturbe, Aya Erquizi, Brenda D. Moore[1,4,5], Danny Ryu[1,4,5], Aditya Natu[2,4,5], Kristy Dillon[7,8,9], Jose Torrellas[7,8,9], Corey Moran[7,8,9], Thomas Ladd [7,8], Farhana Afroz[1,4,5], Tariful Islam[1,4,5], Jaishree Jagirdar[13], Cory C. Funk[14], Max Robinson[14], David R. Borchelt[7,8,9], Nilüfer Ertekin-Taner[11, 12], Jeffrey W. Kelly[15], Frank L. Heppner[16], Erik C. B. Johnson[3,4,5], Karen McFarland[1,4,5], Allan I. Levey[3,4,5,] Stefan Prokop**[6,7,8], Nicholas T. Seyfried**[2,4,5],Todd E. Golde**[1,3,4,5].

[1]Department of Pharmacology and Chemical Biology, School of Medicine, Emory University, Atlanta, GA, USA.
[2]Department of Biochemistry, School of Medicine, Emory University, Atlanta, GA, USA.
[3]Department of Neurology, School of Medicine, Emory University, Atlanta, GA, USA.
[4]Goizueta Brain Health Institute and Alzheimer's Disease Research Center, Emory University School of Medicine, Atlanta, GA, USA.
[5]Center for Neurodegenerative Disease Center, Emory University School of Medicine, Atlanta, GA, USA.
[6]Department of Pathology, College of Medicine, University of Florida, Gainesville, USA.
[7]Evelyn F. and William L. McKnight Brain Institute, University of Florida, Gainesville, Fl, USA.
[8]Center for Translational Research in Neurodegenerative Disease, University of Florida, Gainesville, Fl, USA.
[9]Department of Neuroscience, College of Medicine, University of Florida, Gainesville, USA.
[10]Department of Neurology, College of Medicine, University of Florida, Gainesville, USA
[11]Mayo Clinic, Department of Neuroscience, Jacksonville, FL, USA.
[12]Mayo Clinic, Department of Neurology, Jacksonville, FL, USA.
[13]Department of Pathology and Laboratory Medicine, Emory University Hospital. Atlanta, GA, USA.
[14]Institute for Systems Biology, Seattle, WA, USA.
[15]Department of Chemistry and The Skaggs Institute for Chemical Biology, The Scripps Research Institute, La Jolla, California, USA.
[16]Department of Neuropathology, Charité – Universitätsmedizin Berlin, corporate member of Freie Universität Berlin and Humboldt-Universität zu Berlin; German Center for Neurodegenerative Diseases (DZNE) Berlin; Cluster of Excellence, NeuroCure, Charitéplatz 110117 Berlin, Germany.

* These authors contributed equally
** Address correspondence to tgolde@emory.edu; nseyfri@emory.edu and sprokop@ufl.edu.

Keywords: proteomics, Alzheimer's disease, amyloid, models, plaques, aggregation

Running Title: Amyloid Scaffolds the Matrisome

Abstract

We report a highly significant correlation between human Alzheimer's disease (AD) brain proteome changes and those in CRND8 $APP_{695NL/F}$ transgenic mice. Comparing protein changes observed in the CRND8 mice with co-expression networks derived from human Alzheimer's disease (AD), reveals both conserved and divergent module changes. Many proteins in the most highly conserved module (M42, matrisome) accumulate in plaques, cerebrovascular amyloid (CAA), dystrophic neuronal processes, or a combination thereof. Overexpression of two M42 proteins, midkine (Mdk) and pleiotrophin (PTN), in CRND8 mice brains leads to increased accumulation of Aβ in plaques and in blood vessels; further, recombinant MDK and PTN enhance Aβ aggregation into amyloid structures. Multiple M42 proteins bind to fibrillar Aβ42 and a non-human amyloid fibril *in vitro*. Supporting this binding data, MDK and PTN co-accumulate with transthyretin (TTR) amyloid in the heart. Notably, our findings establish that proteomic changes in modules observed in human AD brains define an Aβ amyloid "responsome" that is well conserved from mouse models to humans. Further, distinct amyloid structures appear to serve as scaffolds, facilitating the co-accumulation of proteins with signaling functions, and this co-accumulation may contribute to downstream pathological sequalae. Overall, this contextualized understanding of proteomic changes and their interplay with amyloid deposition provides valuable insights into the complexity of AD pathogenesis and potential biomarkers and therapeutic targets.

INTRODUCTION

The amyloid cascade hypothesis (ACH) serves as a foundational framework for comprehending the pathogenesis of Alzheimer's disease (AD) [1,2]. Recent evidence from anti-amyloid immunotherapies, developed based on this hypothesis, offers the initial therapeutic validation, affirming the central tenet that Aβ deposition plays a role in the AD pathogenic cascade [3-5]. These antibodies target the early symptomatic phase of AD demonstrating robust reductions in brain Aβ amyloid, slowing AD decline, but not halting or reversing it. Collectively, these findings reinforce the previously proposed notion within the field that, by the time symptoms manifest, the influence of amyloid itself is limited, while additional pathologies may become self-reinforcing or irreversible [6].

Despite extensive investigation, significant gaps in our understanding of AD pathogenesis remain [2,7,8]. The initial notion of a purely linear amyloid cascade, whereby Aβ amyloid deposition in sequence triggers neurofibrillary tau pathology, neuronal degeneration, immune responses, and clinical AD symptoms, is now recognized as overly simplistic. Studies utilizing proteomic, transcriptomic, metabolomic, pathological, and biomarker approaches have unveiled the intricate complexity of changes occurring over decades in the brains of individuals as various AD hallmark pathologies emerge [7,9-24]. These investigations reveal potentially non-linear and multifaceted alterations that affect all major cell-types in the brain, ultimately resulting in regional and widespread organ failure.

At a systems-level, these pathological and cellular changes manifest as fluctuations in protein levels, transcript quantities, and metabolite concentrations, even in brain regions where significant pathology may not be apparent [13]. This further underscores the complexity of AD pathogenesis and highlights the need to consider diverse factors contributing to disease progression beyond the core proteins implicated by the ACH or genetic studies. Comprehensive analyses incorporating multi-omic datasets such as those generated by the Accelerating Medicine Partnership for AD (AMP-AD) and other consortiums provide crucial insights into the systems pathobiology of AD, enabling a more nuanced comprehension of the disease's dynamic processes occurring at the cellular and molecular [7,9-24].

Typically, systems-level omic studies alone cannot establish cause and effect relationships. However, by combining strong correlational inference with omics obtained from different AD stages, we can generate hypotheses regarding causality or the role of these changes in the disease. To determine whether these omic-level changes are a consequence of disease or play a more fundamental role in pathogenesis, it is essential to i) compare the data across related disorders and disease models, ii) integrate the data with genetic risk and biomarker information, and iii) directly manipulate the levels of the altered proteins or RNAs in various model systems to observe their impact on pathophysiology potentially relevant to human AD. By undertaking these approaches, we can gain deeper insights into the significance of omic-level changes in AD, going beyond their descriptive nature and unraveling their potential role in the disease process.

Here, we performed quantitative tandem mass tag mass spectrometry (TMT-MS) based proteomics analyses of the brains from CRND8 transgenic mice at various ages and compared these findings to human proteomic data previously generated from >500 subjects from the Religious Orders Study/Memory and Aging Project (ROSMAP) and Banner Sun Health cohorts [9]. We find robust and highly significant correlation in global proteome changes in human AD brain compared to CRND8 transgenic mouse models. Through integration of protein changes observed in mouse models with co-expression networks derived from human AD, we resolve conserved and divergent network module changes between humans and mice. Multiple proteins that map to the M42 matrisome module, accumulate in Aβ plaques, cerebrovascular amyloid (CAA) and/or dystrophic neuronal processes. We also demonstrate that overexpressing two M42 proteins, midkine (Mdk) and pleiotrophin (PTN), in CRND8 mice leads to accelerated accumulation of Aβ, accompanied by dramatic Aβ amyloid increases in blood vessels linked to CAA. Moreover, *in vitro*

experiments using recombinant MDK and PTN reveal their ability to enhance Aβ aggregation into amyloid structures. Surprisingly, we find that many M42 proteins exhibit binding to fibrillar Aβ and non-human amyloid fibrils *in vitro*. Supporting this association, both MDK and PTN co-accumulate with transthyretin (TTR) amyloid in the heart. These findings establish several critical insights. First, that specific proteomic or module changes observed in human AD brains result from amyloid deposition. Second, amyloid structures seem to serve as scaffolds, facilitating the co-accumulation of proteins such as MDK and PTN with well-established signaling functions. This comprehensive understanding of proteomic changes and their interplay with amyloid deposition provides valuable insights into the complexity of AD pathogenesis and potential biomarkers. More specifically, they suggest that antagonizing MDK and/or PTN binding to amyloid could be a therapeutic strategy.

RESULTS

Deep TMT MS proteomes from 6, 12and 18M CRND8 APP Mice

We have generated TMT-MS proteomic data from the 8M urea extracts of the brains of 6 months (M) 12M and 18M CRND8 mice and non-transgenic (non-Tg) controls (Figure 1, Table S1-S5). We identified 8561, 10066, and 10543 proteins in the 6M, 12M and 18M cohorts with <50% missing values. In the 6M cohort, CRND8 mice show 1097 significant differentially expressed proteins (DEPs) with 172 increased and 65 decreased by more than 20% (Figure 1A). In the 12M cohort, 2340 DEPs are detected with 454 increased and 327 decreased by more than 20% (Figure 1B). In the 18M cohort, 2244 DEPs are detected with 639 increased and 450 decreased by more than 20% (Figure 1C). Notably, proteomic changes in 12M and 18M cohorts are highly reproducible (R^2=0.8129 $p < 1e^{-200}$) (Figure 1D), despite being close, but not precise biological replicates. Indeed, out of the 1006 proteins that were significantly altered and detected in both cohorts only 8 were discordant and for these the log2 fold change (log2 Fc) was modest. Such data indicate that using small cohorts of CRND8 mice and matched non-Tg brains with varying levels of amyloid deposition, we can reliably and reproducibly detect proteomic alterations and that these changes increase with age in this transgenic mouse model of rapid and robust Aβ deposition.

Both full-length APP and specific peptides mapping to the human Aβ peptide sequence also distinguishes Tg from non-Tg mice in all cohorts, consistent with human transgene expression and increasing deposition of Aβ (Figure 1A-C, Table S1). Other proteins previously shown to interact with APP such as (Apbb1 (Fe65), Vac14, Rufy2, Tnfrsf21) are also altered at various ages in the CRND8 proteome and several of these (Apbb1, Vac14, Rufy2) show relatively stable alterations across the age groups suggesting that these may be related to mutant APP overexpression and not linked to Aβ or the response to Aβ accumulation per se (Table S1) [25-27]. Top gene ontology (GO) terms for the DEPs increased in all cohorts highlight heparin and glycosaminoglycan binding, amyloid fibril formation and regulation, vacuolar and lysosomal transport, and immune phagosome and vesicular and lysosomal transport, integrin binding and extracellular matrix (ECM) organization (Figure 1E). Top ontology terms for the decreased DEPs in all cohorts highlight impacts on lipid binding, synaptic vesicle regulation and neurotransmitter release, mitochondrial membrane, and neurogenesis and axogenesis. (Figure 1E).

In the 12 and 18M cohorts there is an appreciable rightward shift in the volcano plots reflecting many proteins that show an age dependent increase in protein level indicating such changes may reflect the evolving "responsome" to enhanced accumulation of Aβ. A subset of the proteins that show the largest fold change increase have been observed to be altered in other APP mouse models and in humans [9,10,14,18,28,29] (Table S1). However, in this study using the older CRND8 mice which have extensive parenchymal amyloid deposition in the forebrain and hippocampus and cerebrovascular amyloid deposition (CAA) in the cerebellum, we appear to detect a more comprehensive picture of the alterations in the proteome in response to Aβ deposition in the brain. Top gene ontology (GO) and KEGG terms for the DEPs that are significantly increased in the 18M CRND8 cohort by log2 Fc > 0.2 and increase by more

148 than 2-fold relative to the change observed in the 6M cohort highlight endosomal and lysosomal
149 processes, axonogenesis and neurogenesis, ECM organization, nitric oxide and superoxide metabolism,
150 and glycosaminoglycan degradation, and many other processes (Figure 1G). Limiting the input for these
151 analyses to the subset of proteins with significant log 2Fc > 1 in the 18M cohort, highlight oligodendrocyte
152 differentiation, synaptic signaling and organization, glycoprotein and, heparin, sulfur compound binding,
153 ECM, and neurogenesis and axogenesis (Figure 1H). Top gene ontology (GO) and KEGG terms for the DEPs
154 that are significantly decreased in the 18M CRND8 cohort by log2 Fc < -0.1 and decrease by more than 2-
155 fold relative to the change observed in the 6M cohort highlight terms around neurotransmitter
156 localization and synaptic function, neurogenesis and axogenesis, signal transduction and protein
157 localization to membrane rafts (Figure 1I).

158 **Integration of the AD human brain and CRND8 mouse brain proteome reveals both conserved and**
159 **divergent changes.**

160 To better understand the similarities and differences in protein levels between human AD and control
161 brains and in theCRND8 Tg and non-Tg mouse brain, we leveraged an extensive proteomic network
162 analysis and the resulting modular framework from human AD and control brains that has been previously
163 published. Using identical TMT-MS methodologies, we have built a deep consensus proteomic network
164 of >8,600 proteins from the dorsal lateral prefrontal cortex of >500 subjects from the Religious Orders
165 Study/Memory and Aging Project (ROSMAP) and Banner Sun Health cohorts [9]. This network was
166 constructed using the weighted gene co-expression network algorithm (WGCNA) and consists of 44
167 modules that reflect multiple biological and cell type processes, many of which are altered in AD. Globally,
168 when the levels of 7588 overlapping proteins are compared between the 18M CRND8 Tg and non-Tg
169 brains and AD and control brains there is a significant correlation ($p<1e^{-9}$, $R^2=0.158$) (Figure 2A); the
170 strength of the correlation is increased when filtering on the significant DEPs (n =709) in both the CRND8
171 and human AD brain proteomes relative to respective controls ($p<1e^{-9}$, $R^2=0.458$) (Figure 2B). Comparison
172 of the 6M CRND8 proteome changes with AD reveals a much weaker correlations for all overlapping
173 proteins (n=6794, $p<1e^{-9}$, $R^2=0.018$) (Figure 2C) but still a strong correlation for shared DEPs ($p<1e^{-9}$,
174 $R^2=0.438$) albeit with many fewer shared DEPs (n=161) (Figure 2D). Notably, the correlation for proteins
175 is stronger than for the correlations between protein coding mRNAs in 20M old CRND8 mice vs. non-Tg
176 mice brains and human AD and control brain superior temporal cortex from Mayo Clinic AD vs. control
177 RNAseq data (orthologous protein coding RNAs, n=13066, $R^2=0.079$; all shared DEGs, n=1399, $R^2=0.276$,
178 Figure S1) [12,30].

179 Inclusive correlations of all proteins shared within each of the human modules revealed select
180 modules with high overall correlations in terms of directionality and magnitude of changes, and modules
181 with negative correlations (Figure 2E). More granularly, when we assess the CRND8 mouse proteome
182 changes by evaluating the DEPs and preservation of direction of change within the human AD brain
183 module structure (Figure 2F), we find that there are number of modules in which there is a high degree
184 of preservation between the CRND8 mouse to human proteome in terms of DEP representation. There
185 are also modules for which many DEPs are discordant in terms of directionality, as well as modules where
186 the preservation of directionality is mixed (referred to as non-concordant). Modules showing strong
187 preservation and shared DEPs with increased levels are M42 (Matrisome), M11 (ECM), M7 (MAPK
188 Signaling), M24 (Ubiquitination), M25 (Sugar Metabolism), M19 (Angiogenesis), M12 Cytoskeleton, M39
189 (Translation Initiation), M21 (MHC/Immune), M38 (Heat Shock), M43 (Ribonucleoprotein), M12
190 (Cytoskeleton), M3 (Myelination) and M17 (Translation). Modules showing strong preservation and
191 shared DEPs with decreased levels are M22/M5 (Postsynaptic Density), M1 (Synaptic Transmission), M4
192 (Synapse), M2 (Mitochondria) and M33 (Hormone Secretion). Discordant changes are observed in M9
193 (Golgi), M44 (Viral Transcription), M29 (Glycosylation) M28 (Ribosome/Translation), M23 (GTPase
194 Activity), M34 (GTP Binding), M8 (Protein Transport), M30 (Proteasome), M16 (RNA Processing), and

M20/M13 (RNA Splicing). Examples of the cross-species correlations observed between all proteins within individual modules detected between the human AD proteome and the 18M CRND8 proteome are shown in Figure 2G and Figure S2. These correlations range from robust and significant (M42, M11, M4) to modest but significant (M7, M25, M2) to absent (M29).

Human AD protein modules show increased magnitude of change in aged CRND8 brains.

The human proteome and modular network included brains of individuals who had no reported cognitive decline yet neuropathologic criteria of AD. These were referred to as asymptomatic AD (Asym AD). Here we assessed the synthetic eigenprotein levels in the three CRND8 cohorts to evaluate how the overlapping mouse proteins within these modules change over age and how they compare to the modular eigenprotein changes in human Asym AD, and AD (Figure 3 and Figure S3). These data show that across many modules there is an increase in the magnitude of the eigenprotein change with preserved directionality as CRND8 mice age (e.g., M42, M11, M21, M7, M1, M9). Other modules show different patterns of change in the cohorts. For example, M15 (Kinase activity) and M2 (Mitochondria) show increased eigenproteins in the 6M cohort and then decreased eigenprotein in the older cohorts, whereas M3 (Myelination) shows a decreased eigenprotein at 6M and then increased at later timepoints. Such data demonstrate that the DEP changes observed often show progressive changes over the age range studied and reveal complex relationships between age, pathology, and proteome changes.

Correlations between Protein and RNA changes in the 18M CRND8 brains.

In human brain, the overall correlation between changes in mRNA and protein levels between AD and control brains is weak [9]. Here we directly compared the protein and RNA levels in the 18M CRND8 cohort. Analyzing the correlation between the changes in 9319 common gene products detected in the 18M CRND8 vs non-Tg proteome at the protein and mRNA levels (Figure S4A) reveals a weak correlation, which is on par with the overall correlation observed in the human brain (protein vs RNA changes in AD vs Control DLPFC) [9]. However, when these data are analyzed within the framework of the protein modular networks, a more complex relationship between changes in mRNA levels and protein levels is observed (Figure S4B-D, Figure S5). For example, within M42 there is no correlation between protein and mRNA levels in either human or mice. However, for modules M11 and M21 there is robust and highly significant correlation between protein and mRNA levels in the CRND8 mouse brain. A more modest, but still highly significant, correlation is observed in the same modules in human AD brain.

Validation of the proteome changes -focus on M42.

We have taken a multifaceted approach to validate the protein changes observed with a major focus on M42 proteins, the module with the most robust changes in CRND8 and strongest correlations between mice and human brains. We also included studies of additional DEPs identified only in the CRND8 proteomes that based on biological inference relating to the protein being secreted, a component of the ECM, and known or inferred (based on homology) binding to heparan sulfate (HS) or heparan sulfate proteoglycans (HSPGs) likely had biological roles relevant to M42. We thus refer to this group of proteins as M42+. Several additional DEPs, which showed a log2 Fc >1 in the 18M cohort (Ctss, S100a6, Rev3l), were also targeted in this validation even though they had no obvious links to M42 biology. There was a manifold rationale for the primary focus on M42+ proteins. First, M42 was strongly associated with both core pathological features of AD and cognitive decline and both APOE and APP/Aβ were present in the network. Second, M42, as shown above, was the most conserved module between human AD and CRND8 mice. Third, with a few notable exceptions, protein changes appeared to be dissociated from changes in RNA, implicating possible disruptions in proteostasis. Fourth, many M42 proteins show the largest log2 Fc between AD and control brain and in many cases even more striking log2 Fc changes in CRND8 mice. Finally, M42 proteins, represent a mix of DEPs, several with links to AD and amyloid pathology, but others with little or no previous links to AD and amyloid.

241 **MDK and PTN co-accumulate with Aβ in plaques and CAA.**

242 We focused initial validation studies at the brain tissue level, as successful detection of the DEP *in situ*
243 would enable us to put the protein changes in pathological context. As exemplars of these studies, we
244 highlight work on midkine (Mdk) and pleiotrophin (Ptn). Mdk and Ptn are homologous small secreted
245 signaling molecules known to interact with HS/HSPGs and signal through a set of overlapping receptors
246 (Sdc1-4, Ptprz1, Ptprb, Lrp1, Ncl, and Integrins α4β1, α6β1, α5β3) [31,32]. In the TMT-MS data, Mdk is
247 significantly increased in all three cohorts studied (log2 Fc) and has the largest log2 Fc of any DEP in the
248 6M cohort, whereas Ptn shows significant increases in the 12 and 18M cohorts. Neither mRNA is altered
249 in bulk transcriptomic studies of human AD brain or APP CRND8 mice brains, though the mRNA levels
250 (Fpkm) are significantly higher for Ptn than Mdk in both human and mouse brain. Select Mdk/Ptn
251 receptors are also altered at the protein level in human AD, CRND8 or both. For example, Sdc2 and Sdc4
252 are significantly increased in AD and CRND8 brains; Ptprz1 is significantly downregulated in CRND8 brains;
253 Lrp1 is significantly upregulated in AD and CRND8 brains; one isoform of Ncl is decreased in 18M CRND8
254 mice; Itga4 and Itgb4 are increased in both CRND8 and AD; Itga5 and b3 are increased in CRND8 mice
255 (Table S1).

256 Immunostaining for Mdk or Ptn shows both exhibit a high degree of overlap with Aβ in CRND8 mice
257 (Figure 4A) and in human brain (Figure 4B). Not only do Mdk and Ptn co-localize to plaques (Figure 4A),
258 but they also co-localize to Aβ amyloid in blood vessels associated with CAA, which is most easily observed
259 in CRND8 in the meningeal vessels of the cerebellum (Figure 4A). In humans, MDK and PTN are detected
260 in both plaques and CAA deposits (Figure 4B). Though both Ptn and Mdk are detected in plaques, they
261 show distinct staining within the cored plaques (Figure 4B-D). Mdk is more prominent in the center of the
262 plaque core in mice and intensity of staining decreases towards the plaque periphery (Figure 4C). Ptn
263 staining is almost the mirror image of Mdk, and it is localized more on the periphery of the fibrillar plaque.
264 In many plaques Ptn does not stain the center where Mdk is most strongly localized (Figure 4C, D). In
265 contrast, in humans, though MDK is more intensely detected in the plaque center, the entire plaque is
266 typically stained, and PTN diffusely stains the fibrillar plaque (Figure 4B). In CAA in the CRND8 mice, both
267 Ptn and Mdk non-homogenously label amyloid deposits detected by Thioflavin S (Thio S) (Figure 4D). In
268 vessels there are some areas where Ptn staining does not overlap with Thio S staining, this might be
269 attributable to expression in pericytes, as Ptn is highly expressed in these cells. Further, staining of Mdk
270 and Ptn in CRND8 mice brains shows co-localization with plaques from 3-12M, as well as staining of
271 plaques in numerous lines of APP transgenic mice (Figure S6A).

272 Western blot analysis of 8M Urea extracts from 20M CRND8 mice brains shows an almost qualitative
273 accumulation of both Mdk and Ptn in both male and female CRND8 brains, relative to the non-transgenic
274 lines, suggesting that TMT-MS methodology may underestimate the true fold change in protein levels
275 (Figure S6B) [33]. As a characteristic feature of Aβ deposited as amyloid is lack of solubility by strong
276 detergent extraction, we examined the crude solubility profiles of Mdk and Ptn in CRND8-Tg brains
277 sequentially extracted with TBS, RIPA, 2% SDS and 8M Urea (Figure S6C). Though relatively low levels of
278 Mdk and Ptn are detected in the TBS and RIPA extracts, the largest amounts were present in the 2% SDS
279 fraction and none was detected in the 2% SDS insoluble urea soluble fraction. Notably, the relative
280 proportion of Mdk or Ptn appearing in each extraction was similar in both the CRND8 Tg and non-Tg brains.
281 This lack of change in gross solubility as the proteins accumulate suggests that they are not undergoing
282 an amyloid-like structural change, which is typically associated with detergent insolubility [34].

283 **Validation of additional M42+ DEP changes**.

284 We initially screened many commercially available antibodies to proteins in M42, few of these
285 antibodies worked in paraffin embedded tissues (Tables S11, S12); therefore, we generated many new
286 rabbit polyclonal antibodies. Data showing these antisera can detect the target protein, is provided in

287 Figure S8A. In mice, we evaluated antibody staining of Tg and non-Tg brains in formalin,
288 paraformaldehyde, and ethanol fixed sections. As shown in Figure 5A, we find that many of these
289 antibodies stain amyloid plaques in CRND8 mice (non-Tg controls are shown in Figure S7A), suggesting
290 that many M42+ proteins accumulate, at least in part, due to sequestration within plaques. In mice, a
291 curious feature of these studies is that the localization of the proteins with the plaques is often
292 morphologically distinct. Slit2, Vtn, Olfml3, Ndp, Rev3l, Ntn1, Hhipl1, Bmp6, Ctss, Frzb, Sema3e, Smoc2
293 and Nog are preferentially localized within the plaque center as observed for Mdk. Col25a1 and Dmp1
294 appear in the more peripheral regions of the fibrillar plaque akin to Ptn. Another subset shows more
295 diffuse homogenous staining of the plaques (e.g., Vtn, Sdc4, S100a6). Still others show a patchy,
296 nonhomogeneous, staining of the plaques (e.g., Hgf, Spock1, ApoD, Egfl8, C1qTnf4, Slit3), which may in
297 part be attributable to staining of dystrophic structures around or within the plaque. In addition, we find
298 that fixation conditions can dramatically impact the staining pattern observed and that the effects of
299 fixation are antibody dependent (Figure S7B). Dual labeling studies with Aβ or Thio S and a subset of these
300 proteins reinforce the different location within the plaque of select M42 proteins (Figure S7C). Finally,
301 except for Mdk, Col25a1 and Ptn, which appear to stain most non-diffuse plaques, we note that only a
302 subset of the plaques detected by Aβ immunohistochemistry is stained (Figure 5A). As the anti-Aβ
303 monoclonal used for staining has subnanomolar affinity, additional studies will be needed to further
304 evaluate the extent of co-localization using additional immunologic reagents.

305 CAA Aβ deposition is easily assessed in the cerebellum of 12M CRND8 mice. In Figure 5B we show the
306 subset of antibodies that stain CAA. In addition to Mdk and Ptn a smaller group of the M42+ DEPs are
307 detectable in CAA Aβ deposits (Col25a1, Olfml3, Htra1, Smoc1, Sulf1, Frzb, Egfl8, C1qtnf4, Smoc2, Nog).
308 All of these can also be shown to co-localize with Thio S staining in the vessels (Figure S7C).

309 Several M42 CRND8 DEPs show staining adjacent to the fibrillar plaque (Figure 5C). Spock3, Bmp6, Frzb,
310 and Nog, show staining patterns highly consistent with the classic dystrophic neurites (DN) often
311 visualized with anti-ubiquitin or other DN markers. In contrast, Col25a1, Vtn, Rev3l, Sdc4, S100a6, Egfl8,
312 Spock1, and Flt1 show peri-plaque staining that is distinct from the classic DN pattern. Selective staining
313 of reactive astrocytes is noted for Htra1, Sulf1, Sfrp1, HhIpl1, Spock3, Sema3d, and Smoc2 (Figure S7D).

314 We have been able to localize a smaller subset of the M42 proteins in AD postmortem brain tissue
315 (Figure 5D). EGFL8, C1QTNF4, COL25A1, HGF, SDC4, NTN1 and SMOC2, all show staining in plaques. We
316 would note that EGFL8 was not detected in the TMT-MS studies in human brain, but Egfl8 was detected
317 as a DEP in CRND8 mice. OLFM3, SPOCK3, SPOCK1, show staining of dystrophic structures around plaques.
318 SULF1, SFRP5 and SFRP1 stain reactive astrocytes.

319 In supplementary Table S9, we compile the staining observed and annotate our findings versus previous
320 studies in the field, we also classify the cell type expression observed for the proteins that we detect in
321 these immunohistochemistry studies using data available at the Allen brain atlas [35]. The extended M42+
322 members appear to arise from multiple cell types representing all major brain cell types. This observation
323 is consistent with the biological annotations of M42 (matrisome, ECM) and likely reflects extracellular
324 processes regulating or responding to abnormal extracellular protein accumulation. Many of the mRNAs
325 encoding these proteins are expressed at low levels (< 5 Fpkm). Further within the M42 DEPs only Olfml3,
326 which is selectively expressed by microglia, shows significant increase in mRNA levels in the 18M RNAseq
327 data. In previous RNAseq studies of CRND8 mice brains, we have found that Olfml3 mRNA levels are
328 increased at 6, 12 and 20M [30]. Ctss and S100a6 also show significant increases in mRNA levels, but as
329 noted previously, are not part of the core M42 module; the associated increase in these mRNAs may be
330 due to the reactive gliosis in the CRND8 brain. In addition to these immunohistochemical studies and data
331 on Mdk and Ptn, we can also demonstrate increases in the brains of older CRND8 mice of Vtn, Htra1,
332 Smoc1, Frzb, ApoD and Nog western blot analysis of the CRND8 mice (Figure S8B).

333 **Mdk and PTN overexpression increase parenchymal amyloid and CAA in CRND8 mice and accelerate**
334 **amyloid aggregation in vivo.**

335 Given the robust data showing the co-localization of Mdk and Ptn with both plaques and CAA Aβ
336 deposits and the early increase observed in the 6M TMT-MS data for Mdk, we evaluated the impact of
337 rAAV-mediated overexpression of Mdk or PTN on amyloid deposition in 2 cohorts of CRND8 mice. The
338 first study examined the impact of P0 ICV injection of rAAV2/8 vectors encoding Mdk or PTN after 3
339 months of age, the second at 6M of age. In both cohorts, similar impacts are observed, for brevity we will
340 primarily describe the 6M analysis here (Figure 6A-C). The 3-month overexpression data is presented in
341 Figure S9A-C. Widespread over expression of Mdk and PTN is detectable in the brain in both cohorts. Even
342 in the small early compact plaques in the 3M cohort it is possible to detect Mdk and PTN staining within
343 the plaques (Figure S9A). Mdk and PTN both increased parenchymal plaques (Figure 6A) and CAA (Figure
344 6B) as assessed by immunohistochemistry. In previous studies of CRND8 mice we have not noted sex
345 differences in amyloid deposition or other phenotypes, though these studies were not designed to be
346 powered to detect sex differences, post hoc analyses do not reveal any major impact of sex. Both also
347 increased Aβ levels in SDS and Formic Acid (FA) fractions, but not in the RIPA fractions (Figure 6C). These
348 studies establish that overexpression of either Mdk and Ptn can accelerate amyloid deposition into fibrillar
349 plaques and CAA in two cohorts. In the 6M cohort, we also evaluated reactive gliosis (Figure S9D, E). Both
350 Mdk and PTN increased astrocytosis assessed by Gfap staining, and PTN increased microgliosis as assessed
351 by Iba1 staining. Mdk overexpression also increased Iba-1 staining but this elevation was not significant.
352 We also assessed the impact of recombinant PTN and MDK on amyloid aggregation *in vitro* using standard
353 ThT fluorescence assays (Figure 6D). Both reproducibly and significantly accelerated Aβ42 aggregation.
354 Mdk also increased Aβ40 aggregation, whereas only a small impact for PTN on Aβ40 aggregation was
355 observed. End of assay total ThT fluorescence was also increased in all cases except for the Aβ40 PTN
356 study, suggesting increased β-sheet formation.

357 **Select M42+ proteins bind to Aβ fibrils and an amyloid derived from a non-human peptide, non-**
358 **homologous peptide.**

359 Many M42 proteins are known or can be inferred by study of other family members to be HS/HSPG
360 binding proteins. We have performed limited studies on heparin interaction with Mdk and Ptn and can
361 confirm strong interactions with immobilized heparin (Figure S10). We evaluated a larger number of these
362 for the potential to interact with Aβ42 fibrils and a non-homologous amyloid formed from a 12 amino acid
363 adenovirus shaft peptide (AVS fibrils) [36,37]. For these studies we turned to a simple amyloid-pulldown assay
364 to screen for interactions with insoluble amyloids [38-40]. As M42 proteins contain numerous intrachain
365 disulfide bonds and other post translational modifications (PTMs), we expressed a subset of these proteins
366 in HEK293 cells and collected conditioned media containing the secreted proteins. Aβ42 fibrils or the AVS
367 fibrils were then incubated and spun down to evaluate potential interactions with amyloid structures. For
368 the subset of proteins which we were able to detect in the media, we can show that APOE4, Mdk, Vtn,
369 Ptn, Olfml3, Htra1, Smoc1, Sulf1, Frzb, ApoD, C1qTnf4, Smoc2, and Nog bind both Aβ42 and AVS amyloids
370 (Figure 7A). Sfrp1 is a notable exception as we only observed it binding to Aβ fibrils in this assay. Such
371 studies provide initial data that many of these proteins bind a generic amyloid structure.

372 **PTN and MDK are colocalized with transthyretin (TTR) amyloid in the human heart.**

373 Though the amyloid pulldown assay shows the ability of multiple M42 proteins to interact with a
374 generic amyloid structure, we wanted to orthogonally test this hypothesis by evaluating whether some of
375 these proteins may accumulate in other human amyloid diseases. For these studies we have focused on
376 in *situ* detection of MDK and PTN, as the antibodies for these robustly detect these proteins in formalin
377 fixed human tissues. As shown in Figure 7B we find that both MDK and PTN co-localize with TTR amyloid
378 in the heart (the third most prominent human amyloid disease) [41]. A series of additional TTR cardiac

379 amyloid cases show consistent co-localization of PTN and CLU, and more variable co-localization of MDK,
380 with the TTR amyloid fibrils (Figure S11).

381 **DEPs in CRND8 mice in the context of AD genetic studies.**

382 Previous transcriptomic studies of APP mice have suggested that very highly upregulated DEGs are
383 enriched for genes under AD GWAS loci or known genetic risk factors for AD [42]. To examine whether DEPs
384 in the CRND8 mice might provide similar insights, we integrated data from three previous GWAS studies
385 of AD to evaluate whether DEPs in CRND8 mice reflect some aspects of the genetic architecture of human
386 AD (Table S1, Figure S12A) [43-45]. Integration of the 18M CRND8 TMT-MS data with these AD genetic studies
387 show that many established AD risk genes and prioritized GWAS loci (e.g., *APOE, BIN1, TREM2, CLU,*
388 *SORL1, ACE, ADAM17, SORT1, INPP5D)* are DEPS in the 18M CRND8 mice. Abca1, recently implicated as
389 genetic risk factor for AD, is also a DEP in both the 12m and 18M CRND8 cohorts [46]. Notably multiple
390 M42+ proteins besides APOE show nominal significance in the GWAS studies including *COL25A1, SMOC1,*
391 *HTRA1, DMP1, MDK, SDC4, SPOCK2, NXPH1*, and *C1QTNF4*, the latter of which lies in the *CELF1* locus and
392 shows the highest p value of M42 members for AD association. Finally, we note that Grn, Sppl2a,
393 Tmem106b and Notch3 are all DEPs in the 18M CRND8 proteome. *GRN* and *TMEM106B* are genetically
394 associated with FTD-GRN, and SPPL2A is known to cleave TMEM106B potentially linking it to the biology
395 of FTD-GRN [47,48]. Further, *NOTCH3* mutations are associated with CADASIL [49]. Given debate over genetic
396 pleiotropy or inclusion of non-AD dementia in the large GWAS studies (clinical phenocopy inclusion) [50,51],
397 these data suggest there are biological links between proteins implicated in FTD and CADASIL and amyloid
398 pathology in AD. A final intriguing observation from these data is that multiple proteins near the *APOE*
399 *l*ocus are DEPs in the CRND8 mice. There is conservation of the extended *APOE* locus between mice and
400 humans, and such data may point to complex biology around the *APOE* locus that could contribute to AD
401 risk.

402 **DEPs in CRND8 mice in the context of AD CSF biomarker studies**

403 We also evaluated the 18M cohort CRND8 DEPs in the context of human AD CSF biomarker studies, for
404 this integration we chose a recent data set in which AD and control CSF were compared using a highly
405 similar proteomic pipeline for both TMT-MS data generation and analysis [52]. However, we would note that
406 this data shows significant overlaps with other large scale proteomic analyses of AD versus control CSF [52-
407 62]. Of the 1839 in the human CSF proteomes 257 of these are significantly altered and of these 62 are
408 significantly changed in the 18M CRND8 mice brains. 39 of these changes are congruent in directionality
409 between the mouse brain and human CSF and 23 are discordant in directionality (Figure S12B, Table S13).
410 Notably, 29 of the 18M DEPs are significantly altered in the same direction in human AD brain as in the
411 mouse model, irrespective of direction of change in CSF, and only 5 show a discordant directionality with
412 human AD brain change. Overall, these data support a hypothesis that some significant and reproducible
413 changes in human CSF may reflect changes in the brain related to amyloid.

414 **DISCUSSION**

415 By integrating newly generated deep TMT proteomic data from CRND8 mice brains with previously
416 generated large-scale proteomic data from human AD brain, we have begun to define the Aβ/Aβ amyloid
417 "responsome" that is partially conserved between this mouse model of Aβ deposition and human AD [9,10].
418 Within select protein modules, DEP and overall protein changes are highly concordant; however, the
419 presence of multiple discordant protein network modules and modules that are simply not concordant,
420 reinforce the concept that these transgenic mice are incomplete models of AD [9,10,30]. Nevertheless, these
421 data and analyses establish a paradigm for contextualizing changes that occur in human AD and provide
422 an unbiased view of the degree to which a model system reflects, or does not reflect, the complex
423 proteomic changes in the human AD brain. Indeed, there is much debate about what defines a "better

424 mouse model", these data suggest that a comparative omics approach particularly those that analyze the
425 proteome, can provide a less biased manner to address this question [63,64].

426 As discussed in detail below, we have primarily focused validation studies on M42, the most
427 concordant module between human and mice, a module that in humans correlates best with amyloid and
428 tau pathologies and strongly correlates with cognitive status [9,10]. However, we document other
429 concordant modules and discordant or non-concordant modules as well. This modular framework may
430 offer initial insights into what aspects of AD pathology the mice mimic and what modules they do not, but
431 validation and contextualization of these will be required to better understand how these modules fit into
432 the complex architecture of AD pathology [2].

433 As CRND8 mice do not show overt neuronal loss [65], the finding that numerous modules relating to
434 neuronal and synaptic function (M1, M4, M5, M22, M33) show conservation is intriguing. Numerous APP
435 models, including CRND8 mice have been shown to have synaptic alterations [66-68], and in many cases these
436 alterations occur at relatively early ages [63,69,70] . Notably, our data show a progressive impact on synaptic
437 protein modules as assessed by eigenprotein levels. However, for the majority of human and mouse
438 proteins in these modules the magnitude of change as assessed by TMT-MS is quite small. Of interest,
439 neuritin (Nrn1) and small glutamine-rich tetratricopeptide repeat-containing protein β (Sgtb) which are
440 implicated in cognitive resilience to AD pathologies are both consistently downregulated DEPs in the older
441 CRND8 cohorts [71,72] . Nevertheless, these studies highlight the disconnect between Aβ amyloid deposition
442 models and human AD, as these models do not progress to an overt neurodegenerative state and lack
443 neurofibrillary tangle (NFT) pathology.

444 Several of the eigenprotein changes in the CRND8 brains assessed in the context of the human AD
445 modular framework show a consistent alteration in directionality and an increased separation between
446 Tg and non-Tg from 6M to 18M (e.g., M42, M28, M11, M12, M4, M23). Other modules, such as M3
447 (Myelination, down at 6M and up at 12/18M) and M15 (Kinase Activity, up at 6M and down at 12/18M)
448 show discordant directionality across the cohorts. Notably, for myelination there is evidence in other APP
449 mice models that there are temporal changes in oligodendrocyte lineages and myelin that may be
450 consistent with this data [73-75] and, more generally, there is growing evidence for oligodendrocyte lineage
451 and myelin alterations in AD [76-78] and other tauopathies [76,79]. However, these specific proteomic changes
452 need to i) be validated in this model and ii) further contextualized by refining these proteomic and
453 validation studies through inclusion of a broader cross-sectional series of ages and additional models with
454 differential temporal sequence of amyloid deposition.

455 We also may need to refine how we view concordant, non-concordant, and discordant changes
456 between the model and human protein modular networks. A good example of this is M21, the
457 MHC/immune module, though the correlation within this module not significant, in general most proteins
458 in this module are upregulated in both human and mice, however, in humans the protein upregulation of
459 immune module is much less robust, although transcriptome upregulation is significant in both human
460 and mouse brains in the context of AD [11,80]. This data suggests that mice respond to amyloid deposition
461 with a more robust innate immune response than humans, perhaps because of i) the compressed time
462 frame for amyloid deposition in these models ii) impacts of aging on the human brain which may alter
463 baseline immune status [81,82] or iii) inherent interspecies differences in synthesis and clearance of these
464 proteins.

465 More broadly, future studies will be needed to guide our understanding of the proteomic changes in
466 mouse models that mimic human AD and those that do not. Similar deep proteomic studies on tau mice
467 might inform on protein modules more related to NFT pathology. We also should consider that discordant
468 modules in mice such as upregulation of M9 (Golgi) that includes ER to Golgi trafficking proteins and

469 lysosomal hydrolases and proteases, might serve protective functions that could impact the appearance
470 of downstream pathologies and overt neurodegeneration in the models [83,84].

471 To build a highly significant deep TMT-MS proteome from human AD brain required hundreds of
472 samples [9,10], in contrast using small cohorts of CRND8 mice we can generate highly reproducible data.
473 Further, by looking at cohorts of different ages, we can infer changes that might be attributable to
474 transgene overexpression versus increasing level of Aβ deposition. The CRND8 mouse is a robust and
475 aggressive model of amyloid deposition [65]. CRND8 mice have shown a very reproducible phenotype across
476 many studies, with no easily discernable sex-based impacts on pathological phenotypes [39,68,85]. Notably
477 our data is highly consistent with previously published proteomic data on 5X FAD mice, but because of
478 the depth, multiple ages, and larger groups sizes we appear to be cataloging a larger number of proteomic
479 changes [14,29]. From a translational point of view, these data reinforce the notion that preclinical studies
480 probing impacts of therapies targeting amyloid or pathologies downstream of amyloid should not just be
481 tested in younger mice with limited amyloid deposition but should also be evaluated in the context of
482 impacts on older mice with extensive amyloid deposition.

483 For the reasons described previously, we focused validation efforts on the M42+ module. We had
484 known from previous studies that several of the core M42 members including APP, APOE and COL25A1
485 accumulate in amyloid plaques [86-90]. Here we provide additional evidence that many of the core human
486 M42 module are present in plaques in mice (Mdk, Ntn1, Smoc1, Sdc4, Olfml3, Sfrp1, Spock1, Frzb, Htra11,
487 Slit2), we also show that many other proteins emerging from the CRND8 proteome (Vtn, Dmp1, Ndp,
488 Rev3l, Hgf, HHipl1, S100a6, Bmp6, Ctss, Sema3e, ApoD, Egfl8, C1qtnf4, Smoc2, Nog and Slit3) are also
489 present in the plaques in mice. A subset of these M42+ proteins also are found in CAA, others in dystrophic
490 processes around plaques and others in reactive astrocytes. We have successfully localized a smaller
491 number of these proteins to plaques and other pathological features in humans. Given the conserved
492 protein changes in mice and humans seen by proteomic analyses, this discrepancy may be attributable to
493 fixation conditions and epitope exposure, which may differ between mice and humans. Our current data
494 showing how fixation conditions can alter the pathologies detected by select antibodies in mice, highlight
495 the importance of developing multiple high-quality antibodies to extend and further validate these initial
496 pathological assignments.

497 Notably, two proteins Egfl8 and Hgf were only detected and present as DEPs in the CRND8 proteome,
498 but both HGF and EGFL8 appear to be plaque components in humans. Such findings serve as an exemplar
499 of the power of utilizing a model system to inform on human pathology. Further, these studies broadly
500 serve as a strong affirmation of the power of WGCNA to inform pathobiology of a complex disease [91].
501 Indeed, M42 is the most conserved protein module network between CRND8 mice and human AD and
502 shows the strongest correlation with amyloid in humans [9,10]; these validation studies highlight its direct
503 links relevant to amyloid pathology or response to amyloid pathology.

504 Some of the more nuanced data emerging from these validation studies relate to the unique patterns
505 of localization of these proteins within fibrillar plaques. This feature has been most rigorously studied for
506 Mdk and Ptn which show unique and reciprocal distributions in the CRND8 plaques, and distinct
507 distributions in human plaques. Overall, there appear to be four general patterns of staining. The first
508 pattern is like Mdk, whereby the core of plaques is labeled most intensely, the second pattern, like Ptn,
509 shows more intense peripheral staining of the plaque, a third pattern, such as seen with Sdc4, shows a
510 very homogenous staining of the entire plaque and a fourth pattern, such as seen with Egfl8, shows patchy
511 non-homogenous staining. Such data along with data showing that only a subset of parenchymal plaque
512 associated proteins are detected in CAA, raises many questions about the nature of these interactions
513 and the differences and similarities of not only CAA and plaque amyloid, but also even the concept that
514 structural interactions may vary even within a single plaque. Direct studies of the human CAA proteome
515 have also found increased levels of OLFML3, PTN and HTR1A, along with other known CAA components

516 (e.g., APOE, CLU, APCS) [92,93]. Further study of CAA and cerebral autosomal-dominant arteriopathy with
517 subcortical infarcts and leukoencephalopathy (CADASIL) vessels' proteomes shows overlap with each
518 other, but also reveal extensive and broad overlap with many M42 DEPs [92,94]. As Notch3 and Htra1 are
519 increased DEPs in CRND8 mice, and we have been able to detect Htra1 in vessels, further study of CAA
520 and its impact on the proteome is warranted. Indeed, there is emerging evidence that sequestration of
521 HTRA1, a serine protease, with NOTCH3 in CADASIL leads to HTRA1 loss of function and accumulation of
522 select HTRA1 substrates [92,94]. Such data could account for the similarities between CADASIL and cerebral
523 autosomal recessive arteriopathy with subcortical infarcts and leukoencephalopathy (CARASIL), the latter
524 of which is caused by heterozygous loss of function mutations in *HTRA1*. Such data suggest that HTRA1
525 accumulation in CAA and in plaques might have similar impacts and contribute to CAA driven vascular
526 dysfunction in AD.

527 The data showing that overexpression of Mdk or PTN in the CRND8 brain results in increased CAA and
528 parenchymal Aβ amyloid suggests that these proteins have a direct impact on amyloid deposition, and
529 therefore represent novel therapeutic targets in AD. As both proteins can accelerate aggregation of Aβ
530 and bind preexisting amyloid fibrils *in vitro* we hypothesize they act as amyloid chaperones likely directly
531 impacting the rate of Aβ aggregation. However, Mdk is known to have impacts on myeloid cell lineages
532 and its co-accumulation in plaques could theoretically impact microglial mediated clearance either
533 through gain or loss of function [95,96] Ptn, which signals largely through the same receptors as Mdk, could
534 have similar impacts as well [97]. Thus, it is also plausible that these proteins may also influence cell
535 mediated clearance of Aβ. More broadly, additional studies will be needed to evaluate the impact of not
536 only Mdk and Ptn but the many co-accumulating proteins on not amyloid deposition itself, but also the
537 cellular responses to the deposits. Though a previous study had noted that a Mdk knockout crossed into
538 an APP transgenic line resulted in increased amyloid deposition, we would note this data is simply
539 anecdotal [98]. Non-Tg mice Mdk and Ptn knockouts were also studied, and claimed to increase amyloid
540 deposition, but in that study the antibody 6E10, which is highly selective for human Aβ was used to stain
541 "plaques". Thus, such results are likely artifactual.

542 HS and HSPGs along with chondroitin sulfate proteoglycans (CSPGs) have long been implicated in the
543 biology of AD and other amyloid deposits [99]. HS and select HSPGs core proteins (e.g., HSPG2, ACAN) have
544 been shown to accumulate in plaques or dystrophic neurites. HSPGs have also been reported to accelerate
545 Aβ aggregation and mediate internalization of extracellular tau [100]. In these proteomic studies, we detect
546 HSPG2, ACAN, and multiple CSPGs but they are minimally altered in either mice or the human AD
547 proteome (Table S1). In contrast, in human AD, GPC4,5; SPOCK1-3; and SDC2,4 are much more robust
548 DEPs and many of these are core M42 module members. In CRND8 mice Gpc1,5; Spock1-3 and Sdc2,4 are
549 also robust DEPs (Table S1). Further, gene ontology strongly demonstrates heparin and glycosaminoglycan
550 biology related biological processes upregulation in aged CRND8 mice brains (Figure 1).

551 We have not systematically evaluated heparin binding as a surrogate for HS/HSPG binding of many of
552 the M42+ proteins studied here, but we find MDK and PTN secreted from mammalians cells bind robustly
553 to heparin. We do find that a subset of the M42+ proteins secreted by human embryonic kidney 293
554 (HEK293) cells bind Aβ42 amyloid and a non-human, non-homologous amyloid fibrils [36,37]. This subset of
555 M42+ proteins was pragmatically chosen simply based on proteins which were secreted and detectable
556 in the media of transiently transfected HEK293 cells. This data led us to explore whether MDK and PTN
557 might be components of peripheral amyloids and we find both accumulate in TTR cardiac amyloid.
558 Neither have been previously detected, even in extensive laser capture proteomic studies of cardiac
559 amyloid deposits [101]. As HS/HSPGs are common components of amyloids, these studies suggest that there
560 may be very complex multipartite structural interactions between amyloid, HS/HSPGs and these co-
561 accumulating proteins which may prove challenging to unravel.

562 Given the intensive studies of both Aβ amyloid and peripheral amyloids, it is somewhat surprising that
563 we and others are finding numerous additional proteins co-accumulating with amyloid [14,28,29,101,102]. In
564 both the human and mouse studies brain tissue was extracted with 8M urea; thus, we are studying the
565 total detectable urea solubilized proteome and not the detergent insoluble proteome. Indeed, for Mdk
566 and Ptn in mice brains we find no gross change in solubility, despite the large increase in the Tg mouse
567 brains. Following SDS-extraction, no residual protein is detected in the Urea fraction. These initial
568 solubility studies likely explain why many of these proteins are not detected in detergent insoluble
569 fractions typically used to isolate amyloid, they simply may not be there.

570 Our current data and data from others reveal numerous proteins that co-deposit with Aβ amyloid.
571 Further, given the large number of proteins showing age progressive increases in the CRND8 mice brain,
572 it is highly likely that over time many additional proteins will be found to accumulate with Aβ amyloid and
573 perhaps other disease relevant amyloids as well. Indeed, two recently identified components of Aβ
574 plaques, Pycard and Mfge8, are increased DEPs in our data, but in the 18M old CRND8 cohort rank 296th
575 and 300th among all the increased DEPs in terms of log2 Fc [103,104]. In the human AD proteome, PYCARD is
576 significantly increased (log2 Fc=0.06), and MFGE8 is detected but not increased. Cleary not all proteins
577 upregulated will be components of plaques, but these data clearly point to biology of amyloid that is much
578 more complex than previously appreciated, and that the response to amyloid deposits may also be equally
579 as complex.

580 Despite thousands of studies and numerous hypotheses, there is ongoing debate as to how amyloid
581 or Aβ aggregate pathology drives cellular dysfunction that leads to the neurodegenerative phase of AD
582 [2,7,8]. More generally, this debate extends to all amyloid disorders and how amyloid accumulation causes
583 tissue damage [34,41,105]. Indeed, extensive efforts have been made to identify more toxic species or
584 conformers (e.g., oligomer, protofibril, dimer, specific fibrillar conformer) [106]. Our current data, along with
585 previous studies of proteins that co-accumulate with amyloid, offer an alternative hypothesis to the
586 concept that amyloid or some distinct amyloid-like aggregate is a direct toxin [70,107]. We term this the
587 "amyloid scaffold" hypothesis (Figure S13) and posit that if amyloid deposits can scaffold the accumulation
588 of numerous proteins than perhaps the accumulation of these proteins mediates downstream
589 pathophysiology. Both toxic gain of function and loss of function mechanisms need to be considered.
590 Accumulation of proteins within amyloid deposits could lead to gain of normal function if these proteins
591 retain activity or if such binding activates a novel signaling pathway. Sequestration in the deposit could
592 result in loss of function and reduced levels in the surrounding tissue. If solubility of select proteins
593 accumulating in the amyloid deposit is not changed, then these proteins may retain signaling function.
594 Indeed, many of the proteins we detect in plaques and CAA are known signaling molecules and through
595 either loss or gain of function mechanisms their accumulation could impact dystrophic neurite and
596 reactive glia in the local plaque microenvironment or cells in the vessel wall. In the heart MDK, though
597 shown to have some cardioprotective effects, can also promote intimal hyperplasia whereas PTN have
598 been shown to have angiogenic effects [108-110]. Thus, this hypothesis may have relevance for peripheral
599 amyloidoses as well. There are also intriguing parallels between this concept of amyloid as a scaffold for
600 pathological process and functional amyloids which have been proposed to mediate their biological
601 effects in part through a scaffolding mechanism (reviewed in [111]).

602 As with many biologic responses, it is important to consider that the accumulation of proteins in the
603 plaque is not simply a bystander effect, but part of the response to amyloid as a danger associated
604 molecular pattern [81,112]. The amyloid "scaffold" and amyloid (or oligomer) as "direct toxin" hypotheses are
605 not mutually exclusive. Amyloid fibrils and oligomers are potent activators of microglia and myeloid cells
606 and soluble oligomeric and protofibrillar aggregates can mediate many impacts on different cells [30,70].
607 Proteins that interact with an amyloid or oligomer structure could be actively involved both in clearance,
608 coating, and neutralization of the structure to reduce toxicity, or some combination of these. Other

609 components may simply be bystanders, at least with respect to impacts on amyloid deposition, but once
610 present could still mediate pathology by altering signaling gradients. er.

611 There is extensive data that APOE and CLU interaction with Aβ/Aβ amyloid deposits alters the local
612 cellular response, and influence amyloid deposition itself[86-88,113,114] Because of their genetic association
613 with AD, they are also considered therapeutic targets, though it has been challenging to develop
614 therapeutic approaches that modulate APOE or CLU and show robust preclinical disease modifying
615 impacts [115]. We have not yet explored studies in knockout mice, however, overexpression studies suggest
616 that Mdk and PTN, like APOE and CLU, can increase amyloid deposition and both also increase CAA. It will
617 be intriguing to evaluate the impacts of the larger set of proteins that are now being shown to co-
618 accumulate. We might speculate that some will promote amyloid deposition, others might block it and
619 still others might simply bind without altering kinetics of deposition. Our initial data suggest that many of
620 these co-accumulating proteins could be considered as novel therapeutic targets, but additional probes
621 of their biology will be necessary to determine their role in disease and their druggability.

622 Integrating data from genetic studies of AD and the DEPs in the CRND8 mouse brain, reinforces links
623 between many established AD genes or prioritized genetic loci and AD risk genes and regulation of
624 Aβ catabolism and deposition or response to Aβ deposition. This integration also provides an additional
625 criterion that might be considered when prioritizing studies in loci with multiple candidate genes. Indeed,
626 multiple proteins that are within M42, co-deposit with amyloid, or both and show nominally significant
627 associations with AD. Integration of CRND8 proteome with AD CSF biomarkers shows that many proteins
628 significantly altered in human AD CSF are DEPs in the brains of an amyloid depositing mouse model. Again,
629 these data suggest that these CSF biomarkers might reflect the impacts of amyloid pathology on the AD
630 brain. With the approval of immunotherapies that can dramatically impact amyloid deposition it will be
631 intriguing to determine if this subset of CSF AD biomarkers is altered in response to such therapy. Recently
632 SMOC1 and SPON1, two core M42 members have been found to be altered in concert with decreases in
633 Aβ42/40 ratios in the CSF of individuals with dominantly inherited AD [57]. Further, Smoc1 is a highly
634 reproducible highly upregulated AD CSF biomarker [53,57,61,116].

635 In summary, this contextualized understanding of AD and APP mouse model proteomic changes
636 provides insights into the true molecular complexity of AD pathogenesis and informs on biomarkers and
637 novel therapeutic targets related to amyloid deposition. Though we have i) validated some of the more
638 robust protein changes in the proteomic analyses, ii) provided pathological insight related to a subset of
639 these proteins, and iii) generated initial modeling and biochemical data to support potential
640 pathobiological roles, there is still much to be learned about amyloid and its role in AD pathophysiology
641 and in other amyloid disorders. Clearly, future integrative omic studies can build off and refine these
642 current studies, especially by incorporating models of additional pathologies relevant to AD and other
643 amyloid disorders.

644 **Limitations of the study**

645 We commented on the many limitations of this multifaceted study in the results and discussion, but
646 several overarching limitations are highlighted here. First, the pathological validation studies vary with
647 respect to the confidence in the findings. Classic criteria suggest two antibodies or antisera to two distinct
648 epitopes of the target protein are needed to confirm presence in pathological setting. A subset of the
649 pathological findings is based on a single antibody or antisera. However, we would note that this criterion
650 was often utilized in an era when additional data (e.g., proteomic based) was lacking. Second, we do not
651 have extensive proteomic data from human brains with amyloid deposition prior to the presence of other
652 pathologies. Thus, we have limited our integration of the mouse data to human brain data which has a
653 spectrum of AD pathologies. This fact limits inference as to which proteomic changes in humans are truly
654 amyloid driven. Third, the lack of analyses of a group young enough to lack amyloid deposition or

alternatively a manipulation that alters amyloid loads, impose some interpretative limitations on the data with respect to changes driven by amyloid or mutant APP overexpression. Nevertheless, given the multiple layers of orthogonal and integrative data used in this study we believe that this study begins to capture and contextualize proteomic changes in AD and a mouse model of amyloid deposition in a way that will inform downstream studies for many years.

661 **REFERENCES**

662 1. Hardy, J., and Selkoe, D.J. (2002). The amyloid hypothesis of Alzheimer's disease: progress and
663 problems on the road to therapeutics. Science *297*, 353-356.
664 2. Golde, T.E. (2022). Alzheimer's disease - the journey of a healthy brain into organ failure. Mol
665 Neurodegener *17*, 18. 10.1186/s13024-022-00523-1.
666 3. Budd Haeberlein, S., Aisen, P.S., Barkhof, F., Chalkias, S., Chen, T., Cohen, S., Dent, G., Hansson,
667 O., Harrison, K., von Hehn, C., et al. (2022). Two Randomized Phase 3 Studies of Aducanumab in
668 Early Alzheimer's Disease. J Prev Alzheimers Dis *9*, 197-210. 10.14283/jpad.2022.30.
669 4. Sims, J.R., Zimmer, J.A., Evans, C.D., Lu, M., Ardayfio, P., Sparks, J., Wessels, A.M., Shcherbinin, S.,
670 Wang, H., Monkul Nery, E.S., et al. (2023). Donanemab in Early Symptomatic Alzheimer Disease:
671 The TRAILBLAZER-ALZ 2 Randomized Clinical Trial. JAMA. 10.1001/jama.2023.13239.
672 5. van Dyck, C.H., Swanson, C.J., Aisen, P., Bateman, R.J., Chen, C., Gee, M., Kanekiyo, M., Li, D.,
673 Reyderman, L., Cohen, S., et al. (2023). Lecanemab in Early Alzheimer's Disease. N Engl J Med *388*,
674 9-21. 10.1056/NEJMoa2212948.
675 6. Golde, T.E., Schneider, L.S., and Koo, E.H. (2011). Anti-abeta therapeutics in Alzheimer's disease:
676 the need for a paradigm shift. Neuron *69*, 203-213. S0896-6273(11)00003-1
677 [pii]10.1016/j.neuron.2011.01.002.
678 7. Murdock, M.H., and Tsai, L.H. (2023). Insights into Alzheimer's disease from single-cell genomic
679 approaches. Nat Neurosci *26*, 181-195. 10.1038/s41593-022-01222-2.
680 8. Long, J.M., and Holtzman, D.M. (2019). Alzheimer Disease: An Update on Pathobiology and
681 Treatment Strategies. Cell *179*, 312-339. 10.1016/j.cell.2019.09.001.
682 9. Johnson, E.C.B., Carter, E.K., Dammer, E.B., Duong, D.M., Gerasimov, E.S., Liu, Y., Liu, J., Betarbet,
683 R., Ping, L., Yin, L., et al. (2022). Large-scale deep multi-layer analysis of Alzheimer's disease brain
684 reveals strong proteomic disease-related changes not observed at the RNA level. Nat Neurosci *25*,
685 213-225. 10.1038/s41593-021-00999-y.
686 10. Johnson, E.C.B., Dammer, E.B., Duong, D.M., Ping, L., Zhou, M., Yin, L., Higginbotham, L.A.,
687 Guajardo, A., White, B., Troncoso, J.C., et al. (2020). Large-scale proteomic analysis of Alzheimer's
688 disease brain and cerebrospinal fluid reveals early changes in energy metabolism associated with
689 microglia and astrocyte activation. Nat Med *26*, 769-780. 10.1038/s41591-020-0815-6.
690 11. Wan, Y.W., Al-Ouran, R., Mangleburg, C.G., Perumal, T.M., Lee, T.V., Allison, K., Swarup, V., Funk,
691 C.C., Gaiteri, C., Allen, M., et al. (2020). Meta-Analysis of the Alzheimer's Disease Human Brain
692 Transcriptome and Functional Dissection in Mouse Models. Cell Rep *32*, 107908.
693 10.1016/j.celrep.2020.107908.
694 12. Allen, M., Carrasquillo, M.M., Funk, C., Heavner, B.D., Zou, F., Younkin, C.S., Burgess, J.D., Chai,
695 H.S., Crook, J., Eddy, J.A., et al. (2016). Human whole genome genotype and transcriptome data
696 for Alzheimer's and other neurodegenerative diseases. Sci Data *3*, 160089.
697 10.1038/sdata.2016.89.
698 13. Wang, X., Allen, M., Is, O., Reddy, J.S., Tutor-New, F.Q., Castanedes Casey, M., Carrasquillo, M.M.,
699 Oatman, S.R., Min, Y., Asmann, Y.W., et al. (2021). Alzheimer's disease and progressive
700 supranuclear palsy share similar transcriptomic changes in distinct brain regions. J Clin Invest.
701 10.1172/JCI149904.
702 14. Bai, B., Wang, X., Li, Y., Chen, P.C., Yu, K., Dey, K.K., Yarbro, J.M., Han, X., Lutz, B.M., Rao, S., et al.
703 (2020). Deep Multilayer Brain Proteomics Identifies Molecular Networks in Alzheimer's Disease
704 Progression. Neuron *106*, 700. 10.1016/j.neuron.2020.04.031.
705 15. Bai, B., Hales, C.M., Chen, P.C., Gozal, Y., Dammer, E.B., Fritz, J.J., Wang, X., Xia, Q., Duong, D.M.,
706 Street, C., et al. (2013). U1 small nuclear ribonucleoprotein complex and RNA splicing alterations
707 in Alzheimer's disease. Proc Natl Acad Sci U S A *110*, 16562-16567. 10.1073/pnas.1310249110.

16. Zhang, B., Gaiteri, C., Bodea, L.G., Wang, Z., McElwee, J., Podtelezhnikov, A.A., Zhang, C., Xie, T., Tran, L., Dobrin, R., et al. (2013). Integrated systems approach identifies genetic nodes and networks in late-onset Alzheimer's disease. Cell *153*, 707-720. 10.1016/j.cell.2013.03.030.
17. Rayaprolu, S., Higginbotham, L., Bagchi, P., Watson, C.M., Zhang, T., Levey, A.I., Rangaraju, S., and Seyfried, N.T. (2021). Systems-based proteomics to resolve the biology of Alzheimer's disease beyond amyloid and tau. Neuropsychopharmacology *46*, 98-115. 10.1038/s41386-020-00840-3.
18. Drummond, E., Kavanagh, T., Pires, G., Marta-Ariza, M., Kanshin, E., Nayak, S., Faustin, A., Berdah, V., Ueberheide, B., and Wisniewski, T. (2022). The amyloid plaque proteome in early onset Alzheimer's disease and Down syndrome. Acta Neuropathol Commun *10*, 53. 10.1186/s40478-022-01356-1.
19. De Jager, P.L., Yang, H.S., and Bennett, D.A. (2018). Deconstructing and targeting the genomic architecture of human neurodegeneration. Nat Neurosci *21*, 1310-1317. 10.1038/s41593-018-0240-z.
20. Xiong, X., James, B.T., Boix, C.A., Park, Y.P., Galani, K., Victor, M.B., Sun, N., Hou, L., Ho, L.L., Mantero, J., et al. (2023). Epigenomic dissection of Alzheimer's disease pinpoints causal variants and reveals epigenome erosion. Cell *186*, 4422-4437 e4421. 10.1016/j.cell.2023.08.040.
21. Sun, N., Victor, M.B., Park, Y.P., Xiong, X., Scannail, A.N., Leary, N., Prosper, S., Viswanathan, S., Luna, X., Boix, C.A., et al. (2023). Human microglial state dynamics in Alzheimer's disease progression. Cell *186*, 4386-4403 e4329. 10.1016/j.cell.2023.08.037.
22. Sun, N., Akay, L.A., Murdock, M.H., Park, Y., Galiana-Melendez, F., Bubnys, A., Galani, K., Mathys, H., Jiang, X., Ng, A.P., et al. (2023). Single-nucleus multiregion transcriptomic analysis of brain vasculature in Alzheimer's disease. Nat Neurosci *26*, 970-982. 10.1038/s41593-023-01334-3.
23. Mathys, H., Peng, Z., Boix, C.A., Victor, M.B., Leary, N., Babu, S., Abdelhady, G., Jiang, X., Ng, A.P., Ghafari, K., et al. (2023). Single-cell atlas reveals correlates of high cognitive function, dementia, and resilience to Alzheimer's disease pathology. Cell *186*, 4365-4385 e4327. 10.1016/j.cell.2023.08.039.
24. Wang, X., Allen, M., Li, S., Quicksall, Z.S., Patel, T.A., Carnwath, T.P., Reddy, J.S., Carrasquillo, M.M., Lincoln, S.J., Nguyen, T.T., et al. (2020). Deciphering cellular transcriptional alterations in Alzheimer's disease brains. Mol Neurodegener *15*, 38. 10.1186/s13024-020-00392-6.
25. Cao, X., and Sudhof, T.C. (2001). A transcriptionally active complex of APP with Fe65 and histone acetyltransferase Tip60. Science *293*, 115-120.
26. Balklava, Z., Niehage, C., Currinn, H., Mellor, L., Guscott, B., Poulin, G., Hoflack, B., and Wassmer, T. (2015). The Amyloid Precursor Protein Controls PIKfyve Function. PLoS One *10*, e0130485. 10.1371/journal.pone.0130485.
27. Zhang, T., Yu, J., Wang, G., and Zhang, R. (2021). Amyloid precursor protein binds with TNFRSF21 to induce neural inflammation in Alzheimer's Disease. Eur J Pharm Sci *157*, 105598. 10.1016/j.ejps.2020.105598.
28. Askenazi, M., Kavanagh, T., Pires, G., Ueberheide, B., Wisniewski, T., and Drummond, E. (2023). Compilation of reported protein changes in the brain in Alzheimer's disease. Nat Commun *14*, 4466. 10.1038/s41467-023-40208-x.
29. Bai, B., Vanderwall, D., Li, Y., Wang, X., Poudel, S., Wang, H., Dey, K.K., Chen, P.C., Yang, K., and Peng, J. (2021). Proteomic landscape of Alzheimer's Disease: novel insights into pathogenesis and biomarker discovery. Mol Neurodegener *16*, 55. 10.1186/s13024-021-00474-z.
30. McFarland, K.N., Ceballos, C., Rosario, A., Ladd, T., Moore, B., Golde, G., Wang, X., Allen, M., Ertekin-Taner, N., Funk, C.C., et al. (2021). Microglia show differential transcriptomic response to Abeta peptide aggregates ex vivo and in vivo. Life Sci Alliance *4*. 10.26508/lsa.202101108.
31. Winkler, C., and Yao, S. (2014). The midkine family of growth factors: diverse roles in nervous system formation and maintenance. Br J Pharmacol *171*, 905-912. 10.1111/bph.12462.

32. Herradon, G., and Perez-Garcia, C. (2014). Targeting midkine and pleiotrophin signalling pathways in addiction and neurodegenerative disorders: recent progress and perspectives. Br J Pharmacol *171*, 837-848. 10.1111/bph.12312.
33. Ting, L., Rad, R., Gygi, S.P., and Haas, W. (2011). MS3 eliminates ratio distortion in isobaric multiplexed quantitative proteomics. Nat Methods *8*, 937-940. 10.1038/nmeth.1714.
34. Glenner, G.G. (1980). Amyloid deposits and amyloidosis. The New England of Medicine *302*, 1283-1292.
35. Yao, Z., van Velthoven, C.T.J., Nguyen, T.N., Goldy, J., Sedeno-Cortes, A.E., Baftizadeh, F., Bertagnolli, D., Casper, T., Chiang, M., Crichton, K., et al. (2021). A taxonomy of transcriptomic cell types across the isocortex and hippocampal formation. Cell *184*, 3222-3241 e3226. 10.1016/j.cell.2021.04.021.
36. Luckey, M., Hernandez, J., Arlaud, G., Forsyth, V.T., Ruigrok, R.W., and Mitraki, A. (2000). A peptide from the adenovirus fiber shaft forms amyloid-type fibrils. FEBS Lett *468*, 23-27.
37. Papanikolopoulou, K., Schoehn, G., Forge, V., Forsyth, V.T., Riekel, C., Hernandez, J.F., Ruigrok, R.W., and Mitraki, A. (2005). Amyloid fibril formation from sequences of a natural beta-structured fibrous protein, the adenovirus fiber. J Biol Chem *280*, 2481-2490.
38. Levites, Y., Jansen, K., Smithson, L.A., Dakin, R., Holloway, V.M., Das, P., and Golde, T.E. (2006). Intracranial adeno-associated virus-mediated delivery of anti-pan amyloid beta, amyloid beta40, and amyloid beta42 single-chain variable fragments attenuates plaque pathology in amyloid precursor protein mice. J Neurosci *26*, 11923-11928. 26/46/11923 [pii]10.1523/JNEUROSCI.2795-06.2006.
39. Chakrabarty, P., Li, A., Ladd, T.B., Strickland, M.R., Koller, E.J., Burgess, J.D., Funk, C.C., Cruz, P.E., Allen, M., Yaroshenko, M., et al. (2018). TLR5 decoy receptor as a novel anti-amyloid therapeutic for Alzheimer's disease. J Exp Med *215*, 2247-2264. 10.1084/jem.20180484.
40. Lessard, C.B., Malnik, S.L., Zhou, Y., Ladd, T.B., Cruz, P.E., Ran, Y., Mahan, T.E., Chakrabaty, P., Holtzman, D.M., Ulrich, J.D., et al. (2018). High-affinity interactions and signal transduction between Abeta oligomers and TREM2. EMBO Mol Med *10*. 10.15252/emmm.201809027.
41. Eisenberg, D., and Jucker, M. (2012). The amyloid state of proteins in human diseases. Cell *148*, 1188-1203. 10.1016/j.cell.2012.02.022.
42. Matarin, M., Salih, D.A., Yasvoina, M., Cummings, D.M., Guelfi, S., Liu, W., Nahaboo Solim, M.A., Moens, T.G., Paublete, R.M., Ali, S.S., et al. (2015). A genome-wide gene-expression analysis and database in transgenic mice during development of amyloid or tau pathology. Cell Rep *10*, 633-644. 10.1016/j.celrep.2014.12.041.
43. Kunkle, B.W., Grenier-Boley, B., Sims, R., Bis, J.C., Damotte, V., Naj, A.C., Boland, A., Vronskaya, M., van der Lee, S.J., Amlie-Wolf, A., et al. (2019). Genetic meta-analysis of diagnosed Alzheimer's disease identifies new risk loci and implicates Abeta, tau, immunity and lipid processing. Nat Genet *51*, 414-430. 10.1038/s41588-019-0358-2.
44. Bellenguez, C., Kucukali, F., Jansen, I.E., Kleineidam, L., Moreno-Grau, S., Amin, N., Naj, A.C., Campos-Martin, R., Grenier-Boley, B., Andrade, V., et al. (2022). New insights into the genetic etiology of Alzheimer's disease and related dementias. Nat Genet *54*, 412-436. 10.1038/s41588-022-01024-z.
45. Lambert, J.C., Ibrahim-Verbaas, C.A., Harold, D., Naj, A.C., Sims, R., Bellenguez, C., DeStafano, A.L., Bis, J.C., Beecham, G.W., Grenier-Boley, B., et al. (2013). Meta-analysis of 74,046 individuals identifies 11 new susceptibility loci for Alzheimer's disease. Nat Genet *45*, 1452-1458. 10.1038/ng.2802.
46. Holstege, H., Hulsman, M., Charbonnier, C., Grenier-Boley, B., Quenez, O., Grozeva, D., van Rooij, J.G.J., Sims, R., Ahmad, S., Amin, N., et al. (2022). Exome sequencing identifies rare damaging

803 variants in ATP8B4 and ABCA1 as risk factors for Alzheimer's disease. Nat Genet *54*, 1786-1794.
804 10.1038/s41588-022-01208-7.
805 47. Rademakers, R., Neumann, M., and Mackenzie, I.R. (2012). Advances in understanding the
806 molecular basis of frontotemporal dementia. Nat Rev Neurol *8*, 423-434.
807 10.1038/nrneurol.2012.117.
808 48. Brady, O.A., Zhou, X., and Hu, F. (2014). Regulated intramembrane proteolysis of the
809 frontotemporal lobar degeneration risk factor, TMEM106B, by signal peptide peptidase-like 2a
810 (SPPL2a). J Biol Chem *289*, 19670-19680. 10.1074/jbc.M113.515700.
811 49. Chabriat, H., Joutel, A., Dichgans, M., Tournier-Lasserve, E., and Bousser, M.G. (2009). Cadasil.
812 Lancet Neurol *8*, 643-653. 10.1016/S1474-4422(09)70127-9.
813 50. Escott-Price, V., and Hardy, J. (2022). Genome-wide association studies for Alzheimer's disease:
814 bigger is not always better. Brain Commun *4*, fcac125. 10.1093/braincomms/fcac125.
815 51. Andrews, S.J., Fulton-Howard, B., and Goate, A. (2020). Interpretation of risk loci from genome-
816 wide association studies of Alzheimer's disease. Lancet Neurol *19*, 326-335. 10.1016/S1474-
817 4422(19)30435-1.
818 52. Modeste, E.S., Ping, L., Watson, C.M., Duong, D.M., Dammer, E.B., Johnson, E.C.B., Roberts, B.R.,
819 Lah, J.J., Levey, A.I., and Seyfried, N.T. (2023). Quantitative proteomics of cerebrospinal fluid from
820 African Americans and Caucasians reveals shared and divergent changes in Alzheimer's disease.
821 Mol Neurodegener *18*, 48. 10.1186/s13024-023-00638-z.
822 53. Watson, C.M., Dammer, E.B., Ping, L., Duong, D.M., Modeste, E., Carter, E.K., Johnson, E.C.B.,
823 Levey, A.I., Lah, J.J., Roberts, B.R., and Seyfried, N.T. (2023). Quantitative Mass Spectrometry
824 Analysis of Cerebrospinal Fluid Protein Biomarkers in Alzheimer's Disease. Sci Data *10*, 261.
825 10.1038/s41597-023-02158-3.
826 54. van Zalm, P.W., Ahmed, S., Fatou, B., Schreiber, R., Barnaby, O., Boxer, A., Zetterberg, H., Steen,
827 J.A., and Steen, H. (2023). Meta-analysis of published cerebrospinal fluid proteomics data
828 identifies and validates metabolic enzyme panel as Alzheimer's disease biomarkers. Cell Rep Med
829 *4*, 101005. 10.1016/j.xcrm.2023.101005.
830 55. Sung, Y.J., Yang, C., Norton, J., Johnson, M., Fagan, A., Bateman, R.J., Perrin, R.J., Morris, J.C.,
831 Farlow, M.R., Chhatwal, J.P., et al. (2023). Proteomics of brain, CSF, and plasma identifies
832 molecular signatures for distinguishing sporadic and genetic Alzheimer's disease. Sci Transl Med
833 *15*, eabq5923. 10.1126/scitranslmed.abq5923.
834 56. Panyard, D.J., McKetney, J., Deming, Y.K., Morrow, A.R., Ennis, G.E., Jonaitis, E.M., Van Hulle, C.A.,
835 Yang, C., Sung, Y.J., Ali, M., et al. (2023). Large-scale proteome and metabolome analysis of CSF
836 implicates altered glucose and carbon metabolism and succinylcarnitine in Alzheimer's disease.
837 Alzheimers Dement. 10.1002/alz.13130.
838 57. Johnson, E.C.B., Bian, S., Haque, R.U., Carter, E.K., Watson, C.M., Gordon, B.A., Ping, L., Duong,
839 D.M., Epstein, M.P., McDade, E., et al. (2023). Cerebrospinal fluid proteomics define the natural
840 history of autosomal dominant Alzheimer's disease. Nat Med *29*, 1979-1988. 10.1038/s41591-
841 023-02476-4.
842 58. Visser, P.J., Reus, L.M., Gobom, J., Jansen, I., Dicks, E., van der Lee, S.J., Tsolaki, M., Verhey, F.R.J.,
843 Popp, J., Martinez-Lage, P., et al. (2022). Cerebrospinal fluid tau levels are associated with
844 abnormal neuronal plasticity markers in Alzheimer's disease. Mol Neurodegener *17*, 27.
845 10.1186/s13024-022-00521-3.
846 59. Delvenne, A., Gobom, J., Tijms, B., Bos, I., Reus, L.M., Dobricic, V., Kate, M.T., Verhey, F., Ramakers,
847 I., Scheltens, P., et al. (2022). Cerebrospinal fluid proteomic profiling of individuals with mild
848 cognitive impairment and suspected non-Alzheimer's disease pathophysiology. Alzheimers
849 Dement. 10.1002/alz.12713.

850 60. Del Campo, M., Peeters, C.F.W., Johnson, E.C.B., Vermunt, L., Hok, A.H.Y.S., van Nee, M., Chen-
851 Plotkin, A., Irwin, D.J., Hu, W.T., Lah, J.J., et al. (2022). CSF proteome profiling across the
852 Alzheimer's disease spectrum reflects the multifactorial nature of the disease and identifies
853 specific biomarker panels. Nat Aging *2*, 1040-1053. 10.1038/s43587-022-00300-1.
854 61. Dammer, E.B., Ping, L., Duong, D.M., Modeste, E.S., Seyfried, N.T., Lah, J.J., Levey, A.I., and
855 Johnson, E.C.B. (2022). Multi-platform proteomic analysis of Alzheimer's disease cerebrospinal
856 fluid and plasma reveals network biomarkers associated with proteostasis and the matrisome.
857 Alzheimers Res Ther *14*, 174. 10.1186/s13195-022-01113-5.
858 62. Higginbotham, L., Ping, L., Dammer, E.B., Duong, D.M., Zhou, M., Gearing, M., Hurst, C., Glass, J.D.,
859 Factor, S.A., Johnson, E.C.B., et al. (2020). Integrated proteomics reveals brain-based
860 cerebrospinal fluid biomarkers in asymptomatic and symptomatic Alzheimer's disease. Sci Adv *6*.
861 10.1126/sciadv.aaz9360.
862 63. Dawson, T.M., Golde, T.E., and Lagier-Tourenne, C. (2018). Animal models of neurodegenerative
863 diseases. Nat Neurosci *21*, 1370-1379. 10.1038/s41593-018-0236-8.
864 64. Drummond, E., and Wisniewski, T. (2017). Alzheimer's disease: experimental models and reality.
865 Acta Neuropathol *133*, 155-175. 10.1007/s00401-016-1662-x.
866 65. Chishti, M.A., Yang, D.S., Janus, C., Phinney, A.L., Horne, P., Pearson, J., Strome, R., Zuker, N.,
867 Loukides, J., French, J., et al. (2001). Early-onset amyloid deposition and cognitive deficits in
868 transgenic mice expressing a double mutant form of amyloid precursor protein 695. J Biol Chem
869 *276*, 21562-21570.
870 66. Wykes, R., Kalmbach, A., Eliava, M., and Waters, J. (2012). Changes in the physiology of CA1
871 hippocampal pyramidal neurons in preplaque CRND8 mice. Neurobiol Aging *33*, 1609-1623.
872 10.1016/j.neurobiolaging.2011.05.001.
873 67. Jolas, T., Zhang, X.S., Zhang, Q., Wong, G., Del Vecchio, R., Gold, L., and Priestley, T. (2002). Long-
874 term potentiation is increased in the CA1 area of the hippocampus of APP(swe/ind) CRND8 mice.
875 Neurobiol Dis *11*, 394-409.
876 68. Chakrabarty, P., Li, A., Ceballos-Diaz, C., Eddy, J.A., Funk, C.C., Moore, B., DiNunno, N., Rosario,
877 A.M., Cruz, P.E., Verbeeck, C., et al. (2015). IL-10 alters immunoproteostasis in APP mice,
878 increasing plaque burden and worsening cognitive behavior. Neuron *85*, 519-533.
879 10.1016/j.neuron.2014.11.020.
880 69. Palop, J.J., and Mucke, L. (2010). Amyloid-beta-induced neuronal dysfunction in Alzheimer's
881 disease: from synapses toward neural networks. Nat Neurosci *13*, 812-818. 10.1038/nn.2583.
882 70. Selkoe, D.J., and Hardy, J. (2016). The amyloid hypothesis of Alzheimer's disease at 25 years.
883 EMBO Mol Med *8*, 595-608. 10.15252/emmm.201606210.
884 71. Yu, L., Tasaki, S., Schneider, J.A., Arfanakis, K., Duong, D.M., Wingo, A.P., Wingo, T.S., Kearns, N.,
885 Thatcher, G.R.J., Seyfried, N.T., et al. (2020). Cortical Proteins Associated With Cognitive Resilience
886 in Community-Dwelling Older Persons. JAMA Psychiatry *77*, 1172-1180.
887 10.1001/jamapsychiatry.2020.1807.
888 72. Hurst, C.D., Dunn, A.R., Dammer, E.B., Duong, D.M., Seyfried, N.T., Kaczorowski, C.C., and Johnson,
889 E.C.B. (2023). Genetic background influences the 5XFAD Alzheimer's disease mouse model brain
890 proteome. bioRxiv. 10.1101/2023.06.12.544646.
891 73. Mitew, S., Kirkcaldie, M.T., Halliday, G.M., Shepherd, C.E., Vickers, J.C., and Dickson, T.C. (2010).
892 Focal demyelination in Alzheimer's disease and transgenic mouse models. Acta Neuropathol *119*,
893 567-577. 10.1007/s00401-010-0657-2.
894 74. Desai, M.K., Mastrangelo, M.A., Ryan, D.A., Sudol, K.L., Narrow, W.C., and Bowers, W.J. (2010).
895 Early oligodendrocyte/myelin pathology in Alzheimer's disease mice constitutes a novel
896 therapeutic target. Am J Pathol *177*, 1422-1435. 10.2353/ajpath.2010.100087.

75. Desai, M.K., Sudol, K.L., Janelsins, M.C., Mastrangelo, M.A., Frazer, M.E., and Bowers, W.J. (2009). Triple-transgenic Alzheimer's disease mice exhibit region-specific abnormalities in brain myelination patterns prior to appearance of amyloid and tau pathology. Glia *57*, 54-65. 10.1002/glia.20734.
76. Allen, M., Wang, X., Burgess, J.D., Watzlawik, J., Serie, D.J., Younkin, C.S., Nguyen, T., Malphrus, K.G., Lincoln, S., Carrasquillo, M.M., et al. (2018). Conserved brain myelination networks are altered in Alzheimer's and other neurodegenerative diseases. Alzheimers Dement *14*, 352-366. 10.1016/j.jalz.2017.09.012.
77. McKenzie, A.T., Moyon, S., Wang, M., Katsyv, I., Song, W.M., Zhou, X., Dammer, E.B., Duong, D.M., Aaker, J., Zhao, Y., et al. (2017). Multiscale network modeling of oligodendrocytes reveals molecular components of myelin dysregulation in Alzheimer's disease. Mol Neurodegener *12*, 82. 10.1186/s13024-017-0219-3.
78. Nasrabady, S.E., Rizvi, B., Goldman, J.E., and Brickman, A.M. (2018). White matter changes in Alzheimer's disease: a focus on myelin and oligodendrocytes. Acta Neuropathol Commun *6*, 22. 10.1186/s40478-018-0515-3.
79. Min, Y., Wang, X., Is, O., Patel, T.A., Gao, J., Reddy, J.S., Quicksall, Z.S., Nguyen, T., Lin, S., Tutor-New, F.Q., et al. (2023). Cross species systems biology discovers glial DDR2, STOM, and KANK2 as therapeutic targets in progressive supranuclear palsy. Nat Commun *14*, 6801. 10.1038/s41467-023-42626-3.
80. Wang, X., Allen, M., Is, O., Reddy, J.S., Tutor-New, F.Q., Castanedes Casey, M., Carrasquillo, M.M., Oatman, S.R., Min, Y., Asmann, Y.W., et al. (2022). Alzheimer's disease and progressive supranuclear palsy share similar transcriptomic changes in distinct brain regions. J Clin Invest *132*. 10.1172/JCI149904.
81. Golde, T.E. (2019). Harnessing Immunoproteostasis to Treat Neurodegenerative Disorders. Neuron *101*, 1003-1015. 10.1016/j.neuron.2019.02.027.
82. Patel, T., Carnwath, T.P., Wang, X., Allen, M., Lincoln, S.J., Lewis-Tuffin, L.J., Quicksall, Z.S., Lin, S., Tutor-New, F.Q., Ho, C.C.G., et al. (2022). Transcriptional landscape of human microglia implicates age, sex, and APOE-related immunometabolic pathway perturbations. Aging Cell *21*, e13606. 10.1111/acel.13606.
83. Van Acker, Z.P., Perdok, A., Bretou, M., and Annaert, W. (2021). The microglial lysosomal system in Alzheimer's disease: Guardian against proteinopathy. Ageing Res Rev *71*, 101444. 10.1016/j.arr.2021.101444.
84. Pimplikar, S.W., Nixon, R.A., Robakis, N.K., Shen, J., and Tsai, L.H. (2010). Amyloid-independent mechanisms in Alzheimer's disease pathogenesis. J Neurosci *30*, 14946-14954. 10.1523/JNEUROSCI.4305-10.2010.
85. Ibanez, K.R., McFarland, K.N., Phillips, J., Allen, M., Lessard, C.B., Zobel, L., De La Cruz, E.G., Shah, S., Vo, Q., Wang, X., et al. (2022). Deletion of Abi3/Gngt2 influences age-progressive amyloid beta and tau pathologies in distinctive ways. Alzheimers Res Ther *14*, 104. 10.1186/s13195-022-01044-1.
86. Castellano, J.M., Kim, J., Stewart, F.R., Jiang, H., DeMattos, R.B., Patterson, B.W., Fagan, A.M., Morris, J.C., Mawuenyega, K.G., Cruchaga, C., et al. (2011). Human apoE isoforms differentially regulate brain amyloid-beta peptide clearance. Sci Transl Med *3*, 89ra57. 10.1126/scitranslmed.3002156.
87. Holtzman, D.M. (2004). In vivo effects of ApoE and clusterin on amyloid-beta metabolism and neuropathology. J Mol Neurosci *23*, 247-254.
88. Fagan, A.M., Watson, M., Parsadanian, M., Bales, K.R., Paul, S.M., and Holtzman, D.M. (2002). Human and murine ApoE markedly alters A beta metabolism before and after plaque formation in a mouse model of Alzheimer's disease. Neurobiol Dis *9*, 305-318.

945 89. Soderberg, L., Zhukareva, V., Bogdanovic, N., Hashimoto, T., Winblad, B., Iwatsubo, T., Lee, V.M.,
946 Trojanowski, J.Q., and Naslund, J. (2003). Molecular identification of AMY, an Alzheimer disease
947 amyloid-associated protein. J Neuropathol Exp Neurol *62*, 1108-1117. 10.1093/jnen/62.11.1108.
948 90. Hashimoto, T., Wakabayashi, T., Watanabe, A., Kowa, H., Hosoda, R., Nakamura, A., Kanazawa, I.,
949 Arai, T., Takio, K., Mann, D.M., and Iwatsubo, T. (2002). CLAC: a novel Alzheimer amyloid plaque
950 component derived from a transmembrane precursor, CLAC-P/collagen type XXV. EMBO J *21*,
951 1524-1534. 10.1093/emboj/21.7.1524.
952 91. Langfelder, P., and Horvath, S. (2008). WGCNA: an R package for weighted correlation network
953 analysis. BMC Bioinformatics *9*, 559. 10.1186/1471-2105-9-559.
954 92. Zellner, A., Muller, S.A., Lindner, B., Beaufort, N., Rozemuller, A.J.M., Arzberger, T., Gassen, N.C.,
955 Lichtenthaler, S.F., Kuster, B., Haffner, C., and Dichgans, M. (2022). Proteomic profiling in cerebral
956 amyloid angiopathy reveals an overlap with CADASIL highlighting accumulation of HTRA1 and its
957 substrates. Acta Neuropathol Commun *10*, 6. 10.1186/s40478-021-01303-6.
958 93. Hondius, D.C., Eigenhuis, K.N., Morrema, T.H.J., van der Schors, R.C., van Nierop, P., Bugiani, M.,
959 Li, K.W., Hoozemans, J.J.M., Smit, A.B., and Rozemuller, A.J.M. (2018). Proteomics analysis
960 identifies new markers associated with capillary cerebral amyloid angiopathy in Alzheimer's
961 disease. Acta Neuropathol Commun *6*, 46. 10.1186/s40478-018-0540-2.
962 94. Zellner, A., Scharrer, E., Arzberger, T., Oka, C., Domenga-Denier, V., Joutel, A., Lichtenthaler, S.F.,
963 Muller, S.A., Dichgans, M., and Haffner, C. (2018). CADASIL brain vessels show a HTRA1 loss-of-
964 function profile. Acta Neuropathol *136*, 111-125. 10.1007/s00401-018-1853-8.
965 95. Cerezo-Wallis, D., Contreras-Alcalde, M., Troule, K., Catena, X., Mucientes, C., Calvo, T.G., Canon,
966 E., Tejedo, C., Pennacchi, P.C., Hogan, S., et al. (2020). Midkine rewires the melanoma
967 microenvironment toward a tolerogenic and immune-resistant state. Nat Med *26*, 1865-1877.
968 10.1038/s41591-020-1073-3.
969 96. Tang, Y., Kwiatkowski, D.J., and Henske, E.P. (2022). Midkine expression by stem-like tumor cells
970 drives persistence to mTOR inhibition and an immune-suppressive microenvironment. Nat
971 Commun *13*, 5018. 10.1038/s41467-022-32673-7.
972 97. Shen, D., Podolnikova, N.P., Yakubenko, V.P., Ardell, C.L., Balabiyev, A., Ugarova, T.P., and Wang,
973 X. (2017). Pleiotrophin, a multifunctional cytokine and growth factor, induces leukocyte responses
974 through the integrin Mac-1. J Biol Chem *292*, 18848-18861. 10.1074/jbc.M116.773713.
975 98. Muramatsu, H., Yokoi, K., Chen, L., Ichihara-Tanaka, K., Kimura, T., and Muramatsu, T. (2011).
976 Midkine as a factor to counteract the deposition of amyloid beta-peptide plaques: in vitro analysis
977 and examination in knockout mice. Int Arch Med *4*, 1. 10.1186/1755-7682-4-1.
978 99. Snow, A.D., Cummings, J.A., and Lake, T. (2021). The Unifying Hypothesis of Alzheimer's Disease:
979 Heparan Sulfate Proteoglycans/Glycosaminoglycans Are Key as First Hypothesized Over 30 Years
980 Ago. Front Aging Neurosci *13*, 710683. 10.3389/fnagi.2021.710683.
981 100. Vaquer-Alicea, J., and Diamond, M.I. (2019). Propagation of Protein Aggregation in
982 Neurodegenerative Diseases. Annu Rev Biochem *88*, 785-810. 10.1146/annurev-biochem-
983 061516-045049.
984 101. Kourelis, T.V., Dasari, S.S., Dispenzieri, A., Maleszewski, J.J., Redfield, M.M., Fayyaz, A.U., Grogan,
985 M., Ramirez-Alvarado, M., Abou Ezzeddine, O.F., and McPhail, E.D. (2020). A Proteomic Atlas of
986 Cardiac Amyloid Plaques. JACC CardioOncol *2*, 632-643. 10.1016/j.jaccao.2020.08.013.
987 102. Rahman, M.M., and Lendel, C. (2021). Extracellular protein components of amyloid plaques and
988 their roles in Alzheimer's disease pathology. Mol Neurodegener *16*, 59. 10.1186/s13024-021-
989 00465-0.
990 103. Wagner, J., Degenhardt, K., Veit, M., Louros, N., Konstantoulea, K., Skodras, A., Wild, K., Liu, P.,
991 Obermuller, U., Bansal, V., et al. (2022). Medin co-aggregates with vascular amyloid-beta in
992 Alzheimer's disease. Nature *612*, 123-131. 10.1038/s41586-022-05440-3.

104. Venegas, C., Kumar, S., Franklin, B.S., Dierkes, T., Brinkschulte, R., Tejera, D., Vieira-Saecker, A., Schwartz, S., Santarelli, F., Kummer, M.P., et al. (2017). Microglia-derived ASC specks cross-seed amyloid-beta in Alzheimer's disease. Nature *552*, 355-361. 10.1038/nature25158.
105. Yakupova, E.I., Bobyleva, L.G., Shumeyko, S.A., Vikhlyantsev, I.M., and Bobylev, A.G. (2021). Amyloids: The History of Toxicity and Functionality. Biology (Basel) *10*. 10.3390/biology10050394.
106. Walsh, D.M., and Selkoe, D.J. (2004). Deciphering the molecular basis of memory failure in Alzheimer's disease. Neuron *44*, 181-193.
107. Dobson, C.M., Knowles, T.P.J., and Vendruscolo, M. (2020). The Amyloid Phenomenon and Its Significance in Biology and Medicine. Cold Spring Harb Perspect Biol *12*. 10.1101/cshperspect.a033878.
108. Papadimitriou, E., Mourkogianni, E., Ntenekou, D., Christopoulou, M., Koutsioumpa, M., and Lamprou, M. (2022). On the role of pleiotrophin and its receptors in development and angiogenesis. Int J Dev Biol *66*, 115-124. 10.1387/ijdb.210122ep.
109. Weckbach, L.T., Grabmaier, U., Uhl, A., Gess, S., Boehm, F., Zehrer, A., Pick, R., Salvermoser, M., Czermak, T., Pircher, J., et al. (2019). Midkine drives cardiac inflammation by promoting neutrophil trafficking and NETosis in myocarditis. J Exp Med *216*, 350-368. 10.1084/jem.20181102.
110. Woulfe, K.C., and Sucharov, C.C. (2017). Midkine's Role in Cardiac Pathology. J Cardiovasc Dev Dis *4*. 10.3390/jcdd4030013.
111. Rubel, M.S., Fedotov, S.A., Grizel, A.V., Sopova, J.V., Malikova, O.A., Chernoff, Y.O., and Rubel, A.A. (2020). Functional Mammalian Amyloids and Amyloid-Like Proteins. Life (Basel) *10*. 10.3390/life10090156.
112. Venegas, C., and Heneka, M.T. (2017). Danger-associated molecular patterns in Alzheimer's disease. J Leukoc Biol *101*, 87-98. 10.1189/jlb.3MR0416-204R.
113. Pinals, R.L., and Tsai, L.H. (2022). Building in vitro models of the brain to understand the role of APOE in Alzheimer's disease. Life Sci Alliance *5*. 10.26508/lsa.202201542.
114. Martens, Y.A., Zhao, N., Liu, C.C., Kanekiyo, T., Yang, A.J., Goate, A.M., Holtzman, D.M., and Bu, G. (2022). ApoE Cascade Hypothesis in the pathogenesis of Alzheimer's disease and related dementias. Neuron *110*, 1304-1317. 10.1016/j.neuron.2022.03.004.
115. Xiong, M., Jiang, H., Serrano, J.R., Gonzales, E.R., Wang, C., Gratuze, M., Hoyle, R., Bien-Ly, N., Silverman, A.P., Sullivan, P.M., et al. (2021). APOE immunotherapy reduces cerebral amyloid angiopathy and amyloid plaques while improving cerebrovascular function. Sci Transl Med *13*. 10.1126/scitranslmed.abd7522.
116. Wang, H., Dey, K.K., Chen, P.C., Li, Y., Niu, M., Cho, J.H., Wang, X., Bai, B., Jiao, Y., Chepyala, S.R., et al. (2020). Integrated analysis of ultra-deep proteomes in cortex, cerebrospinal fluid and serum reveals a mitochondrial signature in Alzheimer's disease. Mol Neurodegener *15*, 43. 10.1186/s13024-020-00384-6.
117. Moore, B.D., Ran, Y., Goodwin, M.S., Komatineni, K., McFarland, K.N., Dillon, K., Charles, C., Ryu, D., Liu, X., Prokop, S., et al. (2023). A C1qTNF3 collagen domain fusion chaperones diverse secreted proteins and anti-Aβ scFvs: applications for gene therapies. Molecular Therapy Methods & Clinical Development. DOI:https://doi.org/10.1016/j.omtm.2023.101146.
118. Chakrabarty, P., Jansen-West, K., Beccard, A., Ceballos-Diaz, C., Levites, Y., Verbeeck, C., Zubair, A.C., Dickson, D., Golde, T.E., and Das, P. (2010). Massive gliosis induced by interleukin-6 suppresses Abeta deposition in vivo: evidence against inflammation as a driving force for amyloid deposition. FASEB J *24*, 548-559. fj.09-141754 [pii]10.1096/fj.09-141754.
119. Xu, G., Ran, Y., Fromholt, S.E., Fu, C., Yachnis, A.T., Golde, T.E., and Borchelt, D.R. (2015). Murine Abeta over-production produces diffuse and compact Alzheimer-type amyloid deposits. Acta Neuropathol Commun *3*, 72. 10.1186/s40478-015-0252-9.

1040 120. Levites, Y., Das, P., Price, R.W., Rochette, M.J., Kostura, L.A., McGowan, E.M., Murphy, M.P., and
1041 Golde, T.E. (2006). Anti-Abeta42- and anti-Abeta40-specific mAbs attenuate amyloid deposition
1042 in an Alzheimer disease mouse model. J Clin Invest *116*, 193-201. 10.1172/JCI25410.
1043 121. Moore, B.D., Levites, Y., Xu, G., Hampton, H., Adamo, M.F., Croft, C.L., Futch, H.S., Moran, C.,
1044 Fromholt, S., Janus, C., et al. (2022). Soluble brain homogenates from diverse human and mouse
1045 sources preferentially seed diffuse Abeta plaque pathology when injected into newborn mouse
1046 hosts. Free Neuropathol *3*. 10.17879/freeneuropathology-2022-3766.
1047 122. Naiki, H., Higuchi, K., Nakakuki, K., and Takeda, T. (1991). Kinetic analysis of amyloid fibril
1048 polymerization in vitro. Lab Invest *65*, 104-110.
1049 123. Young, M.D., Wakefield, M.J., Smyth, G.K., and Oshlack, A. (2010). Gene ontology analysis for RNA-
1050 seq: accounting for selection bias. Genome Biol *11*, R14. 10.1186/gb-2010-11-2-r14.
1051 124. Dobin, A., Davis, C.A., Schlesinger, F., Drenkow, J., Zaleski, C., Jha, S., Batut, P., Chaisson, M., and
1052 Gingeras, T.R. (2013). STAR: ultrafast universal RNA-seq aligner. Bioinformatics *29*, 15-21.
1053 10.1093/bioinformatics/bts635.
1054 125. Lawrence, M., Huber, W., Pages, H., Aboyoun, P., Carlson, M., Gentleman, R., Morgan, M.T., and
1055 Carey, V.J. (2013). Software for computing and annotating genomic ranges. PLoS Comput Biol *9*,
1056 e1003118. 10.1371/journal.pcbi.1003118.
1057 126. Love, M.I., Huber, W., and Anders, S. (2014). Moderated estimation of fold change and dispersion
1058 for RNA-seq data with DESeq2. Genome Biol *15*, 550. 10.1186/s13059-014-0550-8.
1059 127. Nikolayeva, O., and Robinson, M.D. (2014). edgeR for differential RNA-seq and ChIP-seq analysis:
1060 an application to stem cell biology. Methods Mol Biol *1150*, 45-79. 10.1007/978-1-4939-0512-
1061 6_3.
1062
1063
1064 **METHODS**
1065 Cloning and cell culture. All cDNAs used were synthesized by Genscript (Piscataway, NJ) and subcloned
1066 into pCDNA3.1 vector, the rAAV2-CBA expression vector pCTR4 [117], or both. All cDNAs incorporated a FLAG
1067 epitope tag (DYKDDDDK) on the -COOH terminal. To overexpress the genes, 2.7 µg plasmid were
1068 transiently transfected into HEK 293T cells in a 6-well dish using polyethylenimine (PEI). Media was
1069 replaced with FBS free Opti-MEM after 18 hr. incubation. Cells and conditioned media were collected after
1070 another 24 hr. incubation. Bis-Tris precast gels (Bio-Rad, Hercules, CA) were used for all SDS-PAGE. 50 µg
1071 cell lysate by total protein and 30 µl media of each sample were loaded. Western blot was developed
1072 using monoclonal anti-FLAG M2 antibody and anti-β-actin (Sigma-Aldrich, Inc, St. Louis, MO).
1073 Animal models and neonatal injections. All animal procedures were approved by the Institutional Animal
1074 Care and Use Committee in accordance with NIH guidelines. CRND8 mice were bred in house and housed
1075 three to five to a cage and maintained on ad libitum food and water with a 12hr light/dark cycleV.
1076 Intracerebroventricular injections of recombinant adeno-associated virus (rAAVs) were carried out on day
1077 P0 as described previously [118]. Two microliters of rAAV2/1 encoding Mdk and PTN was administrated
1078 bilaterally into the cerebral ventricle. Mice injected with rAAV encoding MDK and PTN were aged 3 or 6
1079 months and euthanized, brains were harvested and one hemibrain was fixed overnight in 4%
1080 paraformaldehyde at 4°C followed by processing and paraffin embedding for immunohistochemical
1081 staining. The other hemibrain was snap frozen in isopentane on dry-ice and then stored at -80°C until it
1082 was thawed and homogenized for ELISA measurements of Aβ peptide levels.
1083 Mouse Brain Histology and immunohistochemistry. Paraffin sections (5 µm) were used for all histology
1084 and immunohistochemistry studies. For various antibodies screens two hemibrains from the same mouse
1085 were fixed in EtOH or in 4% PFA (alternatively, in 10% Formalin) and embedded into the same block.
1086 Antibodies used are listed in Table S11. The slides were scanned by Aperio XT System (Leica Biosystems,

1087 Buffalo Grove, IL). Thio-S tissue staining methods were performed as previously described [119]. For studies
1088 in mice injected with pAAV-Mdk or pAAV-PTN, embedded sections were immunohistochemically stained
1089 with a biotinylated pan-Aβ antibody Ab5 [120] (1:500) or anti-FLAG antibody (Sigma-Aldrich Inc, St. Louis, IL)
1090 and developed using Vectastain Elite ABC Kit (Vector Laboratories, Burlingame, CA) followed with 3,3'-
1091 diaminobenzidine (DAB) substrate (Vector Laboratories, Burlingame, CA) and counterstained with
1092 hematoxylin. The slides were scanned by Aperio XT System and analyzed using the ImageScope program.
1093 In brief, at least three sections per sample, at least 30 µm apart, were imaged and plaque burden was
1094 quantified. For three-month old mice, plaque number was calculated by two independent observers.
1095 Human Tissue Histology and immunohistochemistry. 5 µm thick sections of formalin fixed or ethanol fixed,
1096 paraffin embedded postmortem brain tissue was deparaffinized in xylene twice for 5 minutes and
1097 followed by rehydration in descending ethanol series (100%, 100%, 90%, 70%) for 1 minute each. For
1098 Formic acid antigen retrieval, sections were immersed in a 70% Formic acid solution for 20 minutes (where
1099 indicated in Table S12). Sections were incubated in 0.1M Tris and 0.005% Tween (or Citrate buffer, where
1100 indicated in table below) at high pressure in a pressure cooker for 15 minutes, followed by incubation in
1101 a PBS/H_2O_2 solution with 10% Triton-x for 20 minutes to quench endogenous peroxidase. The sections
1102 were washed with tap water and then equilibrated to 0.1M Tris for 5 min before blocking in normal horse
1103 serum for 20 minutes, followed by blocking in 2% FBS/0.1 M Tris, (pH 7.6) for 5 minutes. After that, primary
1104 antibody, diluted in 2% FBS/0.1 M Tris, (pH 7.6) was applied to the section and incubated overnight at 4
1105 °C. Dilutions for each antiserum is listed in Table S11. The next day, sections were quickly rinsed in 0.1M
1106 Tris and blocked in 2% FBS/0.1 M Tris, (pH 7.6) for 5 minutes before incubating with the secondary
1107 antibody (HRP-conjugated ImmPRESS Polymer Reagent, Vector Labs) for 30 minutes at room temperature.
1108 Following a quick wash in 0.1M Tris, the signal was developed using 3,3'-diaminobenzidin (DAB, Vector
1109 Lab SK-410) for 1-2 minutes and then sections were counterstained with hematoxylin (Mayer's version,
1110 Sigma Aldrich) for 1 minute. Next, sections were washed in tap water, and then dehydrated in an
1111 ascending series of ethanol (70%, 90%, 100%, 100%) for 1 minute each, followed by xylene (2 x 5 mins).
1112 Sections were cover slipped using Cytoseal 60 (Thermo Fisher) mounting media and dried overnight.
1113 Aβ ELISAs. After tissue harvesting, the left hemisphere was flash-frozen in isopentane. The frozen cortex
1114 was sequentially extracted with protease inhibitor cocktail (Roche, Basel, Switzerland) containing RIPA
1115 buffer, 2% SDS, and 70% formic acid (FA) as described previously at a concentration of 150 mg/ml. Aβ
1116 levels from the 2% SDS– and 70% FA–extracted samples were quantified using end-specific sandwich ELISA
1117 as previously described [121]. Aβ40 was captured with mAb 13.1.1 and detected by HRP-conjugated mAb5.
1118 Aβ42 was captured with mAb 2.1.3 and detected by HRP-conjugated mAb5. ELISA results were analyzed
1119 using SoftMax Pro software (Molecular Devices, San Jose, CA).
1120 Amyloid-β Aggregation Assay. The effect of midkine (MDK) and pleiotrophin (PTN) proteins on amyloid
1121 beta 1-42 ($A\beta_{1-42}$) aggregation was measured by *in vitro* thioflavin T (ThT) fluorescence assay, as previously
1122 described [122]. Recombinant human $A\beta_{1-42}$ (20 ng/µL equivalent to 5 µM) from rPeptide (A-1170-1) was
1123 incubated in Tris-buffered Saline (TBS; 150 mM NaCl, 50 mM Tris-HCl, pH 7.6), and 20 µM ThT in the
1124 presence or absence of purified recombinant MDK (1.25 ng/µl equivalent to 47 nM) from Sino Biological
1125 (10247-HNAB) or PTN (5 ng/µl equivalent to 327 nM) from R&D Systems (R&D252-PL-050). The final
1126 volume within each well was 100 µL. The assay was conducted in quadruplicates using chilled (4ºC) 96
1127 well black clear bottom plates (Corning, #3904). Fluorescence was captured at 420 Ex, 480 Em for 20 hours
1128 at 15 min intervals at 37ºC using Synergy H1 (Biotek) microplate reader. ThT alone (20 µM) was measured
1129 and subtracted as background fluorescence. A titration curve was also performed with fixed concentration
1130 of $A\beta_{1-42}$ (5 µM) and an increasing concentration of MDK (12 nM, 23 nM, 47 nM and 93 nM) or PTN (82
1131 nM 163 nM and 327 nM). Fluorescence intensities were graphed using GraphPad Prism.
1132 Pulldowns and Western Blot Analysis $A\beta_{1-42}$ fibrils prepared as described above (20 hr. incubation) were
1133 precipitated by centrifugation at 10,000 x g. The pellet was resuspended in 8M urea buffer (8 M urea, 100
1134 mm $NaHPO_4$, pH 8.5) and boiled in Laemmli sample buffer (BioRad, 161-0737) at 98°C for 5 min. Proteins

1135 were resolved on Bolt 4-12% Bis-Tris gels (Thermo Fisher Scientific, NW04120BOX) followed by transfer
1136 to nitrocellulose membrane using iBlot 2 dry blotting system (ThermoFisher Scientific, IB21001).
1137 Membranes were incubated with StartingBlock buffer (ThermoFisher, 37543) for 30 min followed by
1138 overnight incubation at 4º in primary antibodies including Aβ (Novus, NBP11-97929), MDK (Abcam,
1139 #52637), and PTN (Abcam, #ab79411) antibodies. Membranes were washed with TBS containing 0.1%
1140 (v/v) Tween 20 (TBS-T) and incubated with fluorophore-conjugated secondary antibodies (Alexa Fluor-680
1141 or Alexa Fluor-800; Invitrogen) for 1 hr. at room temperature. Membranes were subsequently washed
1142 three times with TBS-T and images were captured using an Odyssey Infrared Imaging System (LI-COR
1143 Biosciences).
1144 Statistical analysis
1145 Data were analyzed statistically according to the methods specified in each figure legend. Briefly, p values
1146 were obtained as specified by either a one-way ANOVA test with two groups, or for enrichment, by a
1147 Fisher's Exact test. P values were corrected for multiple testing were indicated by Benjamini-Hochberg
1148 FDR correction. For significance of Pearson correlations, Student's test was used.
1149 Proteomic Sample Processing
1150 Each tissue piece was individually homogenized in 300 uL of urea lysis buffer (8M urea, 100 mM $NaHPO_4$,
1151 pH 8.5), including 3 uL (100x stock) HALT protease and phosphatase inhibitor cocktail (Pierce). All
1152 homogenization was performed using a Bullet Blender (Next Advance) according to manufacturer
1153 protocols. Briefly, each tissue piece was added to Urea lysis buffer in a 1.5 mL Rino tube (Next Advance)
1154 harboring 500 mg stainless steel beads (0.9-2 mm in diameter) and blended twice for 5-minute intervals
1155 in the cold room (4°C). Protein supernatants were transferred to 1.5 mL Eppendorf tubes and sonicated
1156 (Sonic Dismembrator, Fisher Scientific) 3 times for 5 s with 15 s intervals of rest at 30% amplitude to
1157 disrupt nucleic acids and subsequently vortexed. Protein concentration was determined by the
1158 bicinchoninic acid (BCA) method, and samples were frozen in aliquots at −80°C. Protein homogenates
1159 (100 ug) were diluted with 50 mM NH_4HCO_3 to a final concentration of less than 2M urea and then treated
1160 with 1 mM dithiothreitol (DTT) at 25°C for 30 minutes, followed by 5 mM iodoacetimide (IAA) at 25°C for
1161 30 minutes in the dark. Protein was digested with 1:100 (w/w) lysyl endopeptidase (Wako) at 25°C for 2
1162 hours and further digested overnight with 1:50 (w/w) trypsin (Promega) at 25°C. Resulting peptides were
1163 desalted with a Sep-Pak C18 column (Waters) and dried under vacuum.
1164 Tandem Mass Tag (TMT) Labeling
1165 Batches 1 and 2 were labeled using the TMT 11-plex kit (ThermoFisher 90406 – Lot# TG273545 and
1166 TG273555) while batch 3 was labeled with TMTPro (ThermoFisher A44520 – Lot# VH311511) according to
1167 manufacturer's protocol. For batches 1 and 2, each sample (containing 100 µg of peptides) was re-
1168 suspended in 100 mM TEAB buffer (100 µL). The TMT labeling reagents were equilibrated to room
1169 temperature, and anhydrous ACN (256 µL) was added to each reagent channel. Each channel was gently
1170 vortexed for 5 min, and then 41 µL from each TMT channel was transferred to the peptide solutions and
1171 allowed to incubate for 1 h at room temperature. The reaction was quenched with 5% (vol/vol)
1172 hydroxylamine (8 µL) (Pierce). For batch 3, each sample (containing 100 µg of peptides) was re-suspended
1173 in 100 mM TEAB buffer (100 µL). The TMT labeling reagents were equilibrated to room temperature, and
1174 anhydrous ACN (200 µL) was added to each reagent channel. Each channel was gently vortexed for 5 min,
1175 and then 20 µL from each TMT channel was transferred to the peptide solutions and allowed to incubate
1176 for 1 h at room temperature. All channels for each batch were then combined (batch 1 used all 11
1177 channels, batch 2 utilized only 10 channel and batch 3 utilized only 8 channels) and dried by SpeedVac
1178 (LabConco) to approximately 150 µL and diluted with 1 mL of 0.1% (vol/vol) TFA, then acidified to a final
1179 concentration of 1% (vol/vol) FA and 0.1% (vol/vol) TFA. Peptides were desalted with a 200 mg C18 Sep-
1180 Pak column (Waters). Each Sep-Pak column was activated with 3 mL of methanol, washed with 3 mL of
1181 50% (vol/vol) ACN, and equilibrated with 2×3 mL of 0.1% TFA. The samples were then loaded, and each

column was washed with 2×3 mL 0.1% (vol/vol) TFA, followed by 2 mL of 1% (vol/vol) FA. Elution was performed with 2 volumes of 1.5 mL 50% (vol/vol) ACN. The eluates were then dried to completeness.

High pH Fractionation

For batches 1 and 2, dried samples were re-suspended in high pH loading buffer (0.07% vol/vol NH_4OH, 0.045% vol/vol FA, 2% vol/vol ACN) and loaded onto an Agilent ZORBAX 300 Extend-C18 column (2.1mm x 150 mm with 3.5 µm beads). An Agilent 1100 HPLC system was used to carry out the fractionation. Solvent A consisted of 0.0175% (vol/vol) NH4OH, 0.01125% (vol/vol) FA, and 2% (vol/vol) ACN; solvent B consisted of 0.0175% (vol/vol) NH4OH, 0.01125% (vol/vol) FA, and 90% (vol/vol) ACN. The sample elution was performed over a 58.6 min gradient with a flow rate of 0.4 mL/min. The gradient consisted of 100% solvent A for 2 min, then 0% to 12% solvent B over 6 min, then 12% to 40 % over 28 min, then 40% to 44% over 4 min, then 44% to 60% over 5 min, and then held constant at 60% solvent B for 13.6 min. A total of 96 individual equal volume fractions were collected across the gradient and subsequently pooled by concatenation into 24 fractions. For batch 3, dried samples were re-suspended in high pH loading buffer (0.07% vol/vol NH_4OH, 0.045% vol/vol FA, 2% vol/vol ACN) and loaded onto a Waters BEH 1.7 um 2.1mm by 150mm. A Thermo Vanquish was used to carry out the fractionation. Solvent A consisted of 0.0175% (vol/vol) NH_4OH, 0.01125% (vol/vol) FA, and 2% (vol/vol) ACN; solvent B consisted of 0.0175% (vol/vol) NH_4OH, 0.01125% (vol/vol) FA, and 90% (vol/vol) ACN. The sample elution was performed over a 25 min gradient with a flow rate of 0.6 mL/min. A total of 192 individual equal volume fractions were collected across the gradient and subsequently pooled by concatenation into 96 fractions. All fractions were dried to completeness using a SpeedVac.

Liquid Chromatography Tandem Mass Spectrometry

For batches 1 and 2, each of the 24 high-pH peptide fractions was resuspended in loading buffer (0.1% FA, 0.03% TFA, 1% ACN). Peptide eluents were separated on a self-packed C18 (1.9 µm Dr. Maisch, Germany) fused silica column (50 cm × 75µM internal diameter (ID), New Objective, Woburn, MA) by an Easy nLC 1200 (Thermo Scientific) and monitored on a Q-Exactive HFX mass spectrometer (Thermo Scientific). Elution was performed over a 120-min gradient at a rate of 250 nL/min or 300 nL/min with buffer B ranging from 3% to 50% (buffer A: 0.1% FA in water, buffer B: 0.1 % FA in 80% ACN). For batch 1, the mass spectrometer was set to acquire data in positive ion mode using data-dependent acquisition with top 20 cycles. Each cycle consisted of one full MS scan followed by a maximum of 20 MS/MS. Full MS scans were collected at a resolution of 120,000 (400-1600 m/z range, 1×10^6 AGC, 100 ms maximum ion injection time). All higher energy collision-induced dissociation (HCD) MS/MS spectra were acquired at a resolution of 45,000 (1.6 m/z isolation width, 0.5 m/z offset, 32% collision energy, 1×10^4 AGC target, 86 ms maximum ion time). Dynamic exclusion was set to exclude previously sequenced peaks for 20 seconds within a 10-ppm isolation window. For batch 2, the mass spectrometer was set to acquire data in positive ion mode using data-dependent acquisition with top 10 cycles. Each cycle consisted of one full MS scan followed by a maximum of 10 MS/MS. Full MS scans were collected at a resolution of 120,000 (400-1600 m/z range, 3×10^6 AGC, 100 ms maximum ion injection time). All higher energy collision-induced dissociation (HCD) MS/MS spectra were acquired at a resolution of 45,000 (1.6 m/z isolation width, 0.5 m/z offset, 30% collision energy, 1×10^4 AGC target, 86 ms maximum ion time). Dynamic exclusion was set to exclude previously sequenced peaks for 20 seconds within a 10-ppm isolation window.

For batch 3, each of the 96 high-pH fractions was resuspended in loading buffer (0.1% FA, 0.03% TFA, 1% ACN). Peptide eluents were separated on a self-packed C18 (1.7 µm Water's BEH) fused silica column (laser pulled 15 cm × 150µM ID) by Ultimate 3000 RSLCnano (Thermo Scientific). Elution was performed over a 36-min gradient at a rate of 1ul/min with buffer B ranging from 3% to 50% (buffer A: 0.1% FA in water, buffer B: 0.1 % FA in 80% ACN). Mass spectrometry was performed with a high-field asymmetric waveform ion mobility spectrometry (FAIMS) Pro frontend equipped Orbitrap Eclipse (Thermo) in positive ion mode using data-dependent acquisition with 1.5 second top speed cycles for each FAIMS compensative voltage (CV). Each cycle consisted of one full MS scan followed by as many MS/MS events

1230 that could fit within the given 1.5 second cycle time limit. MS scans were collected at a resolution of
1231 120,000 (410-1600 m/z range, 4x10^5 AGC, 50 ms maximum ion injection time, FAIMS CV of -45 and -65).
1232 Only precursors with charge states between 2+ and 6+ were selected for MS/MS. All higher energy
1233 collision-induced dissociation (HCD) MS/MS spectra were acquired at a resolution of 30,000 (0.7 m/z
1234 isolation width, 35% collision energy, 1.25^5 AGC target, 54 ms maximum ion time, turboTMT on).
1235 Dynamic exclusion was set to exclude previously sequenced peaks for 20 seconds within a 10-ppm
1236 isolation window.
1237 Proteome Identification and Quantification with Proteome Discoverer
1238 All raw files were analyzed using Proteome Discoverer v2.5.0.400 (ThermoFisher Scientific). MS/MS
1239 spectra were compared to theoretical spectra in a search performed by the Sequest HT search engine,
1240 with parameters specified as: fully tryptic specificity, a maximum of two missed cleavages, a minimum
1241 peptide length of six, fixed modifications for TMT or TMTPro tags on lysine residues and peptide N-termini
1242 (respectively +229.163 or +304.207 Da), carbamidomethylation of cysteine (+57.021 Da), and dynamic
1243 modification of methionine oxidation (+15.995 Da) and N-terminal protein loss of methionine, methionine
1244 loss plus acetylation, or acetylation (-131.040 Da, -89.030 Da, or +42.011 Da, respectively); precursor mass
1245 tolerance was 20 ppm, and Fragment tolerance 0.05 Da. The FASTA database searched was downloaded
1246 from UniProt on August 15, 2020, and contained 91,413 entries, plus one added for human amyloid beta
1247 residues 6-28 (HDSGYEVHHQKLVFFAEDVGSNK). Correction for stable isotope labeling impurity of the TMT
1248 tags used in each of the 3 batches was performed. Proteins reported in the consensus workflow were
1249 filtered by Percolator to 0.005 FDR-passed 1,266,002 PSMs, 0.01 FDR-passed 310,145 peptide groups, and
1250 0.05 FDR-passed 49,656 proteins, including decoys in each case. Strict parsimony principles were followed
1251 to group peptides into proteins so that 11,681 protein parsimony groups represent the full results. A
1252 complete protein-level TMT reporter normalized abundance table is available in Table S3.
1253 Bioinformatic Analyses
1254 Circular heatmap plot of eigenprotein-trait correlations (bicor), native eigenprotein -$\log_{10}$(p) for signed
1255 significance of AD vs control or synthetic eigenprotein Tg vs WT comparison, and the -$\log_{10}$(BH FDR) of cell
1256 type marker enrichment from the one-tailed Fisher's test p value was visualized using the R circlize
1257 package suite of functions using an in-house script. Synthetic eigenprotein calculations used the top 20
1258 percent of hubs ranked by kME, a minimum of 4 hubs per module, calculating the first principal
1259 component of variance in those hubs [9] after mapping cross-species using the biomaRt R package getLDS
1260 function. Effect size correlation plots leveraged the WGCNA verboseScatterplot function for Pearson rho,
1261 least squares fit line, and Student's significance of the Pearson correlation. Boxplots were drawn using the
1262 base R boxplot function, with individual points overlain using the beeswarm package function of the same
1263 name. The stacked bar plot of percent differentially expressed proteins per module was executed using
1264 the DEXpercentStacked function available from https://www.github.com/edammer/parANOVA/.
1265 Ensemble human AD GWAS MAGMA p values (Table S1) were determined as the mean -$\log_{10}$(p) gene-
1266 level risk for all genes reaching nominal significance in any of the three GWAS studies considered [43-45],
1267 following rollup of SNP-level GWAS summary statistics to the gene-level p value using MAGMA v1.09b.
1268 Gene Ontology Analyses.
1269 Gene ontology enrichment analysis were performed with goseq [123] to identify enrichment in gene
1270 ontology categories and KEGG pathways. For DEGs, up- and down-regulated gene lists will be analyzed
1271 separately. For WGCNA, gene lists from each module will be used as input. Over-represented P-values will
1272 be adjusted for multiple comparisons using the Benjamini–Hochberg (BH) adjustments for controlling
1273 false-discovery rates. An enrichment score will be calculated using an observed-over-expected ratio for
1274 each gene list. GO-BP categories and KEGG pathways were plotted if their BH adjusted FDR reached >=
1275 0.05 and the number of DEGs within each category/pathway was greater than 4. Individual GO terms were
1276 grouped based on their similarity of gene composition computed using the Jaccard similarity index where
1277 J(A,B) = |size of A intersection B| / |size of A union B|. These groupings were then expert-annotated based

on the overarching main function and theme of their constituent members into supergroups. The mean enrichment and p-values for the union of all member GO terms for each supergroup were calculated for graphing.

RNA extraction, sequencing and analyses for 18M mouse brains. RNA sequencing data for TgCRND8 transgenic mice was downloaded from Synapse (https://doi.org/10.7303/syn3157182). RNA was extracted using the RNeasy mini extraction kit with on-column DNase treatment (QIAGEN). RNA quantity is determined with the Qubit RNA HS assay. RNA quality will be checked via the RNA Integrity Number (RIN) on an Agilent Bioanalyzer 2100 with the Eukaryote Total RNA Nano chip. Libraries will be generated polyA enrichment using the Illumina TruSeq Stranded mRNA library prep kit. Libraries will be sequenced on paired-end, 100 bp runs on the Nextseq 2000 (Illumina) utilizing a pooling strategy that minimized batch effects from extraction, library preparation.

IFASTQ files were aligned against the mouse genome (GRCm39) and GRCm39.107 annotation using STAR [124] to generate BAM files. Gene counts were generated from BAM files using Rsamtools (https://bioconductor.org/packages/release/bioc/html/SummarizedExperiment.html) and the summarizeOverlaps function with the GenomicAlignments package v1.36.0 [125] . Differential gene expression analysis was performed with DESeq2 package v1.40.2 using the “DESeq” function with default settings [126] which fits a generalized linear model for each gene. Subsequent Wald test P-values are adjusted for multiple comparisons using the Benjamini–Hochberg method (adjusted P-value). Pair-wise changes in gene expression levels between groups were used to identify DEGs. DEGs will be defined as an absolute log2 fold change ≥0.5 and an adjusted P-value ≤0.05.IFASTQ files were aligned against the mouse genome (GRCm39) and GRCm39.107 annotation using STAR [124] to generate BAM files. Gene counts were generated from BAM files using Rsamtools (https://bioconductor.org/packages/release/bioc/html/SummarizedExperiment.html) and the summarizeOverlaps function with the GenomicAlignments package v1.36.0 [125] . Differential gene expression analysis was performed with DESeq2 package v1.40.2 using the “DESeq” function with default settings [126] which fits a generalized linear model for each gene. Subsequent Wald test P-values are adjusted for multiple comparisons using the Benjamini–Hochberg method (adjusted P-value). Pair-wise changes in gene expression levels between groups were used to identify DEGs.

AMP-AD brain transcriptome and proteomic datasets. Brain transcriptome dataset from Mayo Clinic on the AD Knowledge Portal was utilized for human vs mouse DEG comparisons). Human and CRND8 mouse brain RNA sequencing data was downloaded from Synapse (doi: https://doi.org/10. 7303/syn5550404; https://www.synapse.org/#!Synapse:syn17008858). Mayo RNAseq dataset comprises transcriptome measures from temporal cortex (TCX, superior temporal gyrus) and cerebellum (CER) the former of which was utilized in this study. For Non-Tg mice and CRND8 mice a sagitally dissected whole hemibrain was used. RNA isolation, data collection, sequencing alignment, counting and QC has been described in detail elsewhere [12,30,76]. EdgeR was used to reprocess both the mouse and human RNA sequencing data [127]. Mouse and human orthologues were identified in a two-step process. Most orthologous genes were first identified using http://alliancegenome.org/downloads, Database Version: 5.4.0 on Apr 20, 2023, with "Orthology Filter: Stringent". Then a manual curation of additional orthologues was conducted using the gOrth serac function on the g:profiler website (https://biit.cs.ut.ee/gprofiler/orth). Human brain proteomic data was utilized form previous publications. The human proteome data is available at Synapse (https://www.synapse.org/#!Synapse:syn20933797/wiki/596247).

1321 **FIGURE LEGENDS**
1322
1323 **Figure 1. TMT-MS analysis and gene ontologies of CRND8 mice versus non-Tg brains.**
1324 (A) Volcano plot of the 6M CRND8 cohort.
1325 (B) Volcano plot of the 12M CRND8 cohort.
1326 (C) Volcano plot of the 18M CRND8 cohort.
1327 (D) Correlation of CRND8 brain DEPs between the 12M (x) and 18M cohorts (y).
1328 (E) Thematic grouping of gene ontology categories of DEPs increased in all CRND8 cohorts.
1329 (F) Thematic grouping of gene ontology categories of DEPs decreased in all CRND8 cohorts.
1330 (G) Thematic grouping of gene ontology categories of DEPs (log 2 Fc > 0.2) and increased by >2 fold in the
1331 18M CRND8 cohort relative to the 6M cohort.
1332 (H) Thematic grouping of gene ontology categories of DEPs (log 2 Fc > 1) and increased by >2 fold in the
1333 18M CRND8 cohort relative to the 6M cohort.
1334 (I) Thematic grouping of gene ontology categories of DEPs (log 2 Fc < -0.1) and decreased by >2 fold in the
1335 18M CRND8 cohort relative to the 6M cohort.
1336 Lists of all genes used for gene ontology analyses are provided in Table S7.
1337
1338 **Figure 2. Integrated mouse and human brain proteome comparison reveals concordant and discordant**
1339 **changes between CRND8 mice brains and human AD.**
1340 (A) 7588 mouse orthologs of human brain proteins quantified in both proteomes of the consensus human
1341 AD brain proteome (AD vs. Ctrl) and the 18M mice (CRND8 Tg vs non-Tg) are compared by their effect size
1342 (log 2 Fc) in human (x) vs. mouse (y). Red numbers indicate number of proteins in each quadrant.
1343 (B) Proteins in panel A were filtered to retain only orthologs nominally significantly changed in both human
1344 and the 18M mice.
1345 (C) 6794 mouse orthologs of human brain proteins quantified in both proteomes of the consensus human
1346 AD brain proteome (AD vs. Control) and the 6M mice (CRND8 Tg vs non-Tg) are compared by their effect
1347 size in human (x) vs. mouse (y).
1348 (D) Proteins in panel C were filtered to retain only orthologs nominally significantly changed in both
1349 human and the 6M mice.
1350 (E) Overview of human consensus brain proteome mapping to the CRND8 mouse brain shows trait
1351 correlations in human (outer two tracks; red, positive correlation to white, no correlation, to blue,
1352 negative correlation), effect size directionality and significance for AD (third track from the outside), the
1353 effect size directionalities and significance for CRND8 Tg vs. non-Tg at 6M, 12M, and 18M in cognate
1354 mouse synthetic modules (Synth eigenproteins, EP), and hypergeometric overlap significance with cell
1355 type marker lists, indicating cell type enrichment of modules in the innermost track. Modules are
1356 numbered M1 to M44, ordered by bicor correlation relatedness (dendrogram), from M6, top left, to M37,
1357 top right, in a counterclockwise direction.
1358 (F) The 44 consensus modules were assessed for fraction of module member proteins achieving
1359 differentially expressed protein (DEP) status, discerning decreased DEPs in disease or Tg as blue, and
1360 increased DEPs as red in a stacked bar chart. Human and mouse bars for each module are shown side-by-
1361 side, left and right, respectively, above each module description. Descriptions below the numbered
1362 identifiers match the order of modules presented in the previous panel (*arrow*). The color of description
1363 text indicates concordant increases (red), decreases (blue), discordant in direction of change (gold), or
1364 non-concordant (black).
1365 (G) Mouse orthologs CRND8 18M Tg vs. non-Tg effect sizes are compared to the AD vs. Control effect sizes,
1366 module by module, with selected modules shown here. Pearson correlation rho and Student's significance
1367 of correlation are provided along with the number of orthologues mapping to each consensus module
1368 plotted. Text color of each module plot title matches the scheme described for the previous panel.

1369 **Figure 3. Consensus human AD brain synthetic module eigenproteins in mouse show transient and/or**
1370 **age-progressive CRND8 Tg effects.**
1371 Nine consensus human modules are shown for the network of healthy control, pathology-bearing
1372 asymptomatic AD (AsymAD), and symptomatic AD (AD) individuals totaling N=488 (*left panels*). To the
1373 right, the mouse orthologs of hub proteins for these modules were used to calculate the first principal
1374 component of variance in the 6M, 12M, and 18M mouse proteomes, allowing for extrapolation of the
1375 modules into Tg and non-Tg mice, determination of effect size by module in each mouse cohort, and the
1376 significance of Tg effect within each module. Significant one-way ANOVA p values are colored red. Note
1377 the Y-axis are different across ages, and in many modules the eigenprotein change between Tg and non-
1378 Tg mice increases dramatically with age.
1379
1380 **Figure 4. Mdk/MDK and Ptn/PTN colocalize with Aβ in amyloid plaques and CAA in CRND8 mice and**
1381 **human AD.**
1382 (A) Paraffin slides containing brain tissue from 15-18M CRND8 mice were stained with mouse anti-pan-
1383 Aβ, sheep anti-Mdk or rabbit anti-Ptn antibodies. Low magnification (scale 500 μm) images and high
1384 magnification (inset, scale 50 μm) were taken from cortex (plaques) and cerebellum (CAA).
1385 (B) Representative low magnification (scale 100 μm) and high magnification (inset, scale 30 μm) of
1386 postmortem paraffin embedded tissue sections of human frontal cortex from patients with high AD
1387 neuropathological changes stained for MDK and PTN.
1388 (C) Plaques on paraffin slides containing brain tissue from old CRND8 mice were stained with anti-Mdk
1389 and anti-Ptn antibodies and visualized with fluorescent secondary antibodies (anti-rabbit green and anti-
1390 sheep red), scale 50 μm.
1391 (D) Plaques and CAA on paraffin slides containing brain tissue from old CRND8 mice were stained with
1392 anti-pan-Aβ, anti-Mdk or anti-Ptn antibodies and visualized with Thio-S (green) or fluorescent secondary
1393 antibodies (anti-mouse red, anti-rabbit red, anti-sheep red), scale 50 μm.
1394
1395 **Figure 5. M42+ DEPs colocalize with amyloid pathology.**
1396 Brain tissue from 15-18M CRND8 mice were stained with the anti-sera against the indicated proteins. Anti-
1397 pan-Aβ antibody served as a reference for amyloid pathology, secondary antibody alone – as a negative
1398 control. All proteins are listed in order of log 2 Fc (highest to lowest). Low magnification (scale 200 μm)
1399 images and high magnification (inset, scale 50 μm). See Figure S7 for non-Tg staining.
1400 (A) DEPs in amyloid plaques in the CRND8 cortex.
1401 (B) DEPs detected in CAA in the cerebellum.
1402 (C) DEPs detected in dystrophic processes surrounding amyloid plaques in the cortex.
1403 (D) Representative low magnification (scale 100 μm) and high magnification (inset, scale 30 μm) of
1404 postmortem paraffin embedded tissue sections of human frontal cortex from patients with high AD
1405 neuropathological changes stained for Aβ, EGFL8, C1QTNF4, COL25A1, HGF, APOD, SDC4, NTN1, SMOC2,
1406 OLFML3, SPOCK3, SPOCK1, SULF1, SFRP5 and SFRP1. There is selective staining of plaques by antisera for
1407 COL25A1, SDC4, NTN1, SMOC2, and EGFL8. Weaker staining of plaques and cellular staining is observed
1408 for HGF, C1QTNF4 and APOD. Dystrophic processes are stained with anti-serum to SPOCK3, SPOCK1
1409 OLFML3. Glial cells are detected with anti-sera to SULF1, SRRP5 and SFRP1.
1410
1411 **Figure 6. Mdk and PTN overexpression increase parenchymal Aβ amyloid deposition and CAA in 6M**
1412 **CRND8 mice.** Mice were intracerebrally injected with rAAV2/8-Mdk, rAAV2/8-PTN or not injected
1413 (control) at P0 and aged 6 months.
1414 (A, B) Representative images of cortex and hippocampus 9A) or CAA (B) stained with biotinylated anti-Aβ
1415 mAb 33.1.1 (anti-Aβ 1-16). Scale bar: 500 μm, 50 μm (inset). Quantification data of the entire brain plaque

count in three non-consecutive sections represented by a scatter dot plot of male (closed circle/square) and female (open circle/square) ± standard error of the mean. n=5-15. Statistical analyses by one-way ANOVA test (*, $p<0.05$; ***, $p<0.001$).
(C) RIPA, 2% SDS and 70% formic acid (FA) extracted Aβ42 and Aβ40levels were detected by ELISA and plotted as scatter dot plot of male (closed circle/square) and female (open circle/square) ± standard error of the mean. n=5-12. Aβ42 and Aβ40 levels were quantified with corresponding one-way ANOVA and paired comparison test (*, $p<0.05$; **, $p<0.01$, ***, $p<0.001$).
(D) MDK and PTN accelerate amyloid aggregation in vitro as detected by real time Thioflavin T (ThT) assay.

Figure 7. Amyloid binding and co-localization in TTR amyloids.
(A) M42+ proteins secreted into the media of transiently transfected HEK cells bind to Aβ42 and AVS amyloids. Data are representative of three independent experiments.
(B) Representative images of immunohistochemical stains for MDK, PTN or Thio-S on human cardiac amyloidosis sections. Scale bar, 50 µm.

Availability of data and materials
Raw mass spectrometry data and pre- and post-processed plasma protein abundance data and case traits related to this manuscript are available at https://synapse.org/CRND8. The results published here are in whole or in part based on data obtained from the AMP-AD Knowledge Portal (https://adknowledgeportal.synapse.org). The AMP-AD Knowledge Portal is a platform for accessing data, analyses and tools generated by the AMP-AD Target Discovery Program and other programs supported by the National Institute on Aging to enable open-science practices and accelerate translational learning. The data, analyses and tools are shared early in the research cycle without a publication embargo on secondary use. Data are available for general research use according to the following requirements for data access and data attribution (https://adknowledgeportal.synapse.org/#/DataAccess/Instructions).

AD Knowledge Portal: AMP-AD datasets: The results published here are in whole or in part based on data obtained from the AMP-AD Knowledge Portal (https:// doi. org/ 10. 7303/ syn25 80853). Mayo Clinic: The Mayo RNAseq study data was led by Dr. Nilüfer Ertekin-Taner, Mayo Clinic, Jacksonville, FL as part of the multi-PI U01 AG046139 (MPIs Golde, Ertekin-Taner, Younkin, Price). Samples were provided from the following sources: The Mayo Clinic Brain Bank and Banner Sun Health Research Institute. Data collection was supported through funding by NIA grants P50 AG016574, R01 AG032990, U01 AG046139, R01 AG018023, U01 AG006576, U01 AG006786, R01 AG025711, R01 AG017216, R01 AG003949, NINDS grant R01 NS080820, CurePSP Foundation, and support from Mayo Foundation. Study data includes samples collected through the Sun Health Research Institute Brain and Body Donation Program of Sun City, Arizona. The Brain and Body Donation Program is supported by the National Institute of Neurological Disorders and Stroke (U24 NS072026 National Brain and Tissue Resource for Parkinson's Disease and Related Disorders), the National Institute on Aging (P30 AG19610 Arizona Alzheimer's Disease Core Center), the Arizona Department of Health Services (contract 211002, Arizona Alzheimer's Research Center), the Arizona Biomedical Research Commission (contracts 4001, 0011, 05-901 and 1001 to the Arizona Parkinson's Disease Consortium) and the Michael J. Fox Foundation for Parkinson's Research. For the human protein data All raw data, case traits and analyses (differential and co-expression) related to this manuscript are available at https://www.synapse.org/consensus. The results published here are in whole or in part based on data obtained from the AMP-AD Knowledge Portal (https://adknowledgeportal.synapse.org). The AMP-AD Knowledge Portal is a platform for accessing data, analyses, and tools generated by the Accelerating Medicines Partnership (AMP-AD) Target Discovery

Program and other National Institute on Aging (NIA)-supported programs to enable open-science practices and accelerate translational learning. The data, analyses and tools are shared early in the research cycle without a publication embargo on secondary use. Data is available for general research use according to the following requirements for data access and data attribution (https://adknowledgeportal.synapse.org/#/DataAccess/Instructions). ROSMAP resources can be requested at www.radc.rush.edu.

ACKNOWLEDGEMENTS

Author contributions: Conceptualization, TEG, NTS, SP, AIL, YL, ECBJ, ED; Methodology, TEG, YL, YR, DD, JG, NTS, MA, KD, DR, JT, CM, LP, AI, AE, BDM, KDD, AN, TI, FA, TL, KM, BM, MR, CF; Investigation, YL, EBD, YR, WT, DD, MA, JG, KL , JT-L, JP, AI, AE, BM, KM, AN; Formal Analysis, YL, KM, EBD, MR, CF, NTS, TEG, AN; Writing – Original Draft, TEG, YL, SP; Writing – Review & Editing, YL, EBD, DD, NET, JWK, AIL, KM, NTS, TEG, SP, FLH; Funding Acquisition, TEG, SP, NTS, YL AIL and; Resources, AIL, JWK, NTS, SP, TEG, ECBJ, FLH, JWK, JJ; All authors read and approved the final manuscript.

Funding: This study was supported by the following National Institutes of Health (NIH) funding mechanisms: P30AG066506, U01AG061357, U01AG046139 (TEG and NET), U01AG061357, RF1AG074569 (AIL and NTS), RF1AG062181 (NTS) and P30AG066511 (AIL) and the Foundations for the National Institute of Health AMP-AD 2.0 grant. This work was supported by the Deutsche Forschungsgemeinschaft (DFG, German Research Foundation) under Germany's Excellence Strategy NeuroCure– EXC-2049 – 390688087 to F.L.H., as well as HE 3130/6-1 to F.L.H. Additional support for these studies was provided by the NIA grants R01-AG061796 (NET), U19-AG074879 (NET), Alzheimer's Association Zenith Fellows Award (NET).

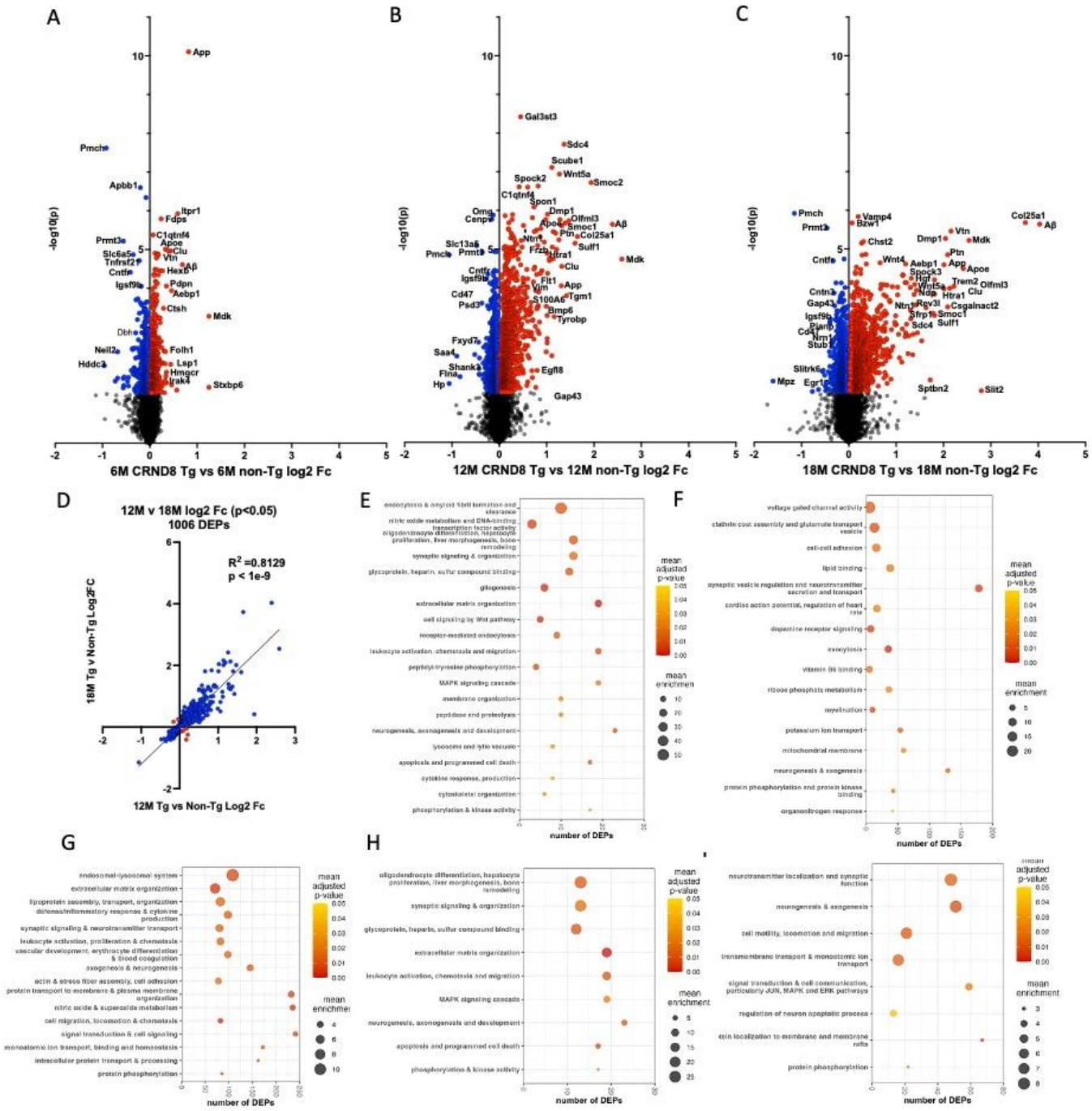

Figure 1. TMT-MS analysis and gene ontologies of CRND8 mice versus non-Tg brains.

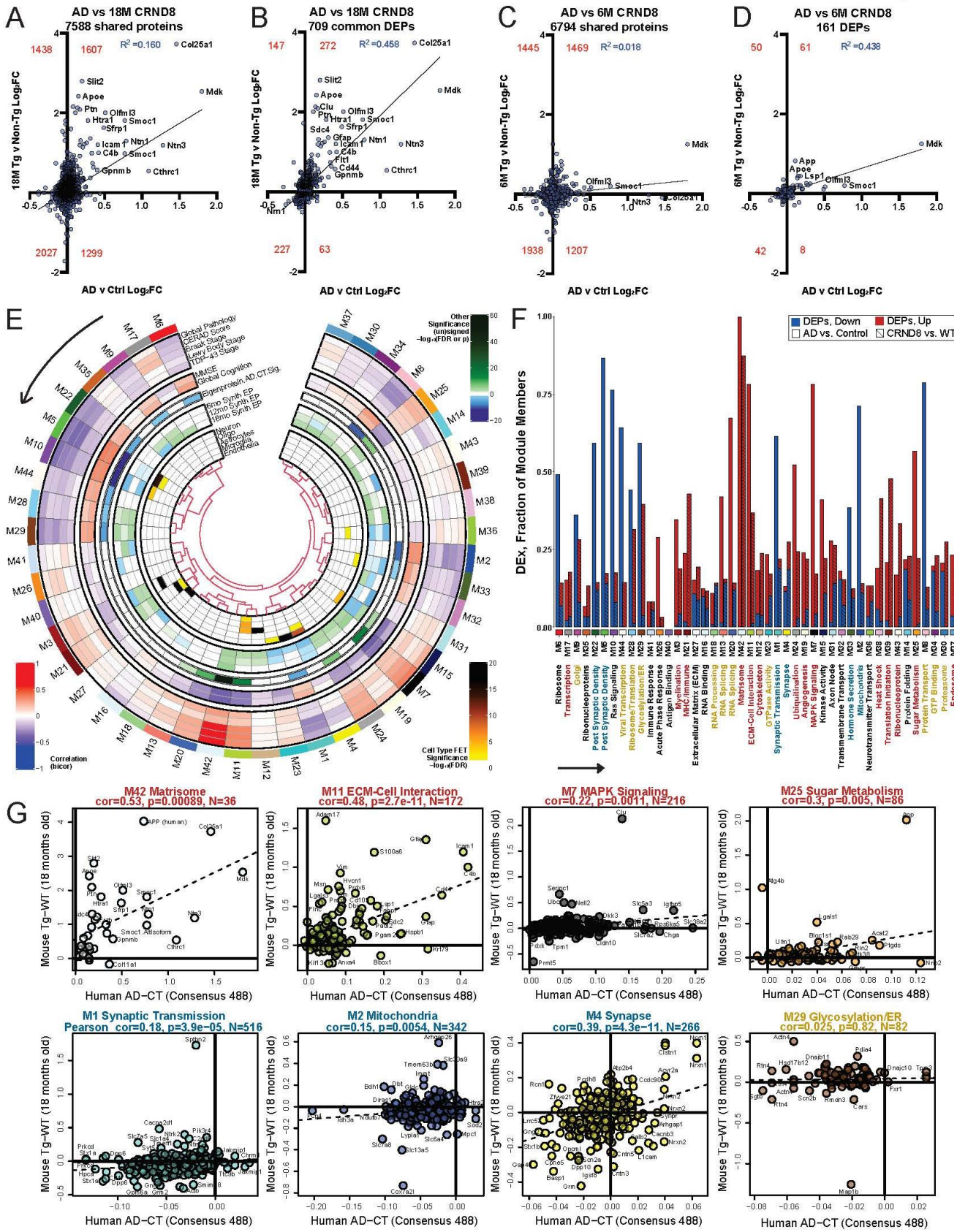

Figure 2. Integrated mouse and human brain proteome comparison reveals concordant and discordant changes between CRND8 mice brains and human AD.

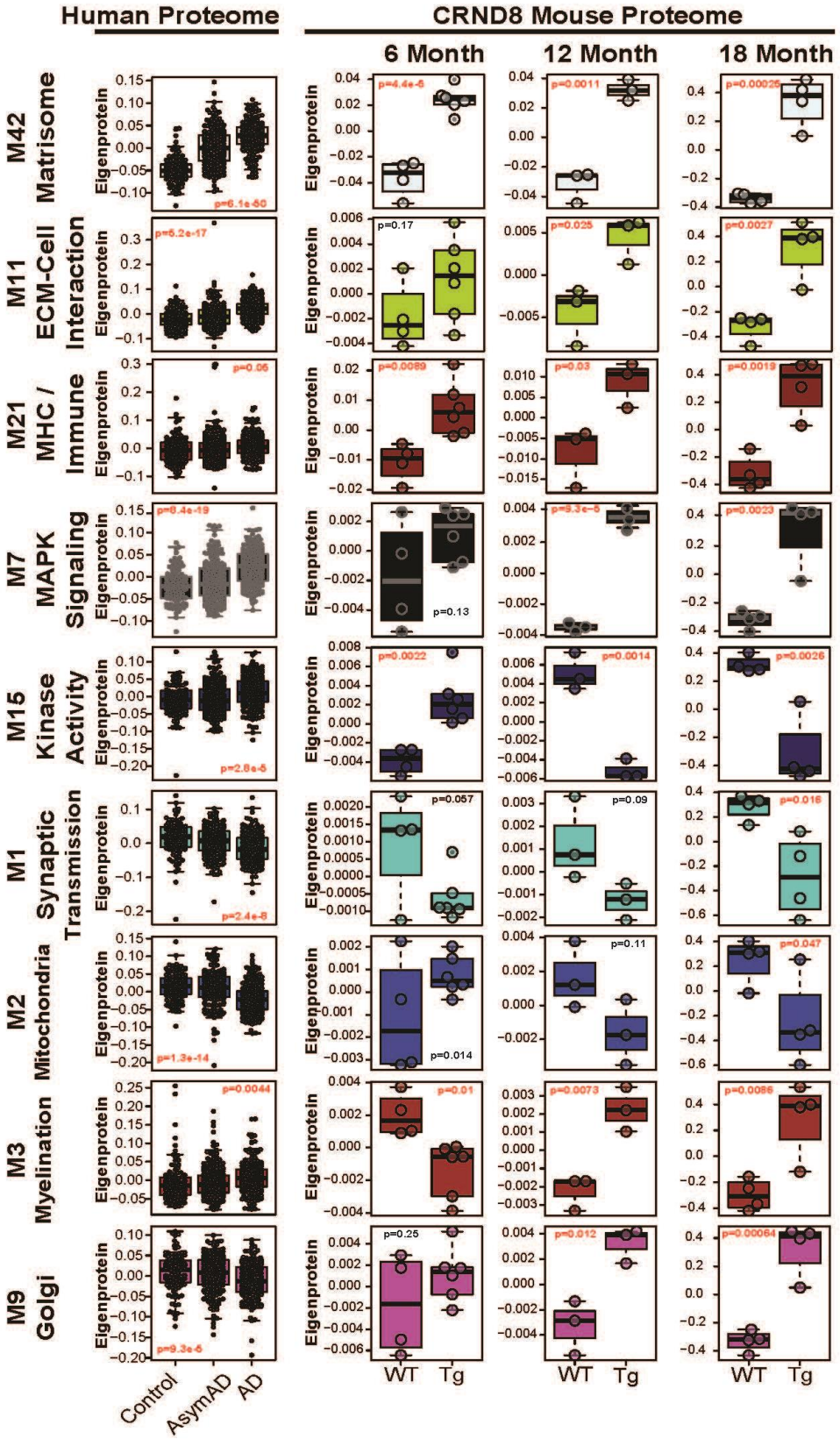

Figure 3. Consensus human AD brain synthetic module eigenproteins in mouse show transient and/or age-progressive CRND8 Tg effects.

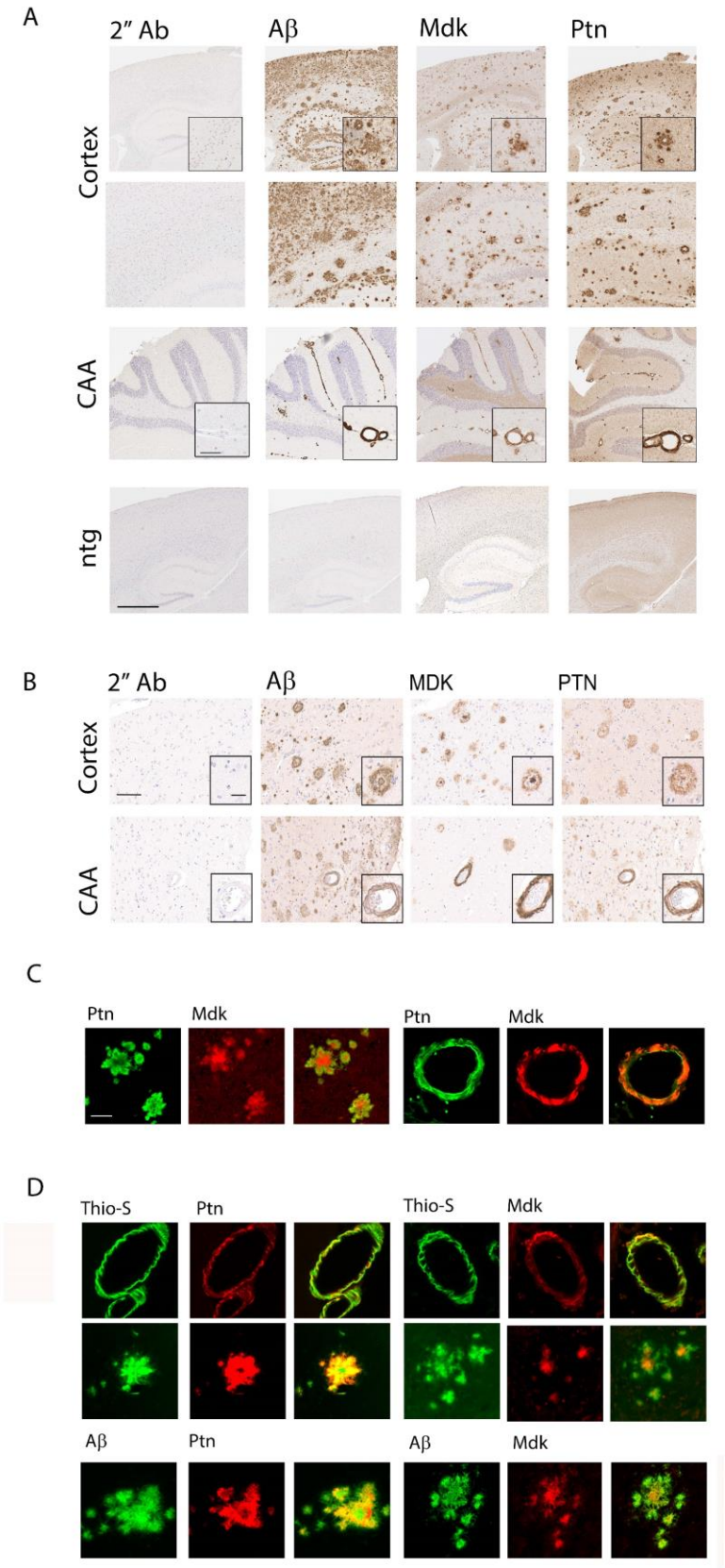

Figure 4. Mdk/MDK and Ptn/PTN colocalize with Aβ in amyloid plaques and CAA in CRND8 mice and human AD.

1

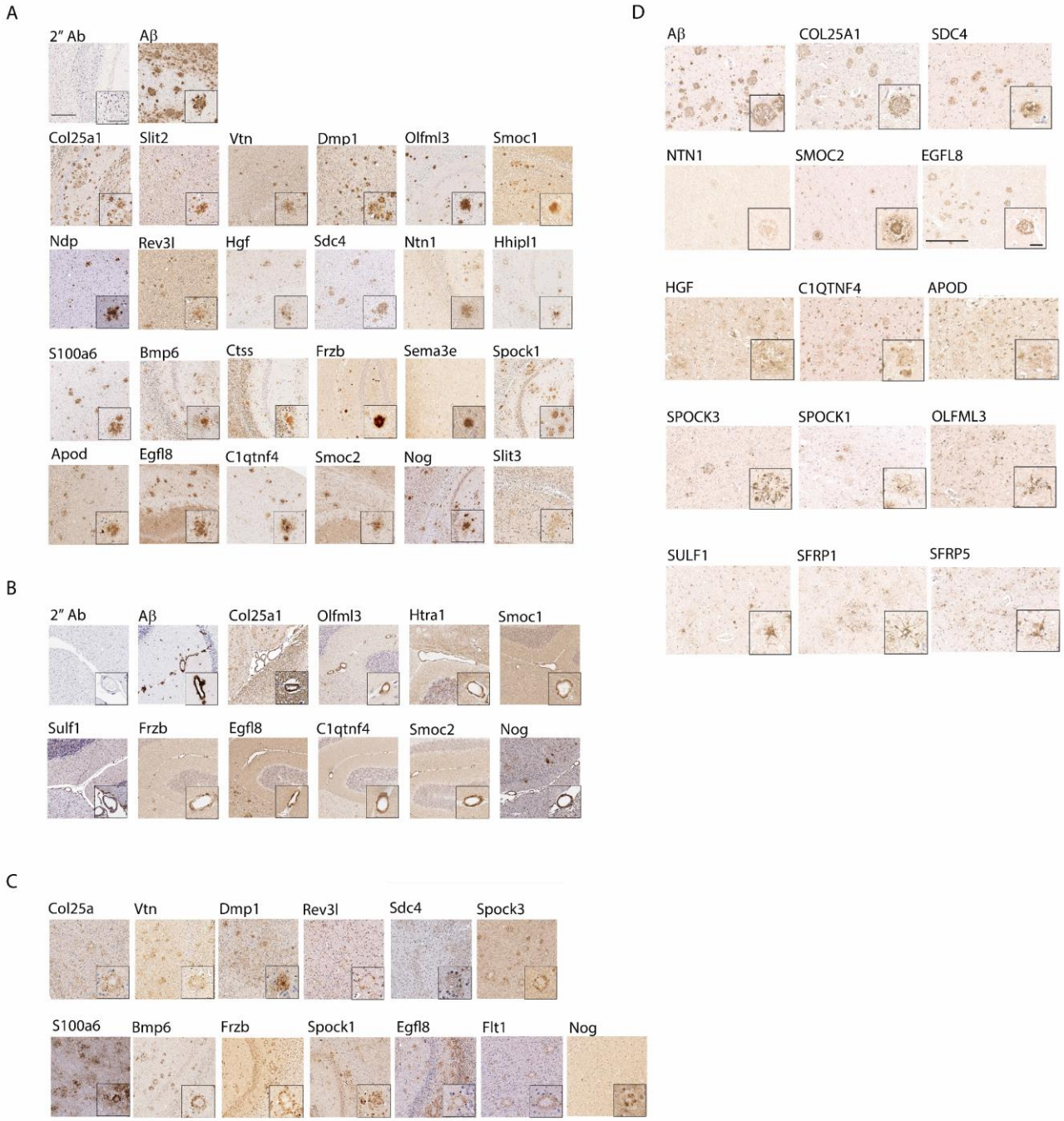

Figure 5. M42+ DEPs colocalize with amyloid pathology.

1492

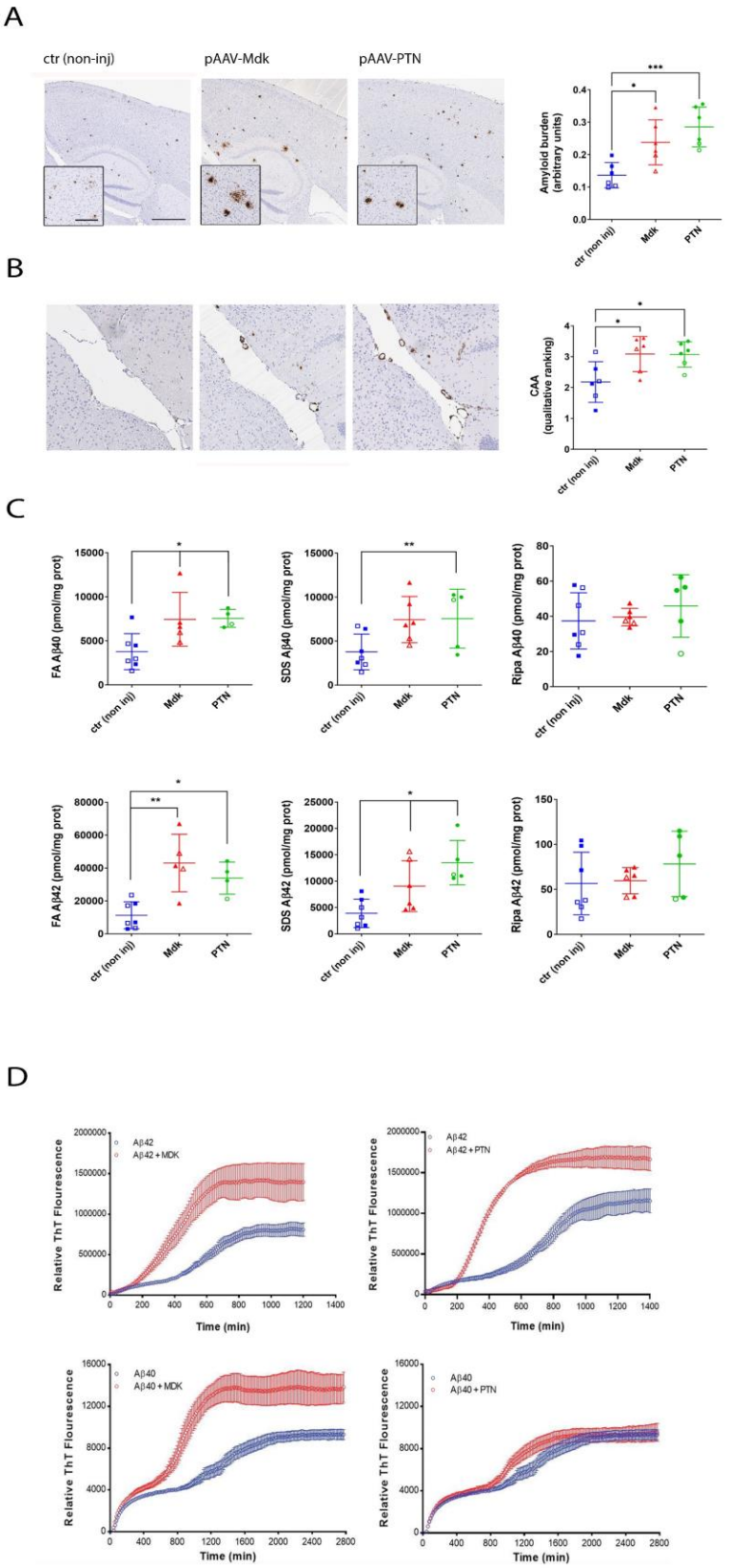

Figure 6. Mdk and PTN overexpression increase parenchymal Aβ amyloid deposition and CAA in 6M CRND8 mice.

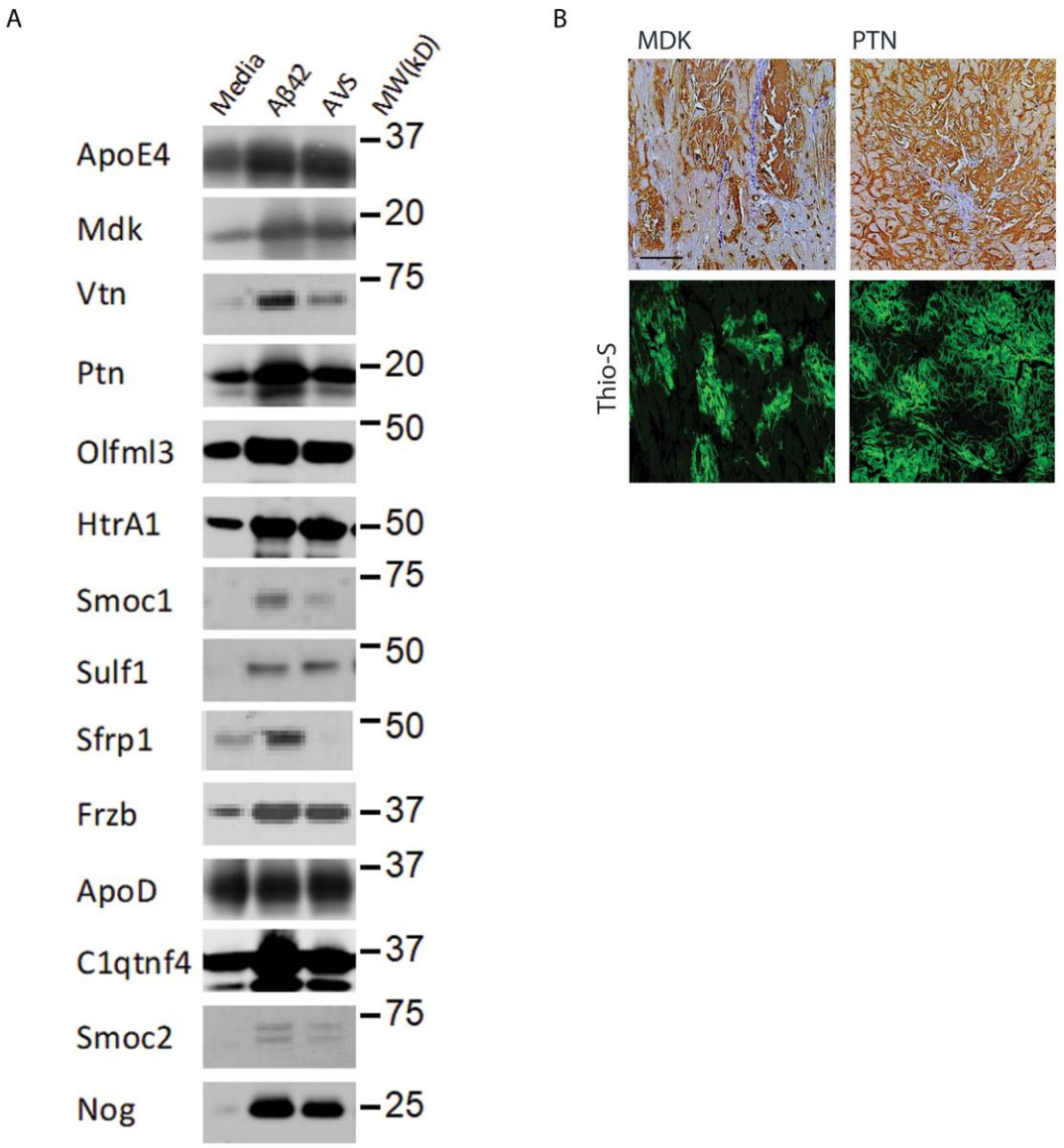

Figure 7. Amyloid binding and co-localization in TTR amyloids.

1494 **Supplemental material**

1495 **Figure legends**

1496 **Figure S1. Correlation of protein encoding mRNAs in 20M CRND8 mice (Tg versus non-Tg) and AD versus**
1497 **Control human Temporal Cortex.**

1498 Previously generated RNA expression data from human temporal cortex [12] and CRND8 mice brains [30] was
1499 reanalyzed using EdgeR and filtered for orthologues.

1500 (A) Plot of log2FC of human temporal cortex AD versus Control mRNA levels (x-axis) and 20M CRND8 of
1501 orthologous protein coding RNA (y-axis).

1502 (B) Plot of log2FC of human temporal cortex AD versus Control mRNA levels (x-axis) and 20M CRND8 of
1503 shared DEGs of protein coding genes (y-axis).

1504 Data used to generate these plots is found in Table S6.

1505

1506 **Figure S2. Effect size correlation for human AD vs control effect and mouse Tg effect at 18M shows**
1507 **varying concordance in each of the 44 consensus brain modules.**

1508 Panels are in rank size order from M1 to M44, with each title providing module number, description,
1509 Pearson correlation (rho), Student's significance of correlation, number of mouse orthologs mapped to
1510 the members of the human module, and all points labeled by the gene symbol of the mouse ortholog.
1511 *Modules also displayed in Figure 2 are labeled with an asterisk. Text color of each module plot title
1512 matches the scheme described in Figure 2F.

1513

1514 **Figure S3. Synthetic eigenproteins (modules) show trends across the three cohorts of aged Tg and non-**
1515 **Tg mice for all 44 consensus brain modules.** All 44 human modules were calculated as synthetic
1516 eigenproteins in the mouse proteomics and plotted as boxplots. Boxes represent the second to third
1517 interquartile range; whiskers represent the 5th to 95th percentiles; and the horizontal line within each box
1518 represents the median value.

1519

1520 **Figure S4. RNA-Protein AD or Tg Effect Size Correlation, in total and within modules.**

1521 (A) The correlation of Tg effect size in mouse proteome (x) to transcriptome (y) shown with a least squares
1522 trendline over a scatterplot of the effect sizes for 9319 mouse gene transcripts and corresponding proteins
1523 (Table S8). When more than one splicing isoform protein was present, the one with maximum variance
1524 was retained.

1525 (B) M42 protein (x) to transcriptome (y) effect size scatterplot with least squares trendline, Pearson
1526 correlation (rho), and Student's significance of correlation are shown for Tg vs non-Tg effect sizes (*left*),
1527 and in human AD vs. Control effect sizes (*right*).

1528 (C) M1 RNA-protein correspondence for Tg effect (*left*) and for the effect in human of AD vs. control (*right)*.

1529 (D) M21 RNA-protein correspondence for Tg effect (*left*) and for the human AD effect (*right*).

1530

1531 **Figure S5. Protein-RNA effect size correlation varies in mouse and human for all 44 consensus brain**
1532 **modules.**

1533 Gene product names label each point, with the module number (size rank), count of proteins mapped to
1534 mouse (*left*) from human (*right*), Pearson correlation rho and Student's significance of correlation given
1535 in each plot title.

1536

1537 **Figure S6. Mdk and Ptn colocalization with amyloid is age dependent, occurs in various AD transgenic**
1538 **mouse models, and accumulation does not alter overall solubility.**

1539 (A) Paraffin slides containing brain tissue from 12M non-Tg mice; 3, 6 and 12M CRND8 mice; 12M

1540 Tet.HuAPP, PrP.MoAβ and PrPHuAβ/PS1 mice were stained with mouse anti-pan-Aβ, sheep anti-Mdk or
1541 rabbit anti-Ptn antibodies. scale 50 mm.
1542 (B). Western blots detecting Mdk and Ptn in the urea extracts of 15M CRND8 mice and non-Tg control
1543 brains as shown by SDS-PAGE stained with anti-Mdk or anti-Ptn antibodies in total Urea extracts (first two
1544 lanes for each are male and second two lanes are females. Blots are representatives of three independent
1545 experiments.
1546 (C) Sequential extractions with TBS, RIPA, 2% SDS and 8M Urea, show that neither Mdk nor Ptn become
1547 detergent insoluble. Blots are representatives of three independent experiments.
1548
1549 **Figure S7. Non-Tg staining, fixation effects, co-localization, and astrocyte staining.**
1550 (A) DEP staining of 15-18M old non-Tg controls. Paraffin slides containing brain tissue from 15-18M non-
1551 Tg fixed in 4% paraformaldehyde (one hemibrain) or 10% ethanol (second hemibrain), were stained with
1552 anti-DEP antibodies. Low magnification (scale 500 μm) images were taken from cortex and hippocampus.
1553 (B) Fixation impacts localization, but impacts are dependent on the antiserum used. Paraffin slides
1554 containing brain tissue from 15M CRND8 mice, fixed in 4% paraformaldehyde (one hemibrain) or 10%
1555 ethanol (second hemibrain), were stained with the indicated anti-DEP antibodies. Scale 200 μm.
1556 (C, D) Colocalization of DEP in plaques. Paraffin slides containing brain tissue from 15M TgCRND8 mice,
1557 were stained with either mouse anti-pan-Aβ antibody or Thio-S and rabbit anti-DEP. Secondary
1558 fluorescent anti-mouse (green) and rabbit (red) antibodies were used. Colocalization was visualized by
1559 overlap of green and red colors to create yellow in plaques (C) or CAA (D) Scale 50 μm.
1560 (E) Select DEPs accumulate in astrocytes surrounding amyloid plaques. Paraffin slides containing brain
1561 tissue from 15-18M CRND8 mice were stained with anti-DEP antibodies. Scale 200 μm.
1562
1563 **Figure S8. Antibody validation studies and additional DEPS validated by Western blotting.**
1564 (A) Antibody validation. 293T HEK cells were transfected with plasmids containing FLAG-tagged cDNAs
1565 encoding M42+ DEP and gene expression in the media (SPOCK3, VTN, HTRA1) and lysates (all other genes)
1566 was detected on SDS-PAGE with 1 (anti-Flag) and 2 (anti-DEP sera). Non-transfected cells served as
1567 control. Representative blots of at least three independent experiments are shown. Sources of the
1568 antibodies are listed in Table S10, S11.
1569 **(**B) M42+ DEPs are detected in total UREA extracts from 15M CRND8 mice. Brain homogenates from Tg
1570 and age matched non-Tg mice were subjected to SDS-PAGE and stained with anti-DEP antibodies. (n=2;
1571 one male and one female).
1572
1573 **Figure S9. Midkine and Pleiotrophin overexpression increase formation of Aβ amyloid deposition and**
1574 **CAA in 3M CRND8 mice and 6M mouse data on gliosis.**
1575 Mice were intracerebrally injected with rAAV2/8-Mdk, rAAV2/8-PTN or not-injected (control) at P0 and
1576 aged 3 months.
1577 (A, B) Representative images of cortex and hippocampus (A) or CAA (B) stained with biotinylated anti-Aβ
1578 mAb 33.1.1 (anti-Aβ 1-16). Scale bar: 500 μm, 50 μm (inset). Quantification data of the entire brain plaque
1579 count in three non-consecutive sections represented by a scatter dot plot of male (closed circle/square)
1580 and female (open circle/square) ± standard error of the mean. n=5-15. Plaques were quantified with one-
1581 way ANOVA test (*, $p<0.05$; ***, $p<0.001$).
1582 (C) RIPA, 2% SDS and 70% formic acid (FA) extracted Aβ40 and Aβ42 levels were detected by ELISA and
1583 plotted as scatter dot plot of male (closed circle/square) and female (open circle/square) ± standard error
1584 of the mean. n=5-12. Aβ42 and Aβ40 levels were quantified with corresponding one-way ANOVA and
1585 paired comparison test (*, $p<0.05$; **, $p<0.01$, ***, $p<0.001$).

1586 (D, E) Mdk and PTN overexpression induces astrocytosis and microgliosis in 6M CRND8 mice.
1587 Representative images of GFAP-reactive astrocyte (D) and Iba-1 reactive microglia (E) in 6-month-old
1588 TgCRND8 mice overexpressing Mdk or PTN genes. Quantitation of the Iba-1 or GFAP staining was
1589 performed in cortex and hippocampus combined area. N = 6 mice. Scale bar, 500 µm, 50 µm. Clear
1590 symbols denote female mice and filled symbols denote male mice. Data represents mean ± sem. One-way
1591 ANOVA; ***p < 0.001; **p < 0.01; *p < 0.05.
1592
1593 **Figure S10. Mdk and PTN interact with heparin.**
1594 Flag-tagged Mdk and PTN secreted into the media of transiently transfected HEK cells binds to heparin-
1595 agarose beads.
1596
1597 **Figure S11. Human heart tissues stained with Congo red, MDK, PTN and CLU.** Representative images of
1598 immunohistochemical stains for Congo Red, MDK, PTN or CLU on human cardiac amyloidosis sections.
1599 Scale bar, 300 µm.
1600
1601 **Figure S12. Contextualization of CRND8 18M proteome by integration with AD GWAS MAGMA p**
1602 **values and AD CSF proteomic changes.**
1603 (A) Volcano plot of log2 Fc of DEPs in the 18M CRND8 proteome versus the -log10p MAGMA AD GWAS
1604 values (Table S1). Red circles indite GWAS loci that have been prioritized for further study. Blue circles
1605 indicate M42+ DEPs that accumulate in the CRND8 proteome. APOE and CLU are denoted as known
1606 GWAS loci that accumulate with amyloid by circles with red interior with blue border.
1607 (B) Volcano plot of the AD vs control CSF log 2 Fc derived from the Caucasian cohort in Modeste et. al
1608 51, annotated by showing as colored symbols the overlapping DEPS in the CRND8 18M brain proteome.
1609 Red indicates a change that is concordant in direction between CSF and mouse brain. Yellow indicates a
1610 discordant change. M42 members are denoted by red squares. Grey triangles indicate significantly
1611 altered proteins in CSF that are either not detected in the 18M CRND8 proteome or not significantly
1612 changed (see Table S13).
1613
1614 **Figure S13. A schematic illustrating the amyloid scaffold hypothesis.**
1615
1616 **Supplemental Tables.**
1617 Table S1. Master stats table for all 3 age group batches, including MAGMA p values from AD GWAS and
1618 human brain data from Johnson et al [9].
1619 Table S2. Unified 3 TMT batch traits
1620 Table S3. TMT Normalized abundance
1621 Table S4. TMT Normalized abundance 5% < FDR < 5%, Granular quantifications
1622 Table S5. CRND8 3 age group batch statistics for proteins from table.
1623 Table S6. Genes and mRNA expression (log2 Fc) from reprocessed AD TCx and 20M CRND8 mice used for
1624 Figure S1A.
1625 Table S7. List of DEPS used in GO analysis in Figure 1.
1626 Table S8. RNA-Seq Counts, Dispersion-normalized, with Statistics for 18M CRND8 vs 18M Non-Tg
1627 Table S9. Histopathology results summary CRND8 studies.
1628 Table S10. Antibodies used in mice and staining conditions.

1629 Table S11. Antibodies used in humans and staining conditions.

1630 Table S12. List of peptides used to create new antibodies and list of antibodies/antisera that were tested
1631 from commercial sources that did not work on the pathological specimens.

1632 Table S13. List of CSF proteins and DEPs in 18M CRND8 brains used for Figure S12.

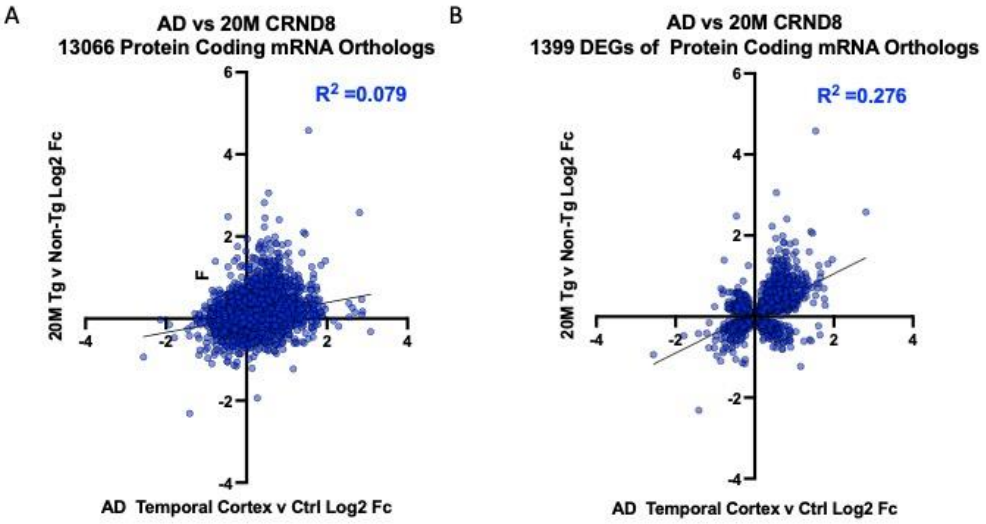

Figure S1. Correlation of protein encoding mRNAs in 20M CRND8 mice (Tg versus non-Tg) and AD versus Control human Temporal Cortex.

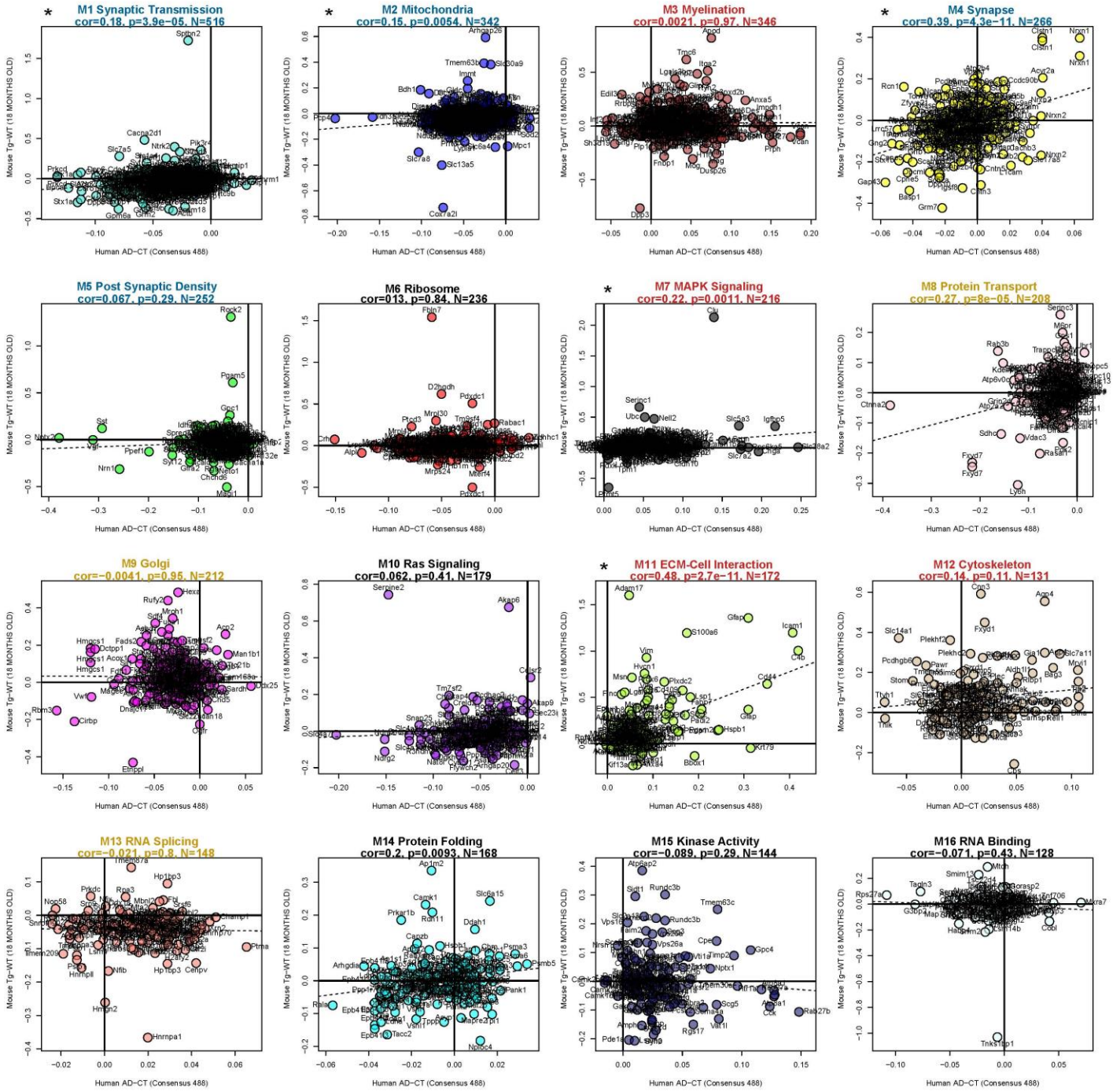

Figure S2. Effect size correlation for human AD vs control effect and mouse Tg effect at 18M shows varying concordance in each of the 44 consensus brain modules.

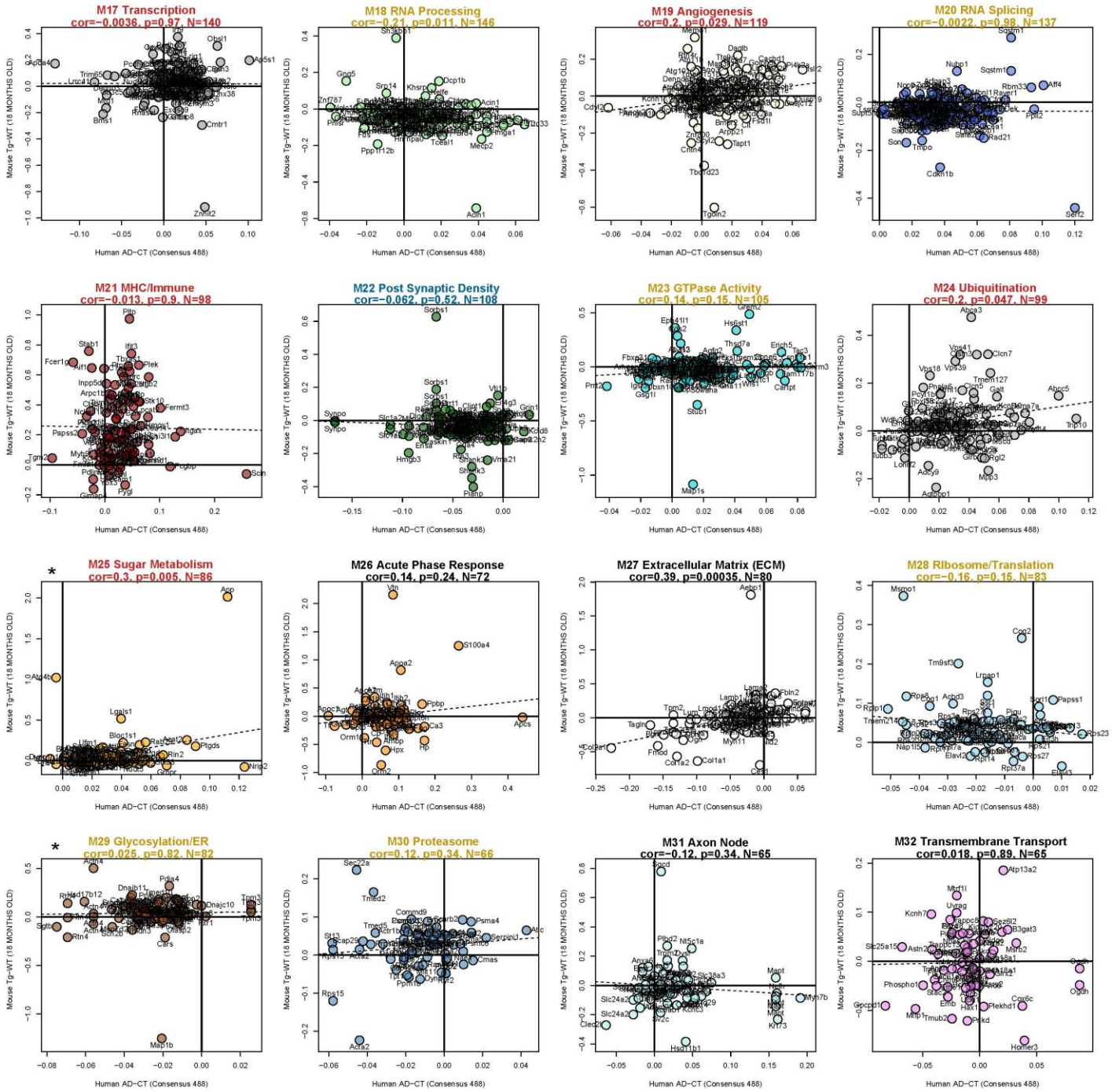

Figure S2 (cont.). Effect size correlation for human AD vs control effect and mouse Tg effect at 18M shows varying concordance in each of the 44 consensus brain modules.

1

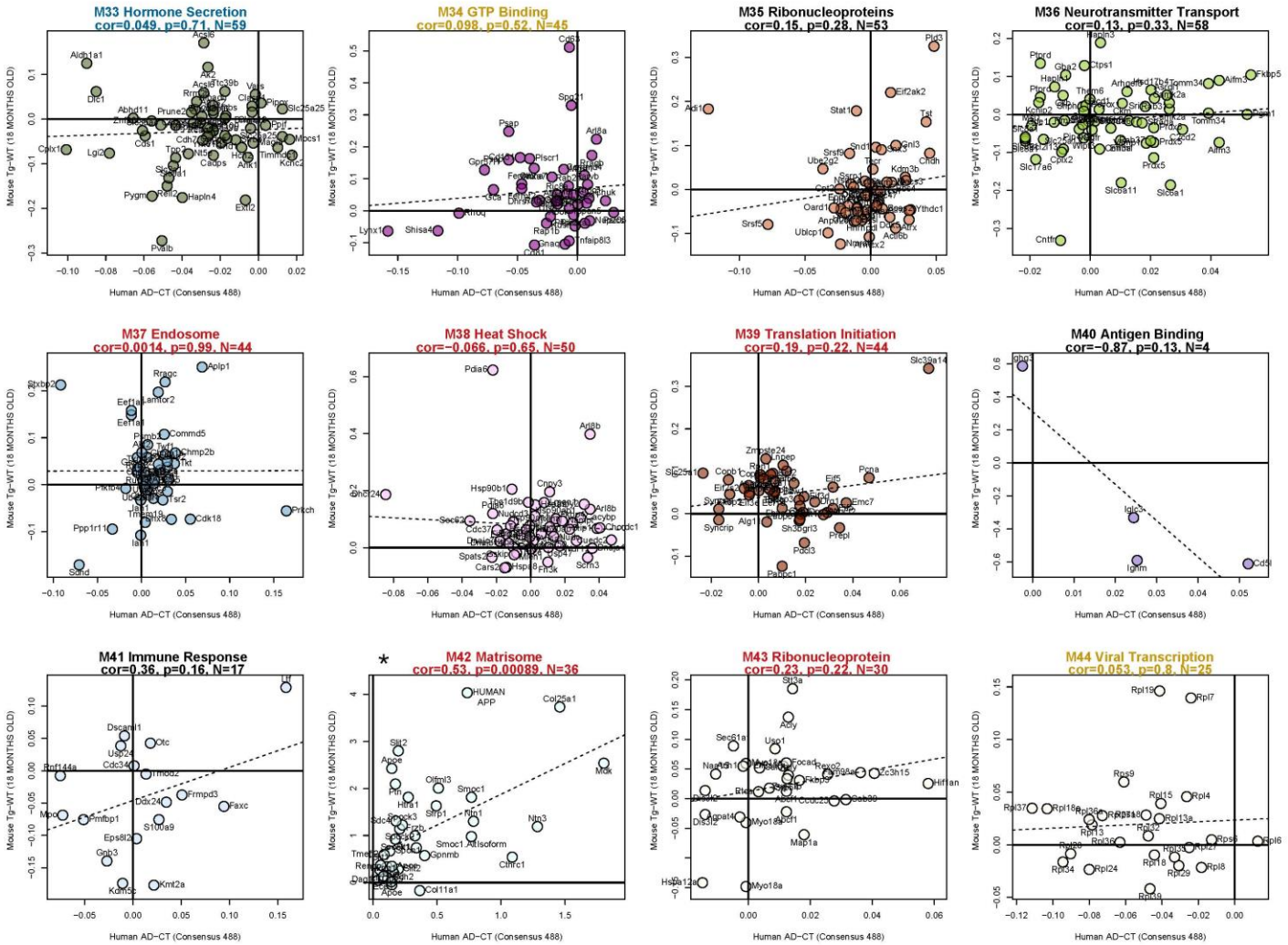

Figure S2 (cont.). Effect size correlation for human AD vs control effect and mouse Tg effect at 18M shows varying concordance in each of the 44 consensus brain modules.

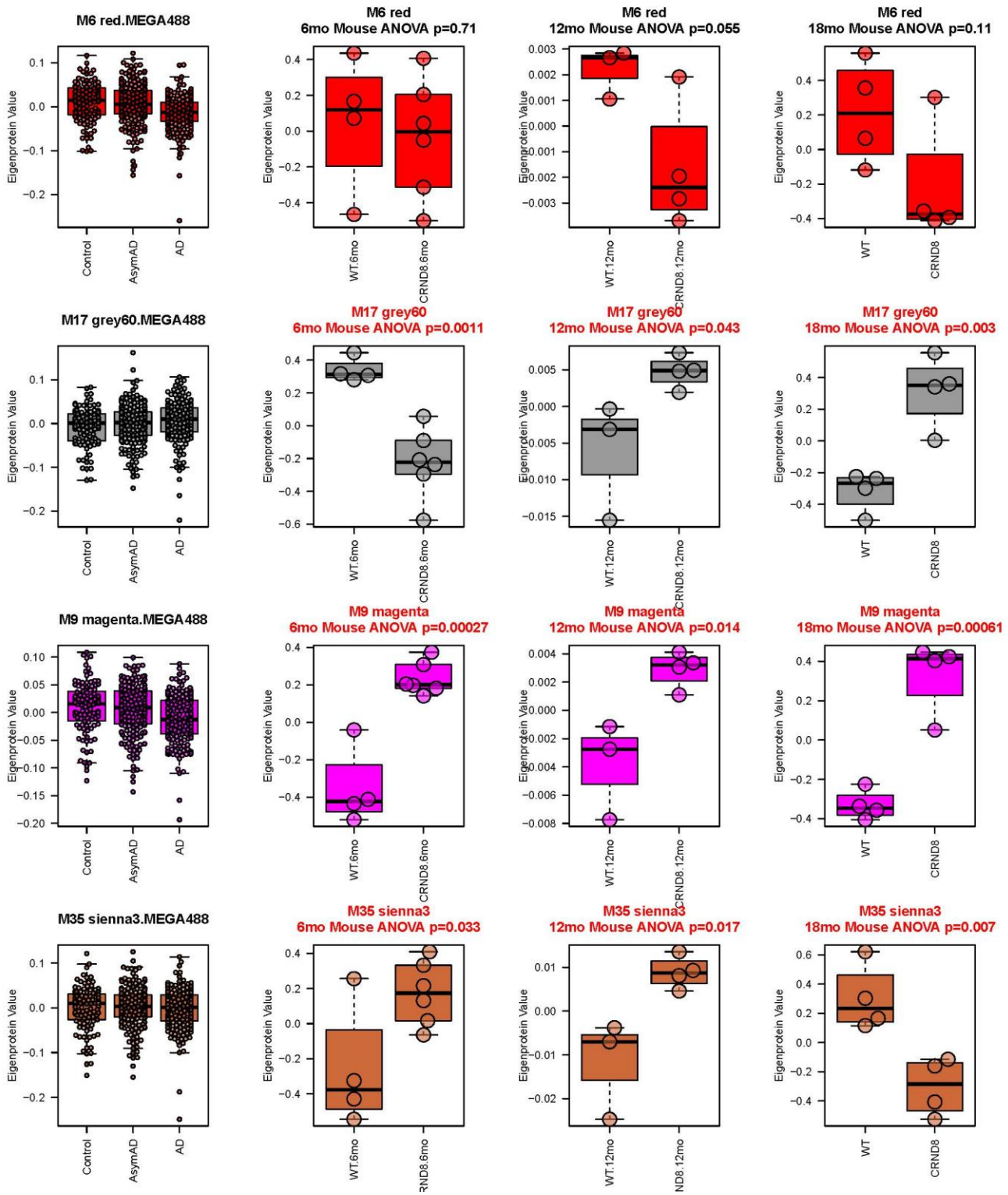

Figure S3. Synthetic eigenproteins (modules) show trends across the three cohorts of aged Tg and non-Tg mice for all 44 consensus brain modules.

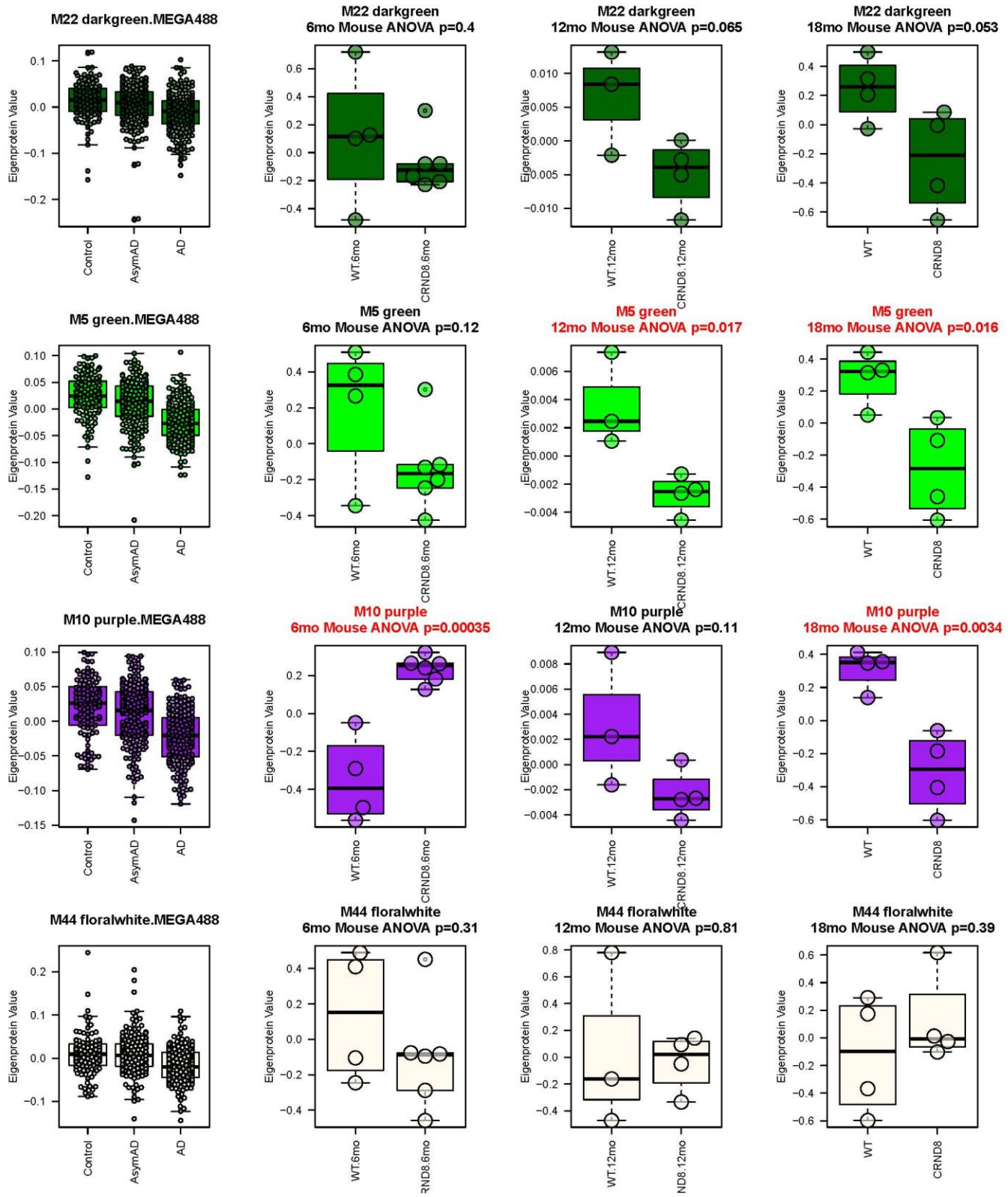

Figure S3 (cont.). Synthetic eigenproteins (modules) show trends across the three cohorts of aged Tg and non-Tg mice for all 44 consensus brain modules.

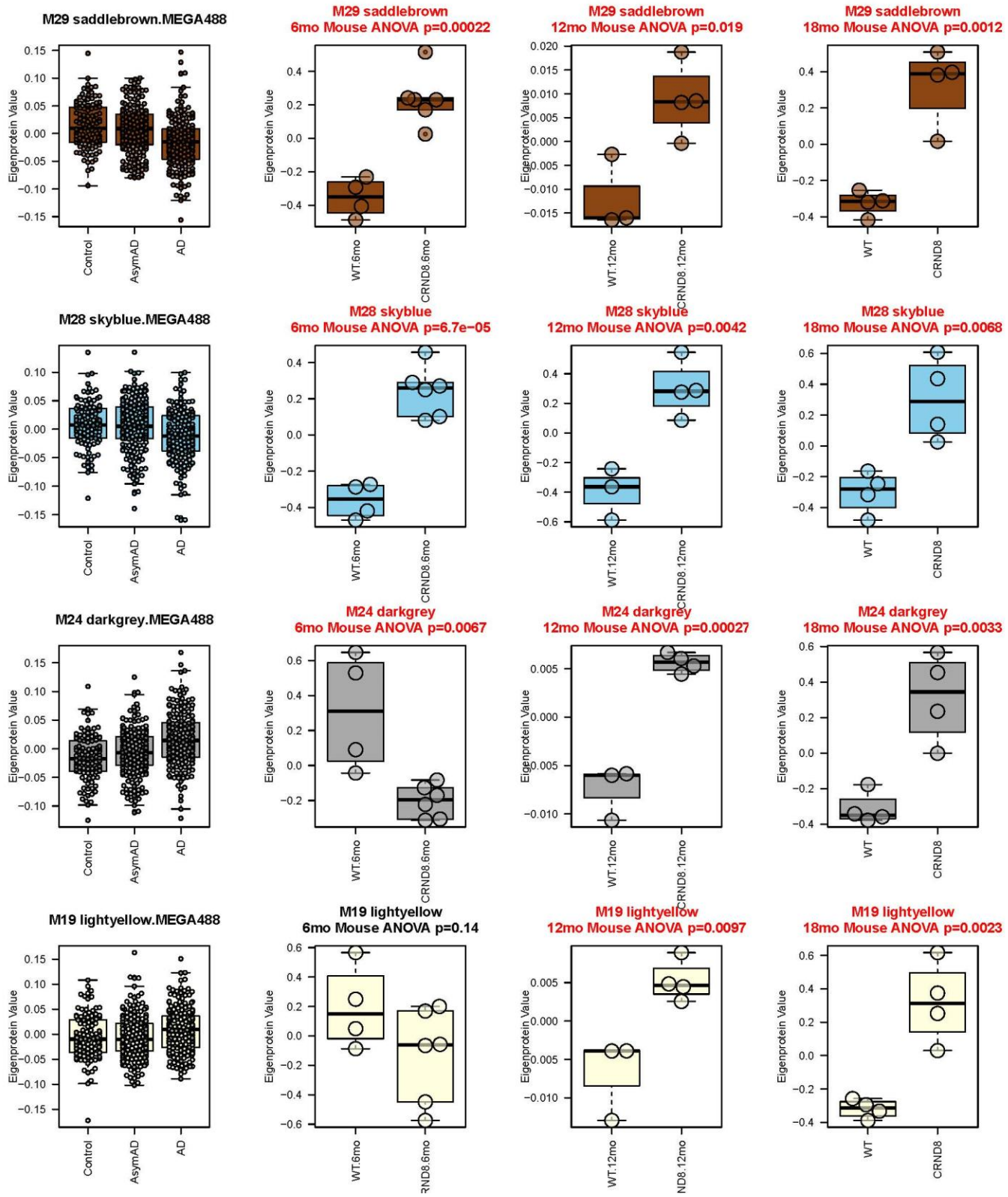

Figure S3 (cont.). Synthetic eigenproteins (modules) show trends across the three cohorts of aged Tg and non-Tg mice for all 44 consensus brain modules.

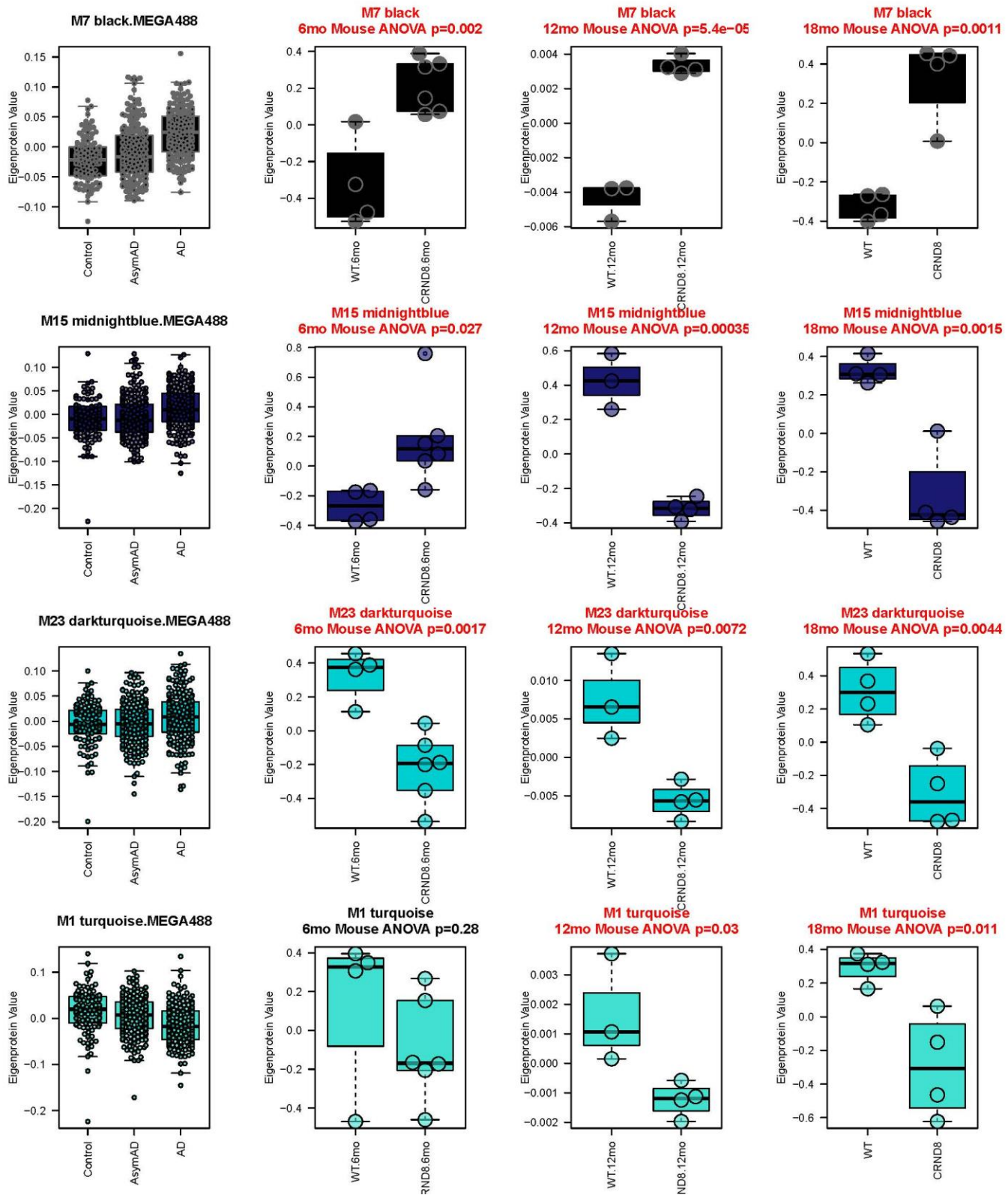

Figure S3 (cont.). Synthetic eigenproteins (modules) show trends across the three cohorts of aged Tg and non-Tg mice for all 44 consensus brain modules.

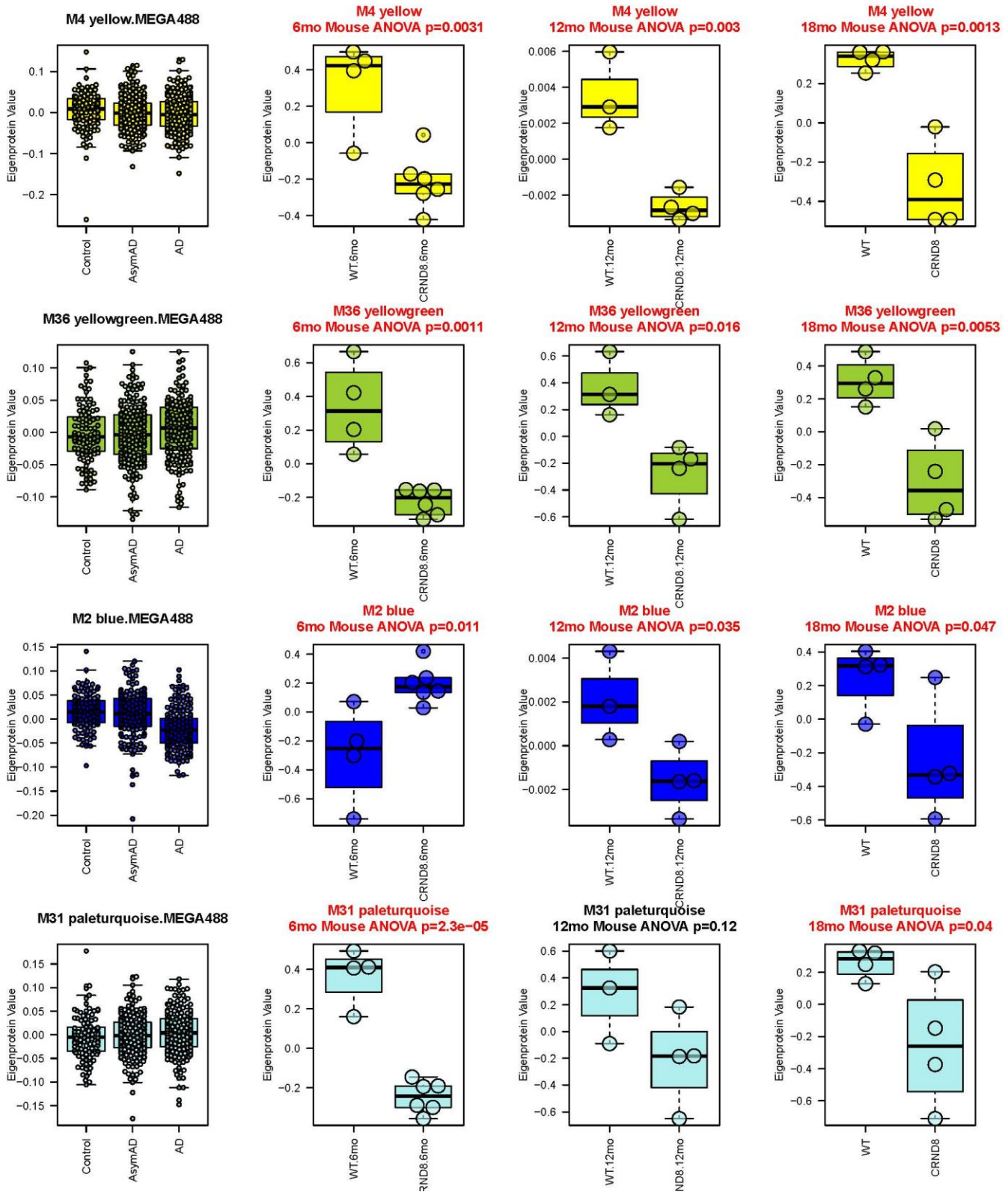

Figure S3 (cont.). Synthetic eigenproteins (modules) show trends across the three cohorts of aged Tg and non-Tg mice for all 44 consensus brain modules.

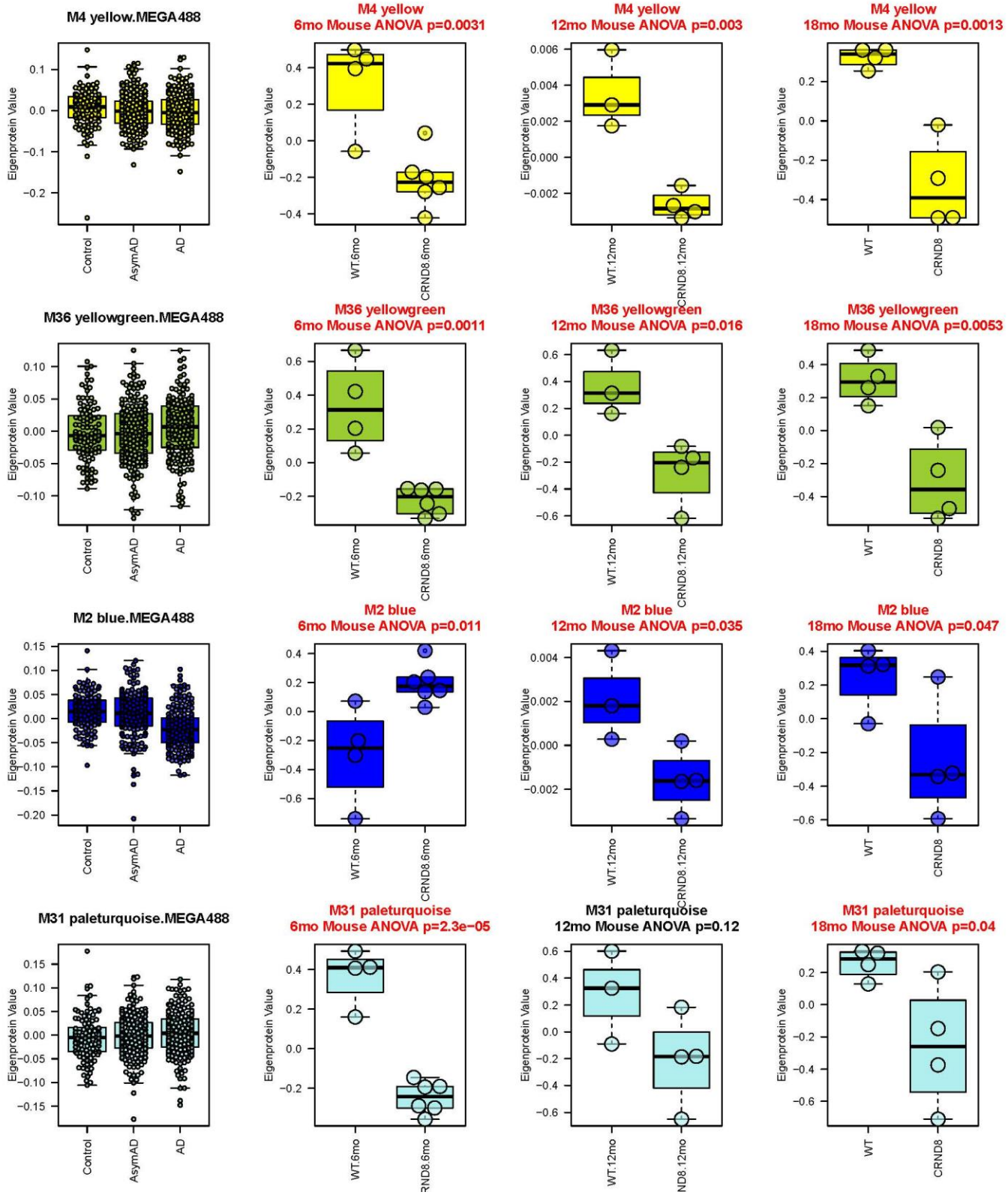

Figure S3 (cont.). Synthetic eigenproteins (modules) show trends across the three cohorts of aged Tg and non-Tg mice for all 44 consensus brain modules.

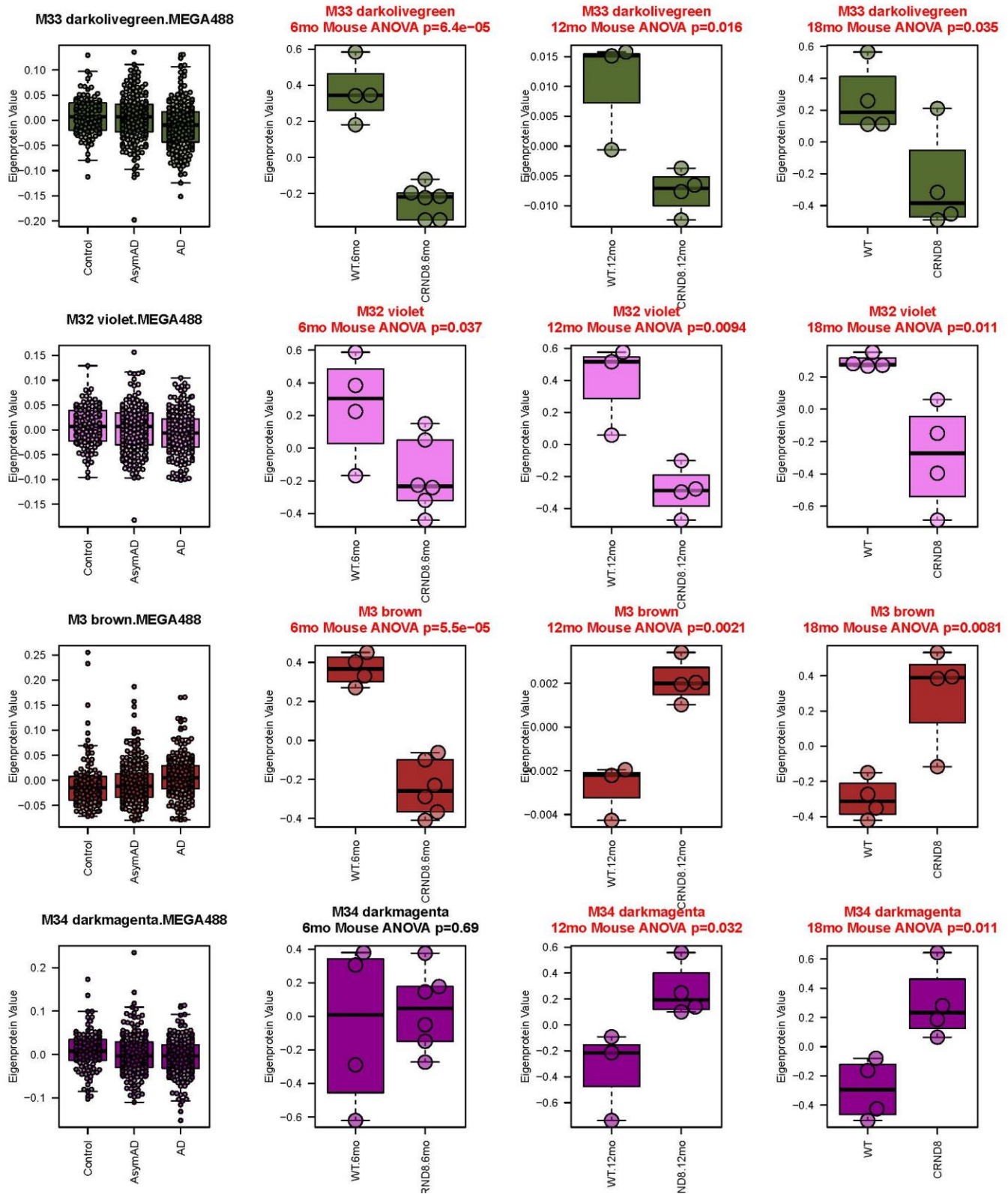

Figure S3 (cont.). Synthetic eigenproteins (modules) show trends across the three cohorts of aged Tg and non-Tg mice for all 44 consensus brain modules.

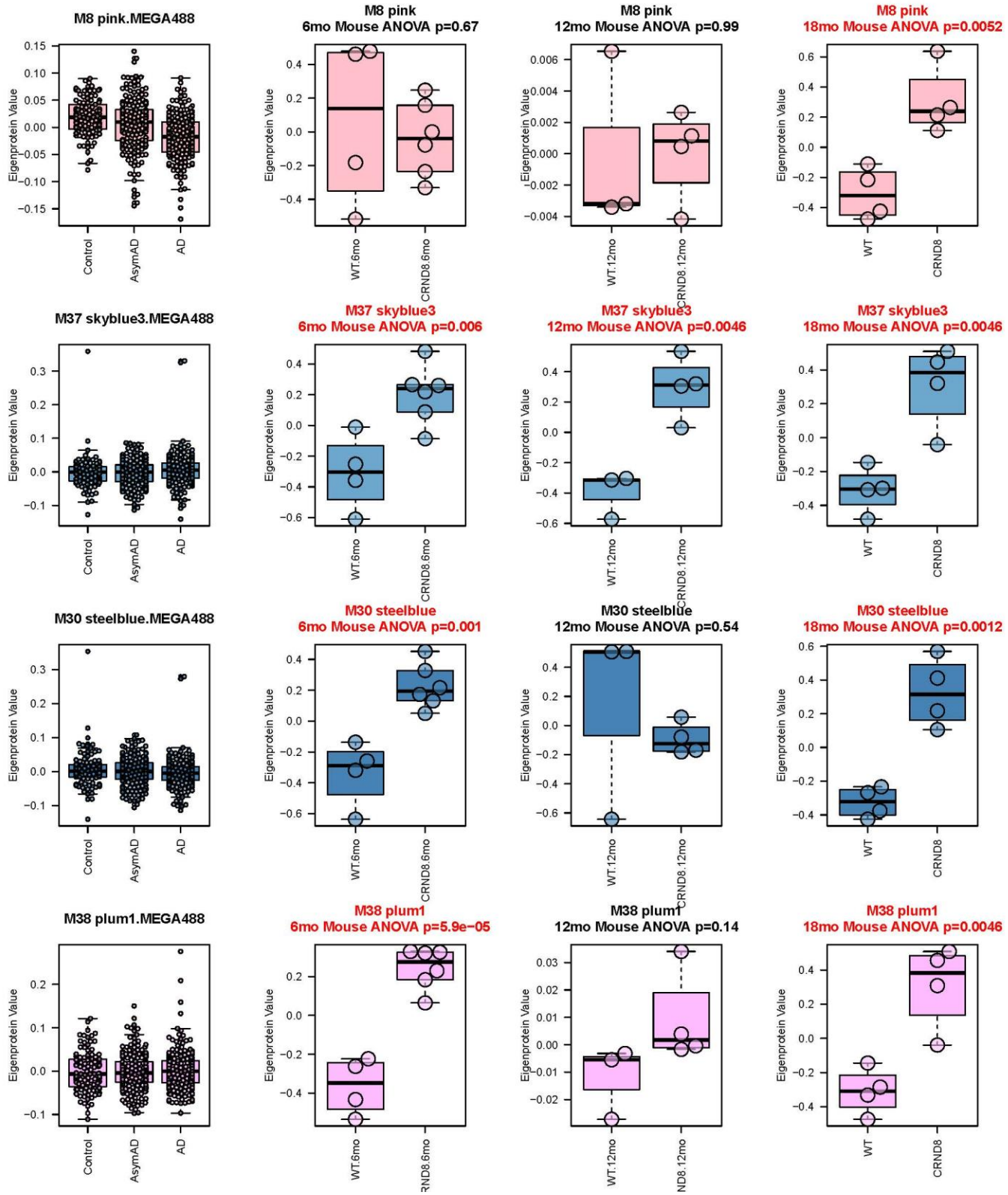

Figure S3 (cont.). Synthetic eigenproteins (modules) show trends across the three cohorts of aged Tg and non-Tg mice for all 44 consensus brain modules.

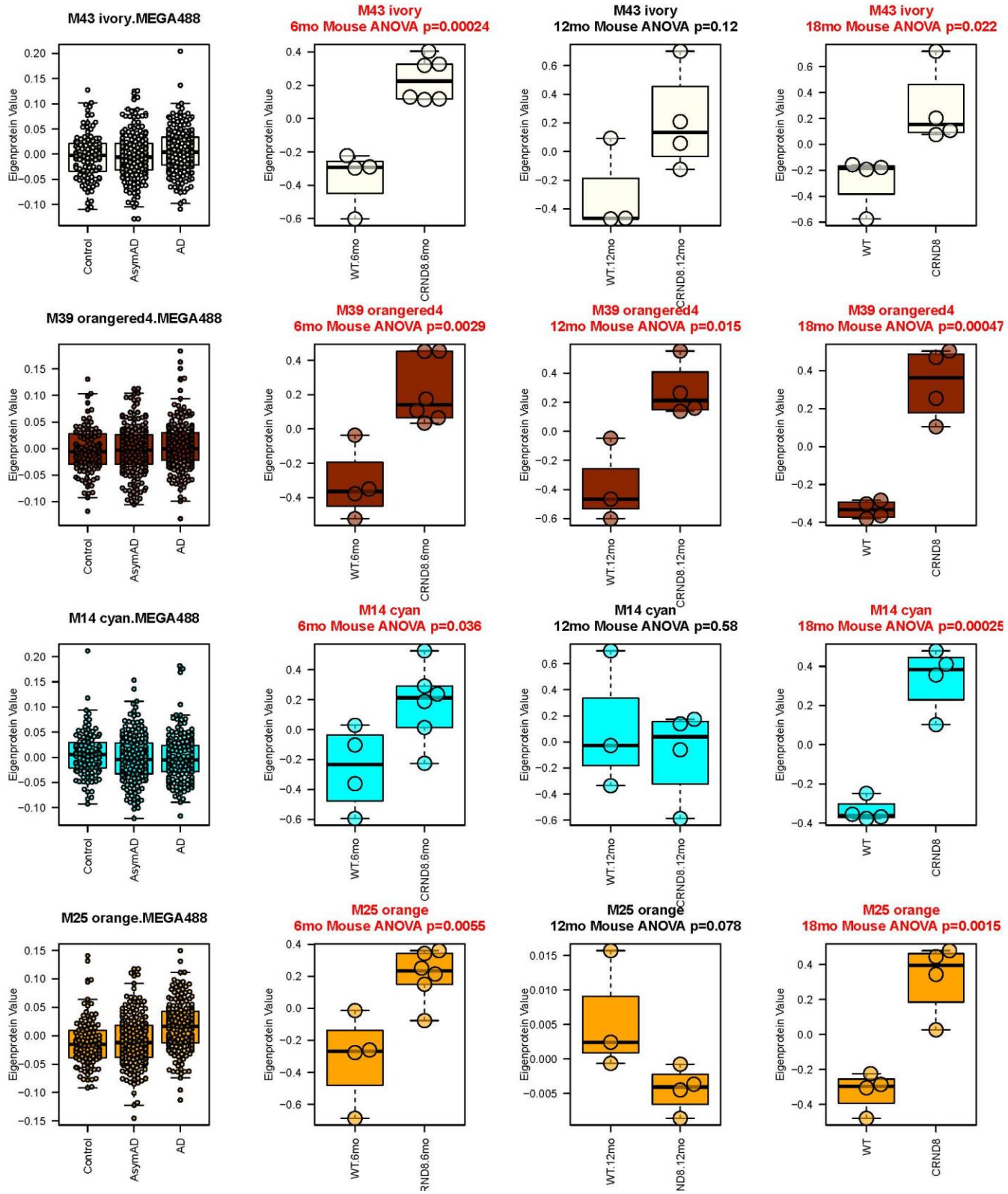

Figure S3 (cont.). Synthetic eigenproteins (modules) show trends across the three cohorts of aged Tg and non-Tg mice for all 44 consensus brain modules.

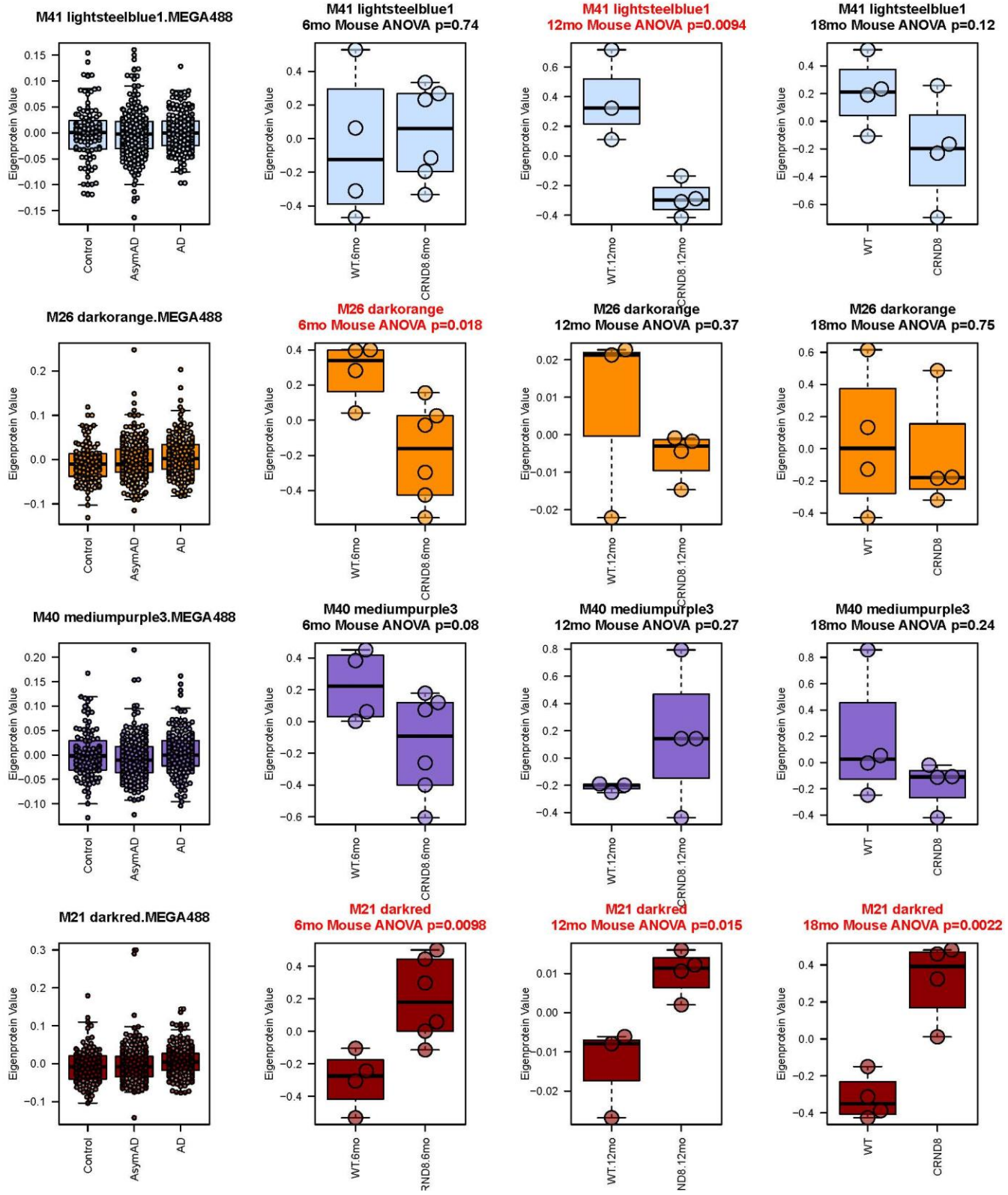

Figure S3 (cont.). Synthetic eigenproteins (modules) show trends across the three cohorts of aged Tg and non-Tg mice for all 44 consensus brain modules.

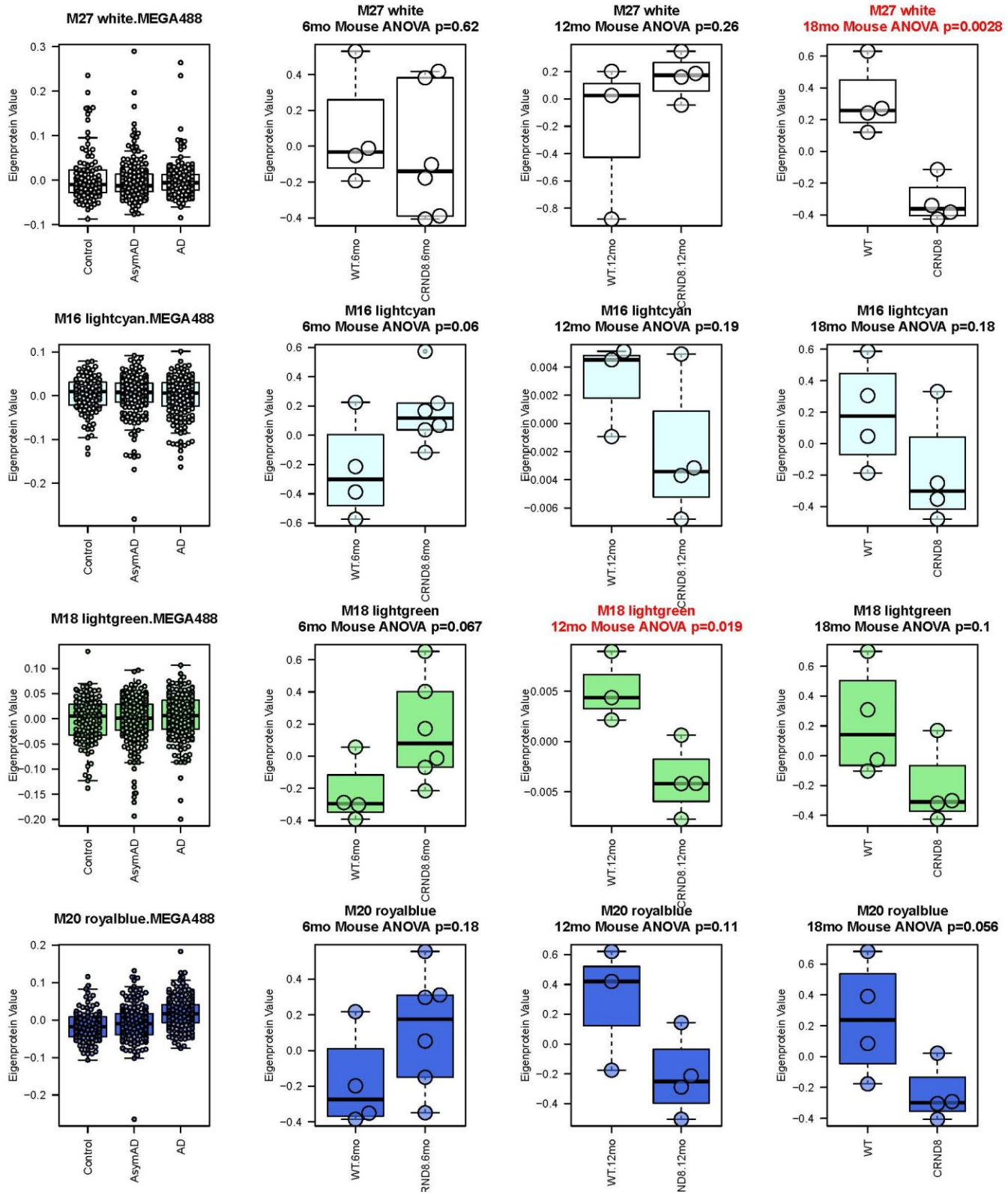

Figure S3 (cont.). Synthetic eigenproteins (modules) show trends across the three cohorts of aged Tg and non-Tg mice for all 44 consensus brain modules.

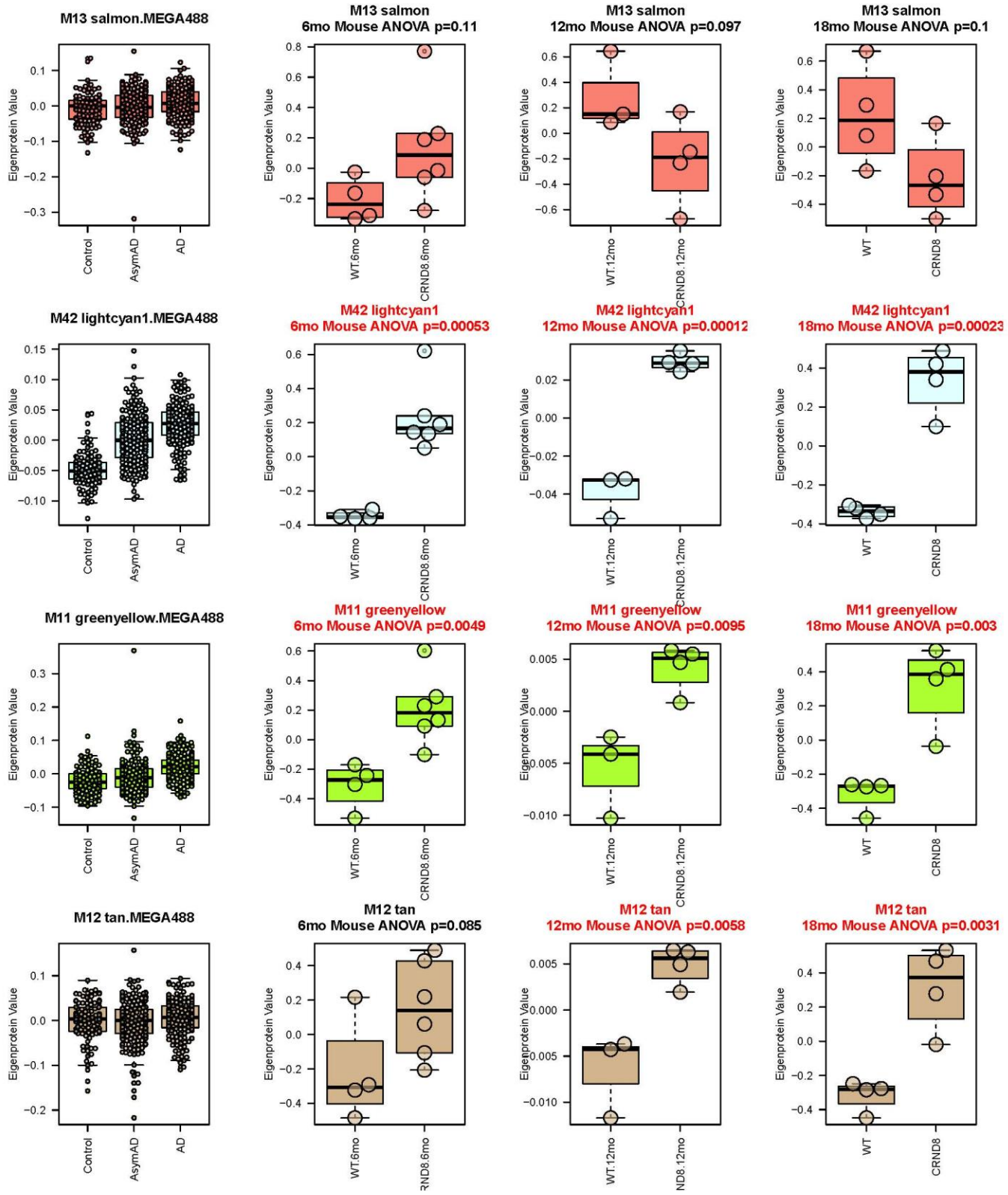

Figure S3 (cont.). Synthetic eigenproteins (modules) show trends across the three cohorts of aged Tg and non-Tg mice for all 44 consensus brain modules.

Figure 4

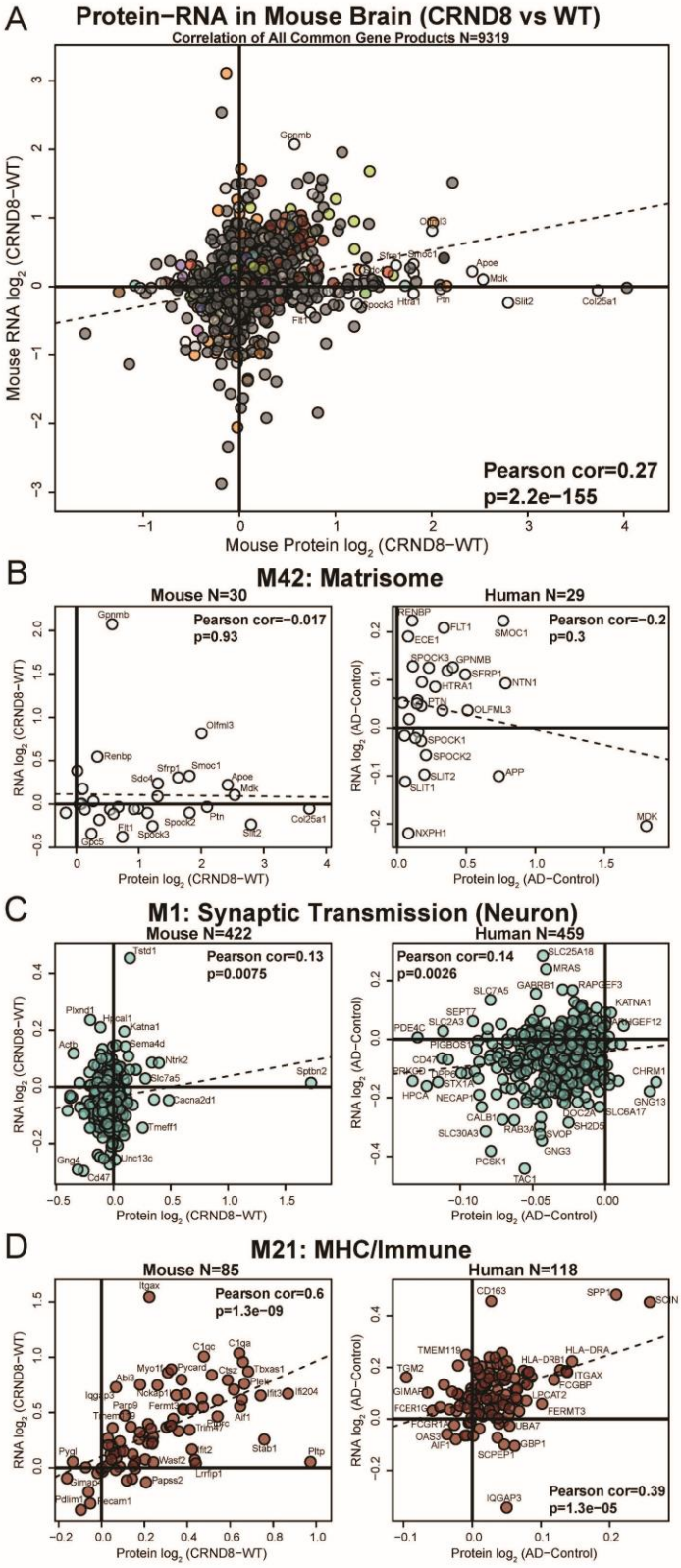

Figure S4. RNA-Protein AD or Tg Effect Size Correlation, in total and within modules.

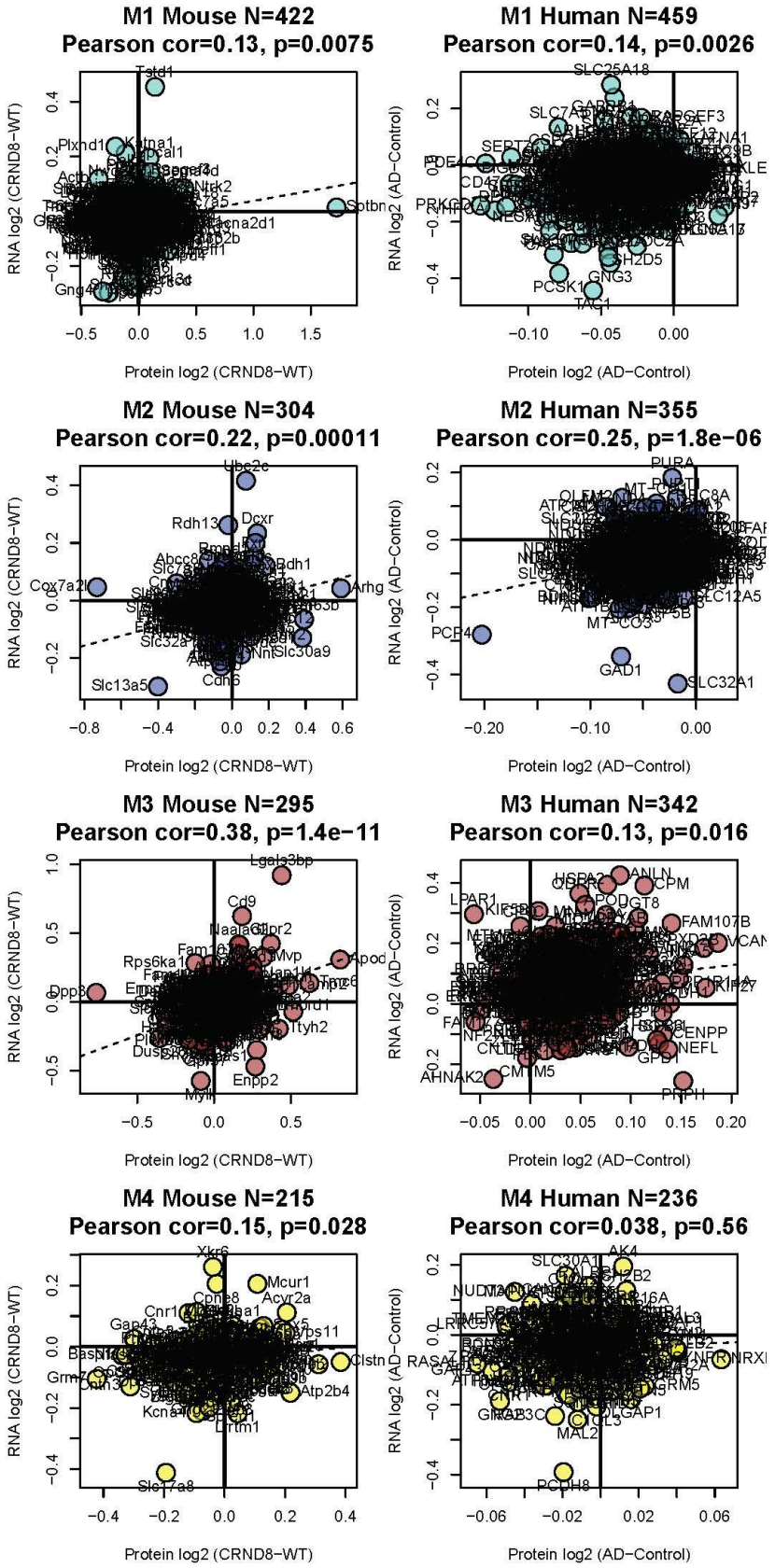

Figure S5. Protein-RNA effect size correlation varies in mouse and human for all 44 consensus brain modules.

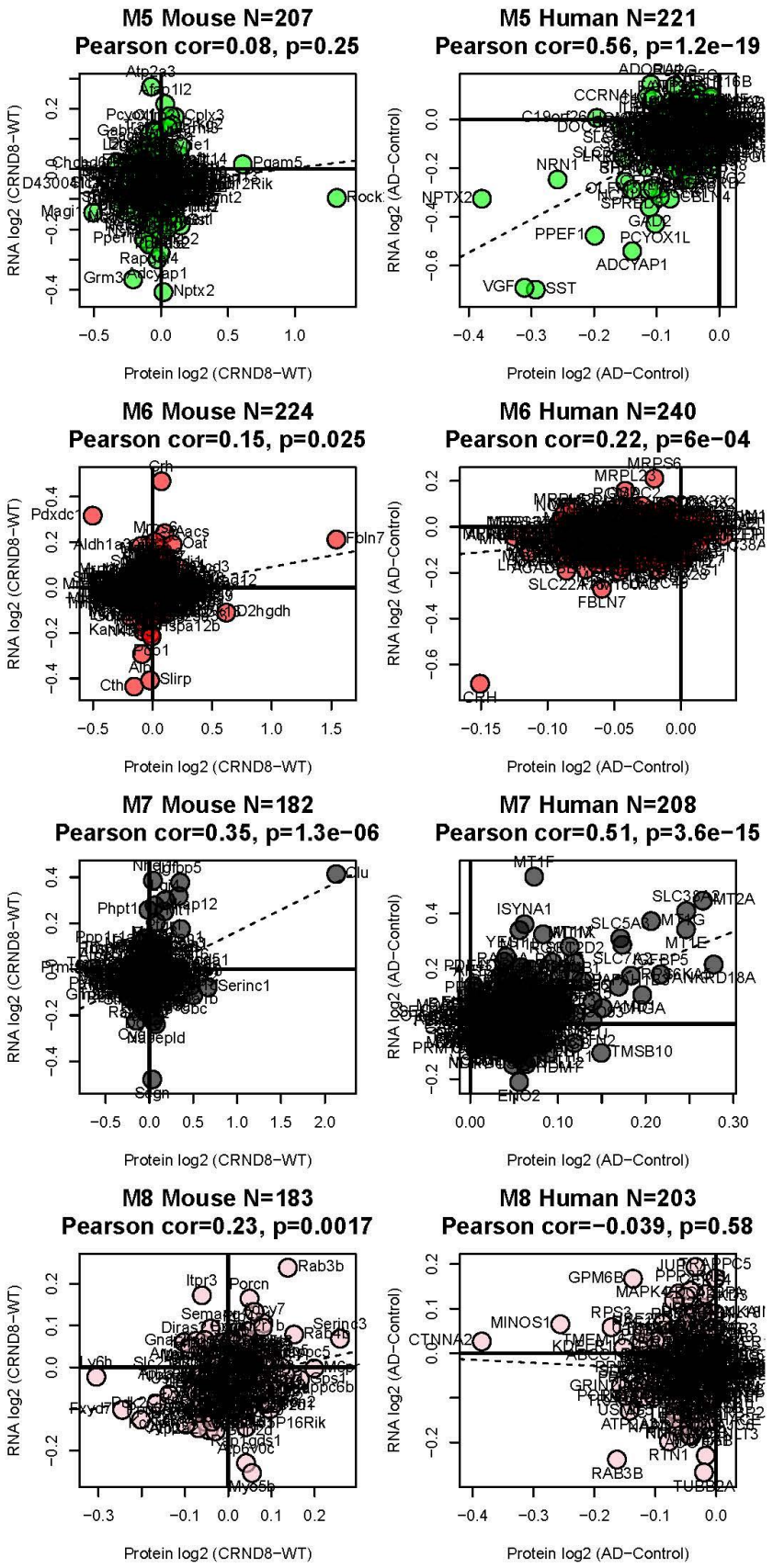

Figure S5 (cont.). Protein-RNA effect size correlation varies in mouse and human for all 44 consensus brain modules.

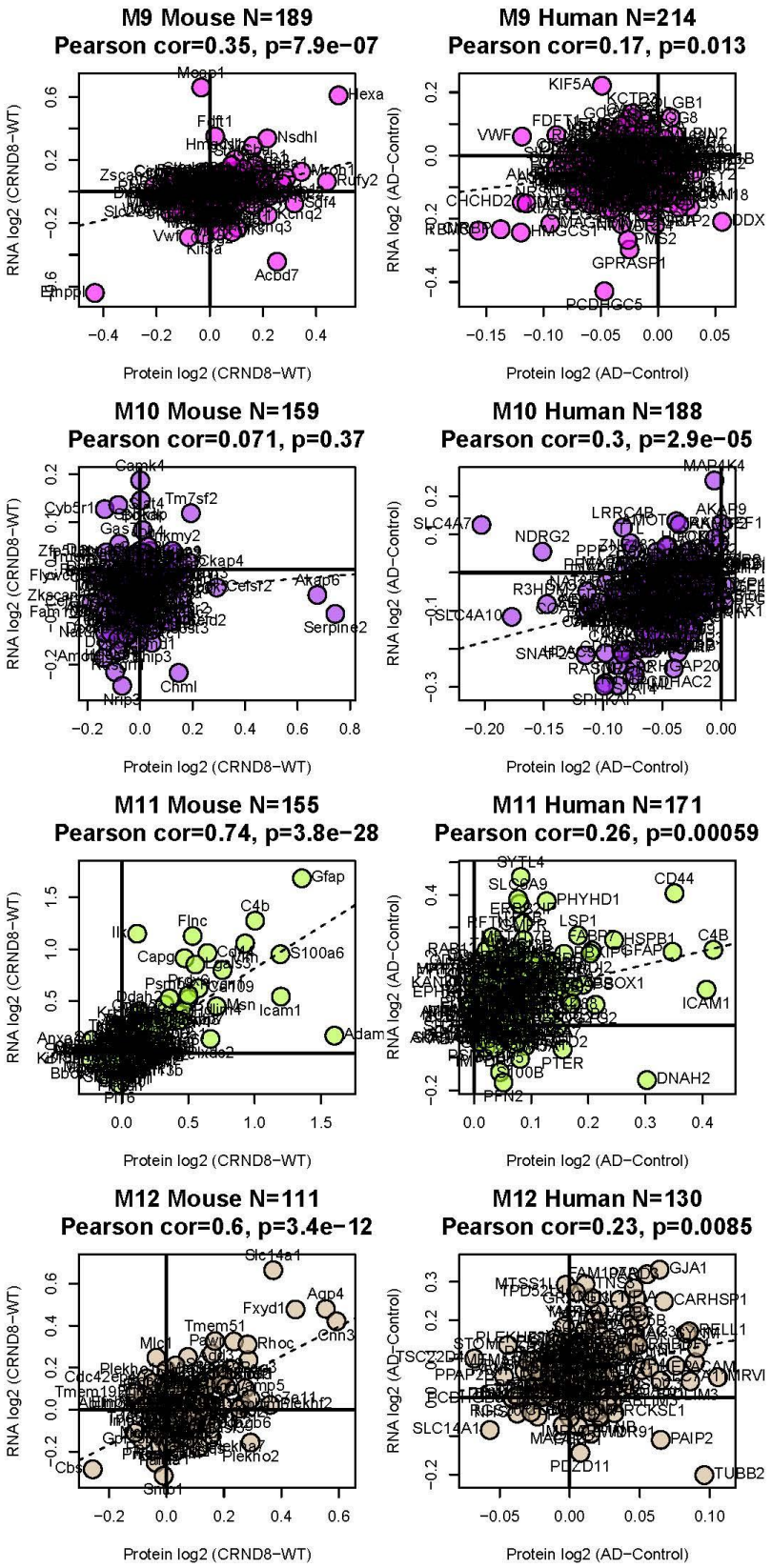

Figure S5 (cont.). Protein-RNA effect size correlation varies in mouse and human for all 44 consensus brain modules.

1653

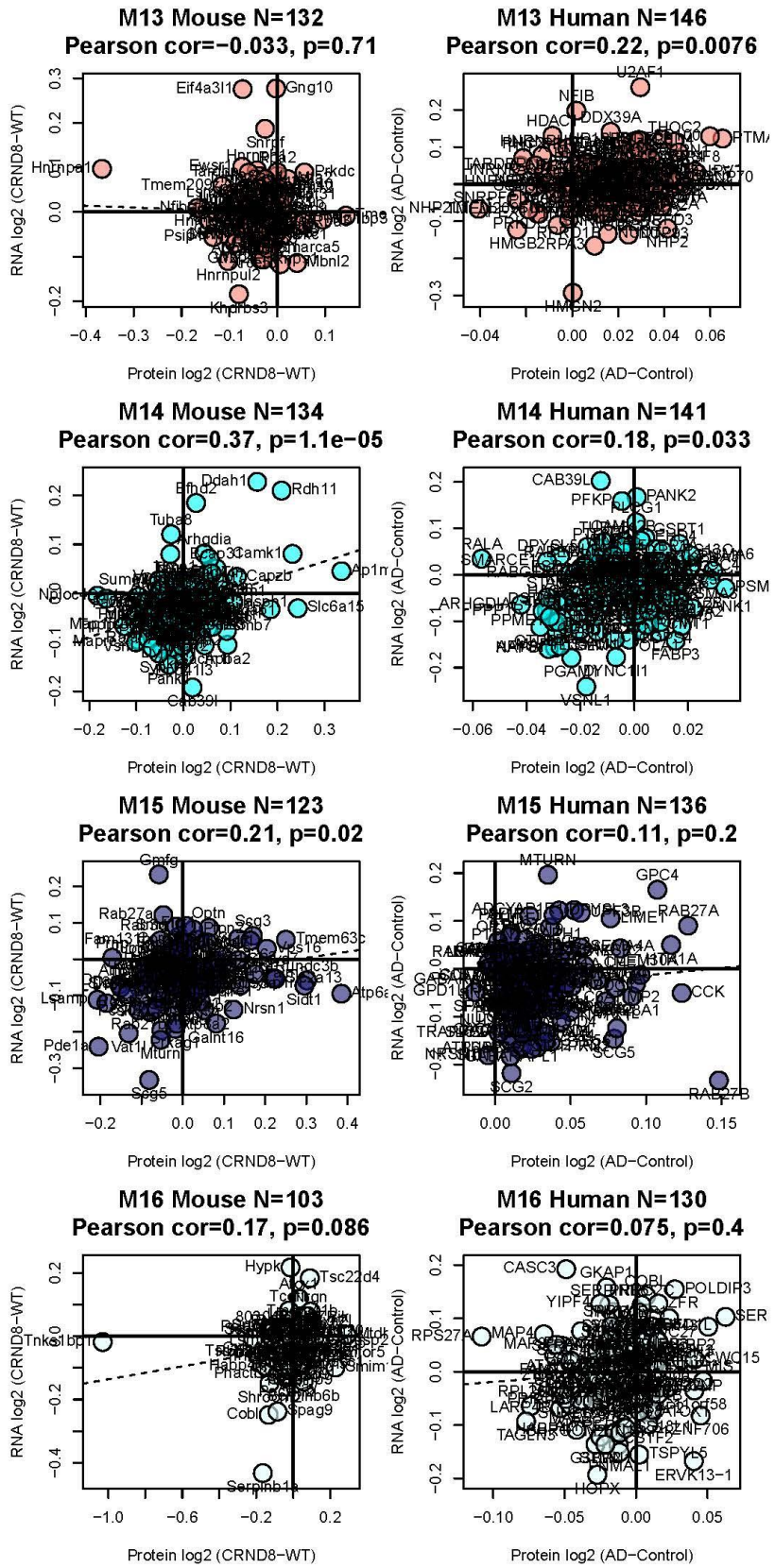

Figure S5 (cont.). Protein-RNA effect size correlation varies in mouse and human for all 44 consensus brain modules.

1654

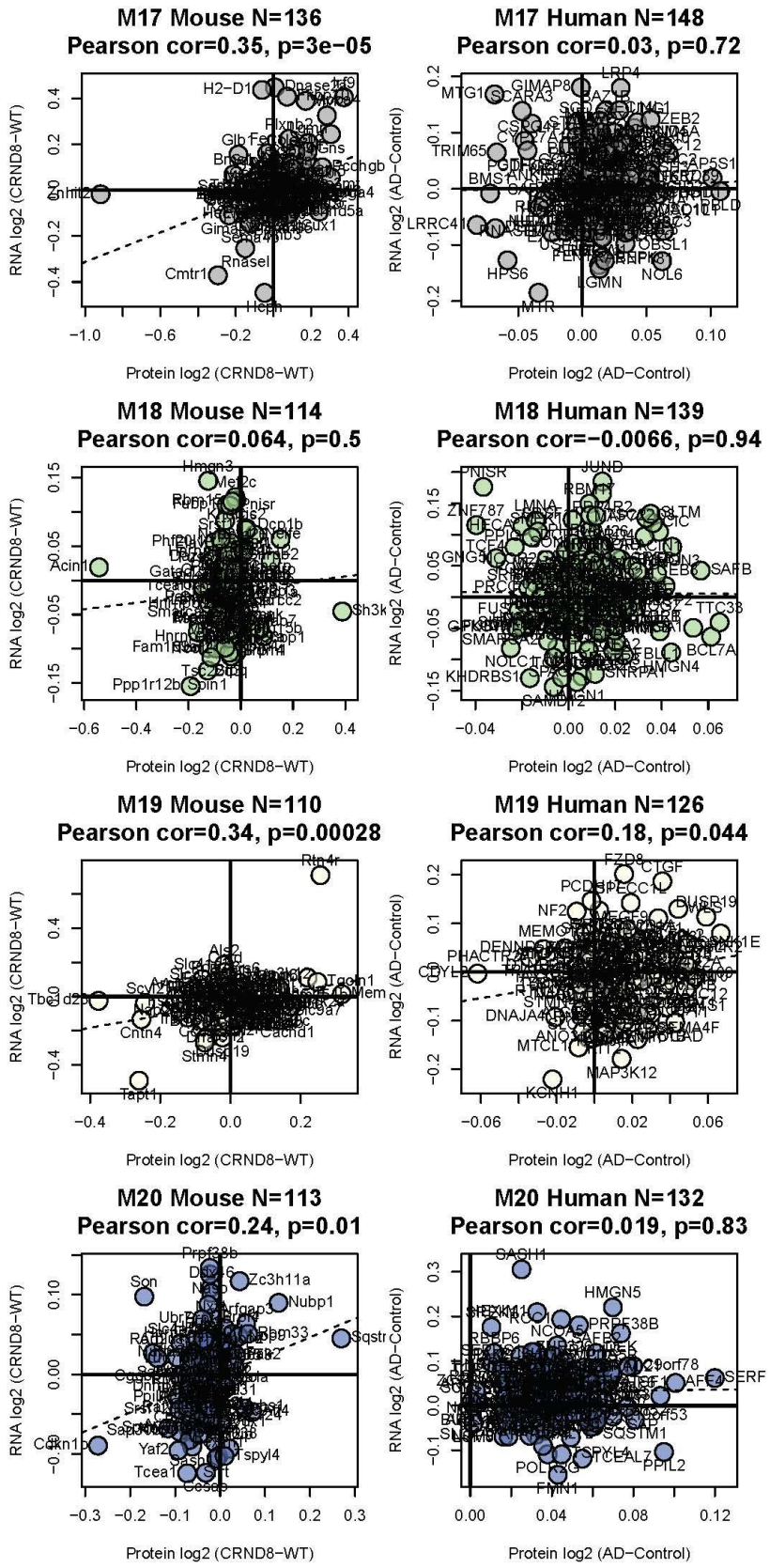

Figure S5 (cont.). Protein-RNA effect size correlation varies in mouse and human for all 44 consensus brain modules.

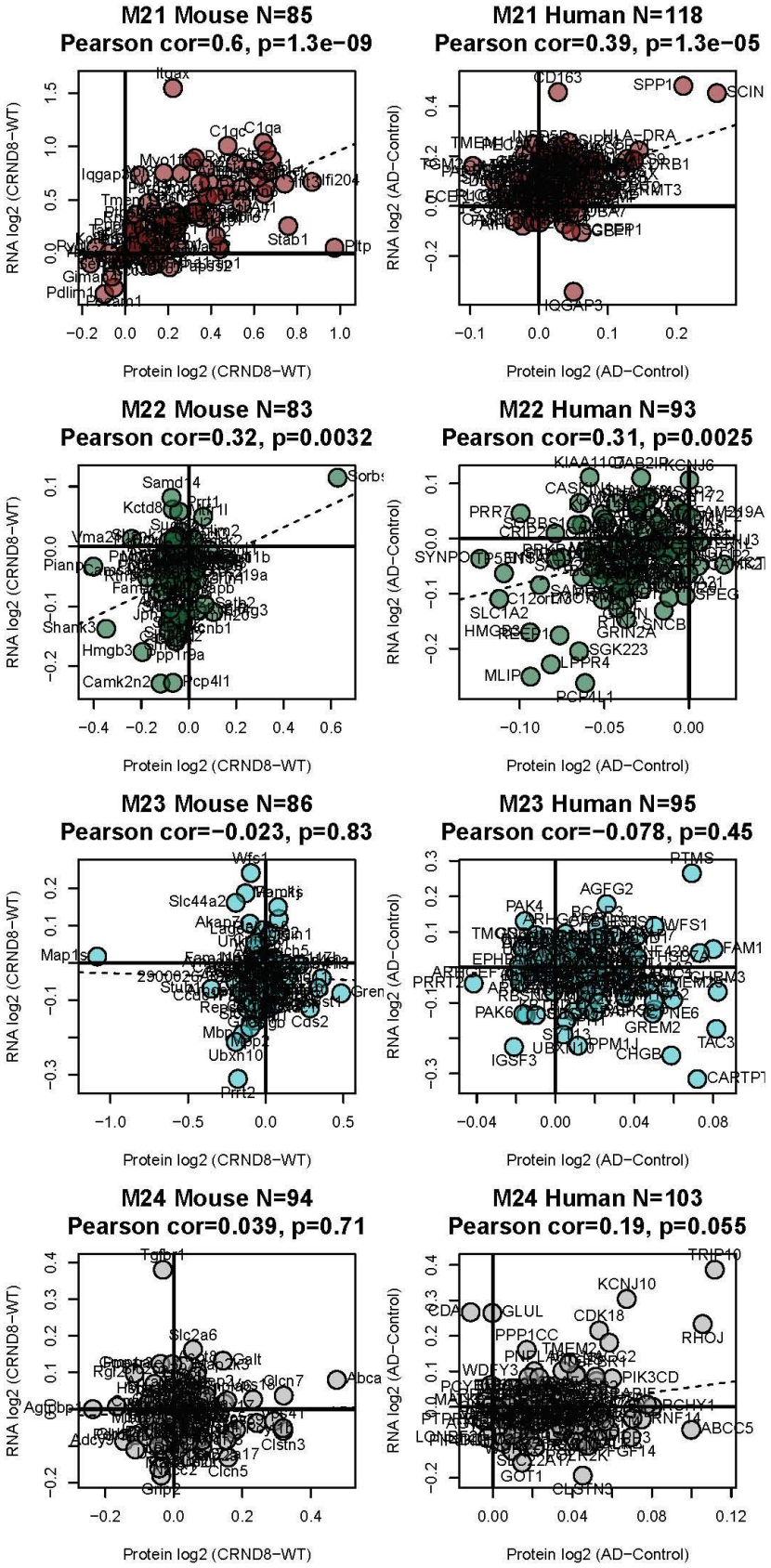

Figure S5 (cont.). Protein-RNA effect size correlation varies in mouse and human for all 44 consensus brain modules.

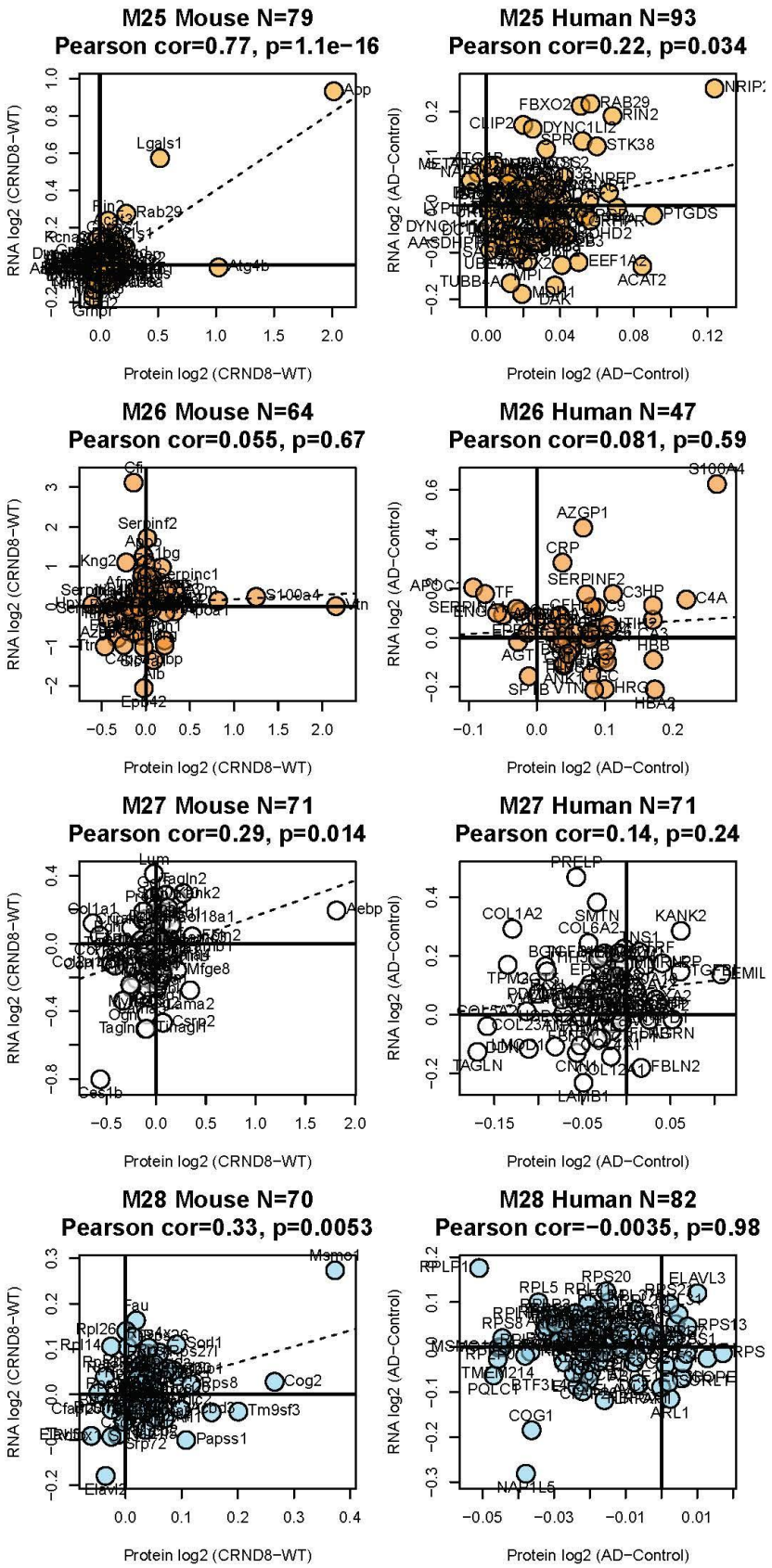

Figure S5 (cont.). Protein-RNA effect size correlation varies in mouse and human for all 44 consensus brain modules.

1657

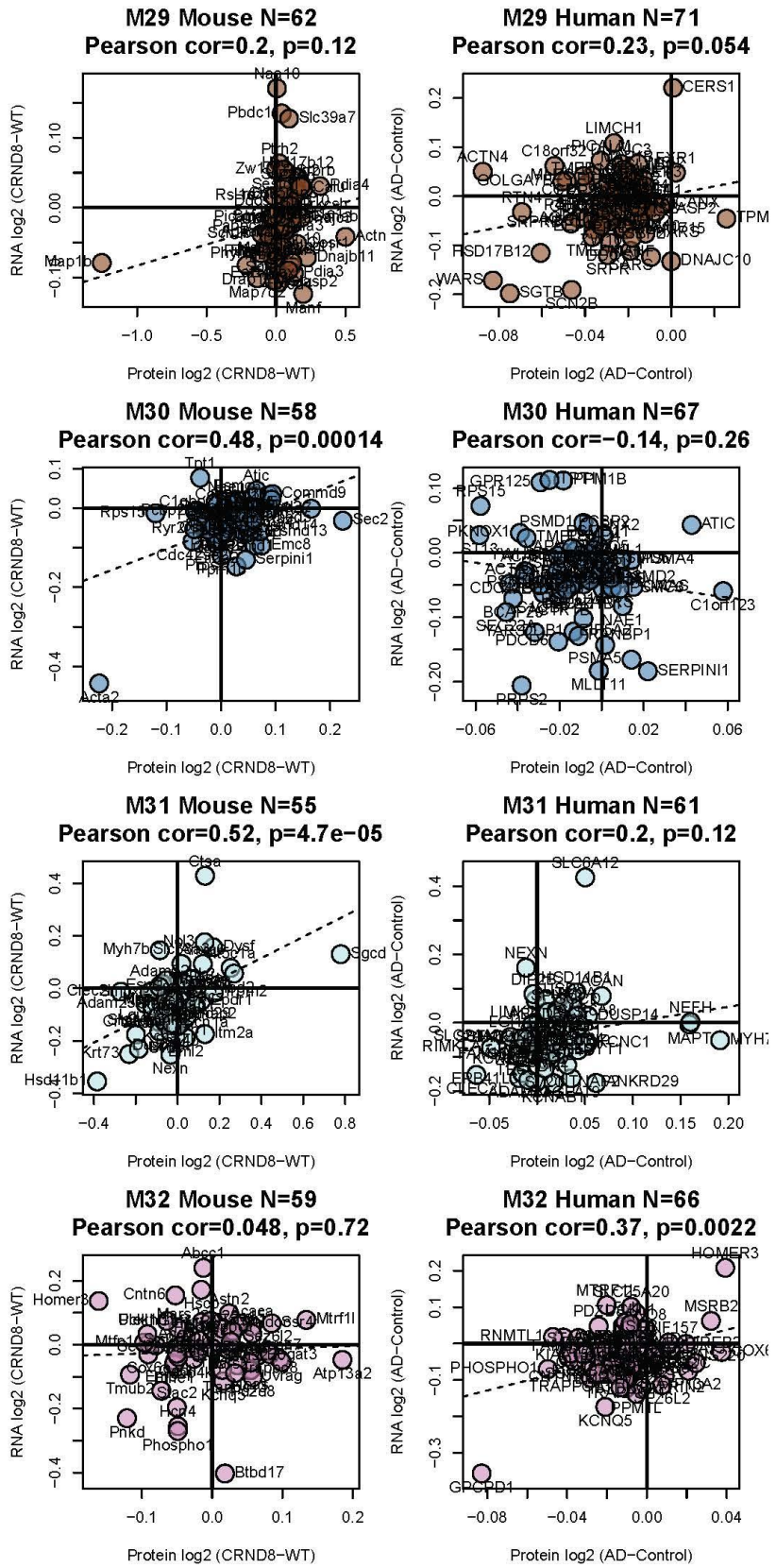

Figure S5 (cont.). Protein-RNA effect size correlation varies in mouse and human for all 44 consensus brain modules.

1658

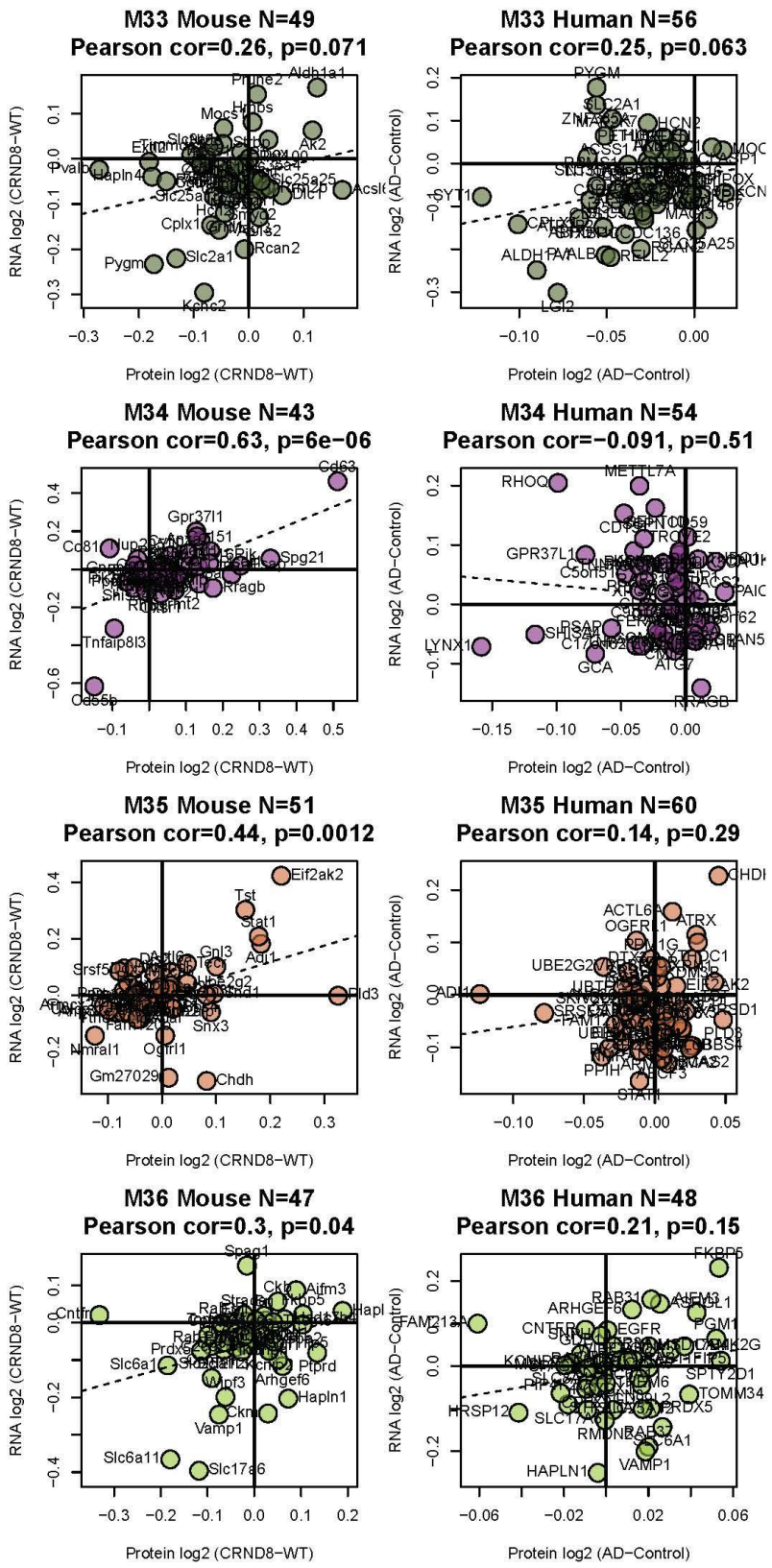

Figure S5 (cont.). Protein-RNA effect size correlation varies in mouse and human for all 44 consensus brain modules.

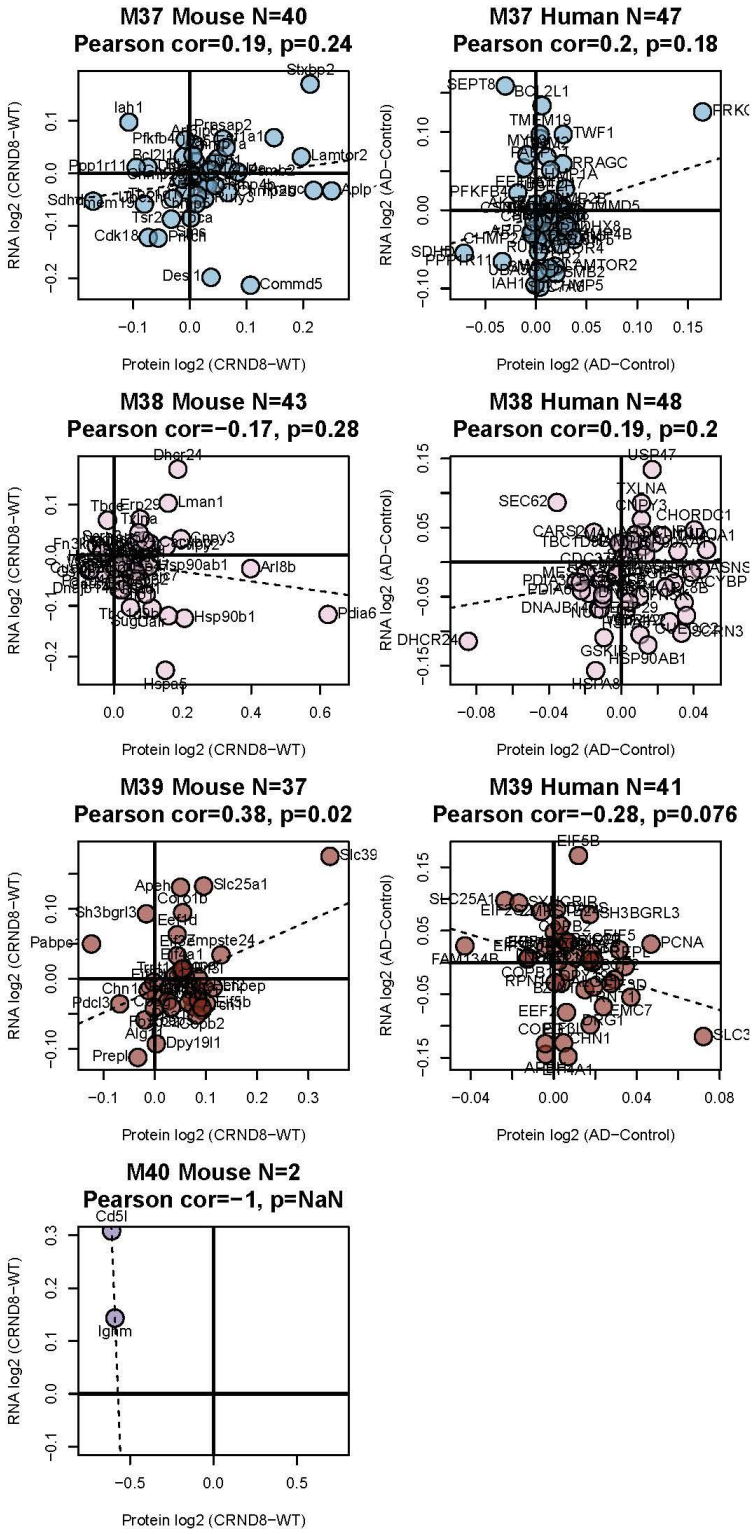

Figure S5 (cont.). Protein-RNA effect size correlation varies in mouse and human for all 44 consensus brain modules.

1660

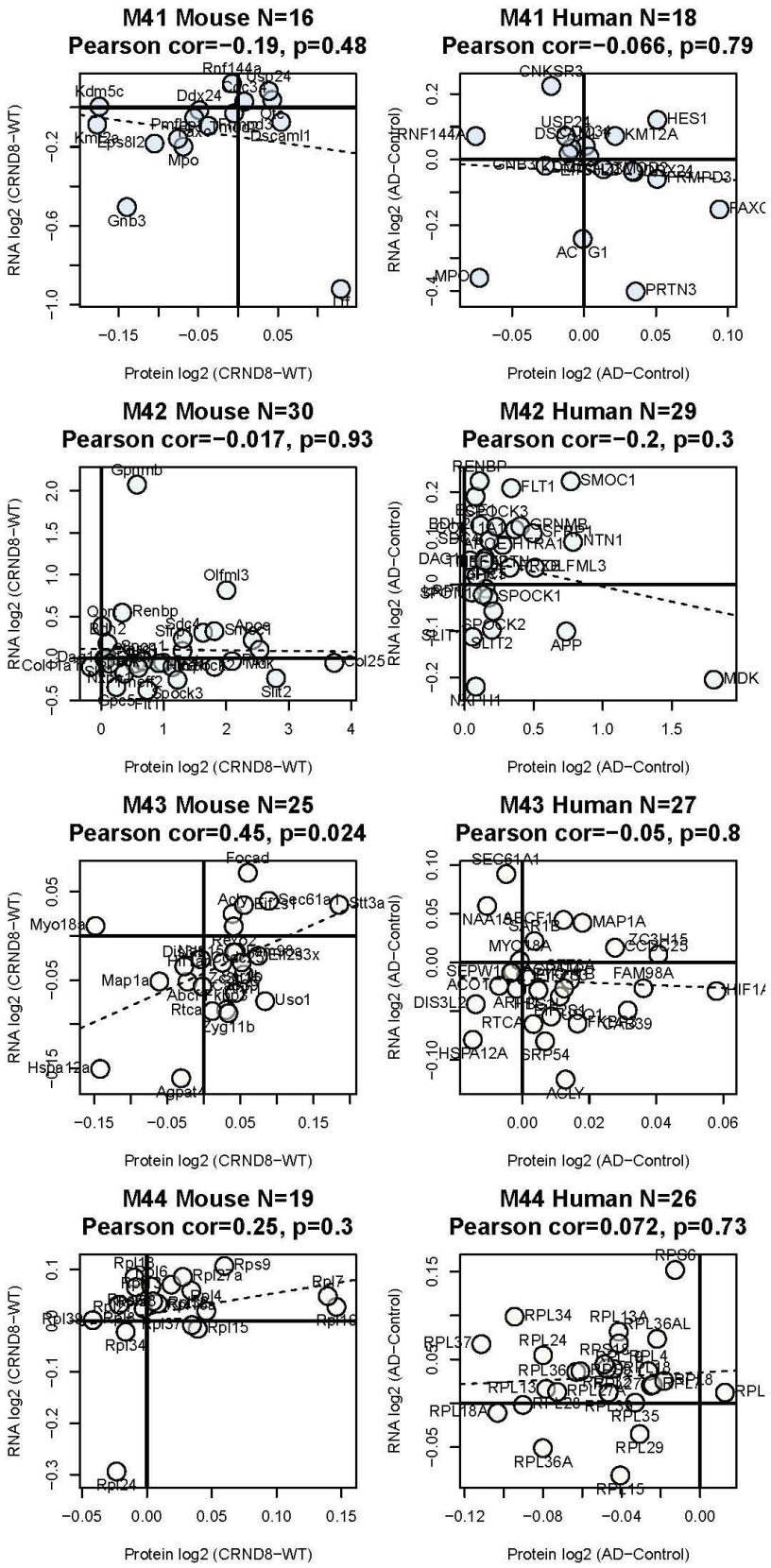

Figure S5 (cont.). Protein-RNA effect size correlation varies in mouse and human for all 44 consensus brain modules.

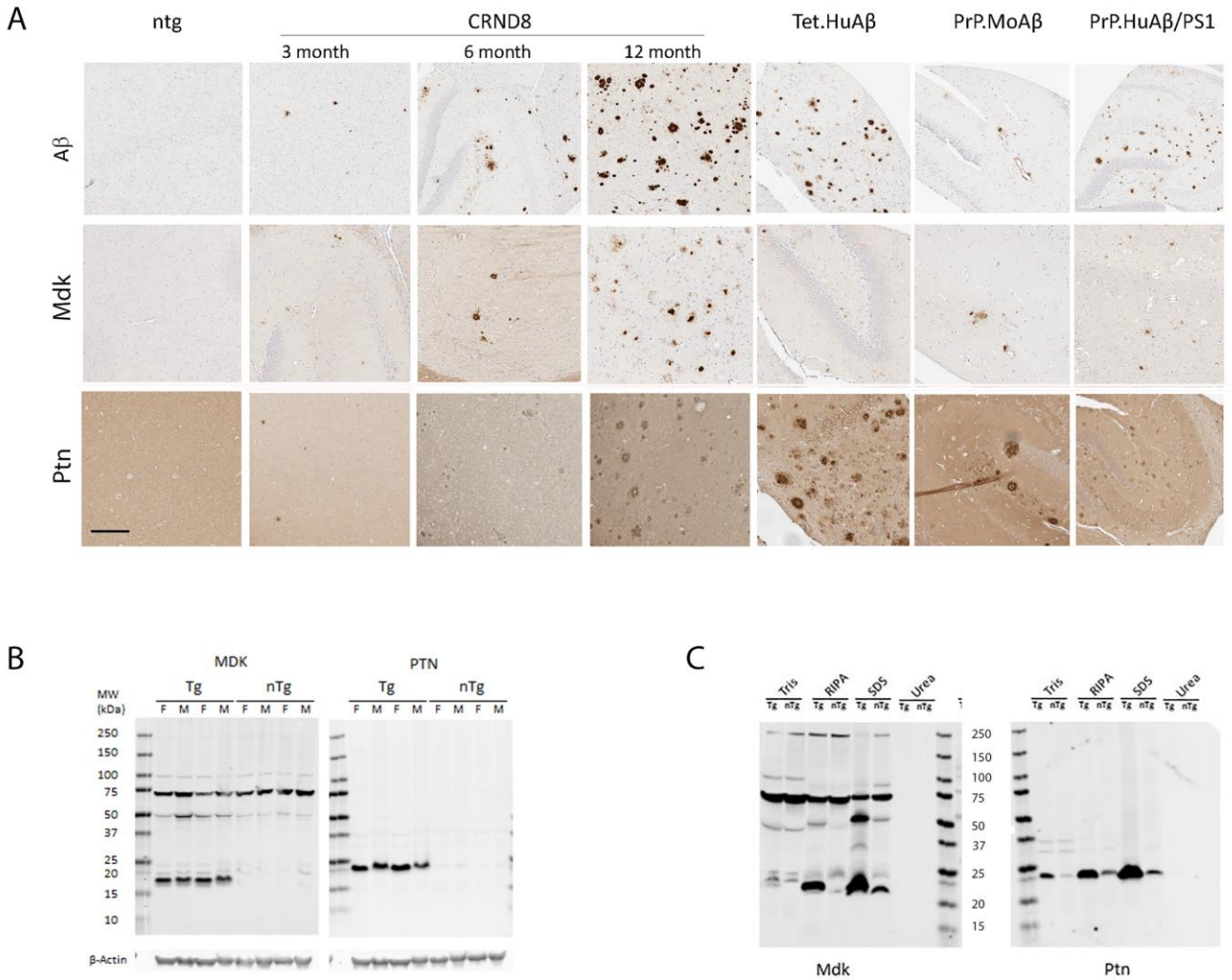

Figure S6. Mdk and Ptn colocalization with amyloid is age dependent, occurs in various AD transgenic mouse models, and accumulation does not alter overall solubility.

A

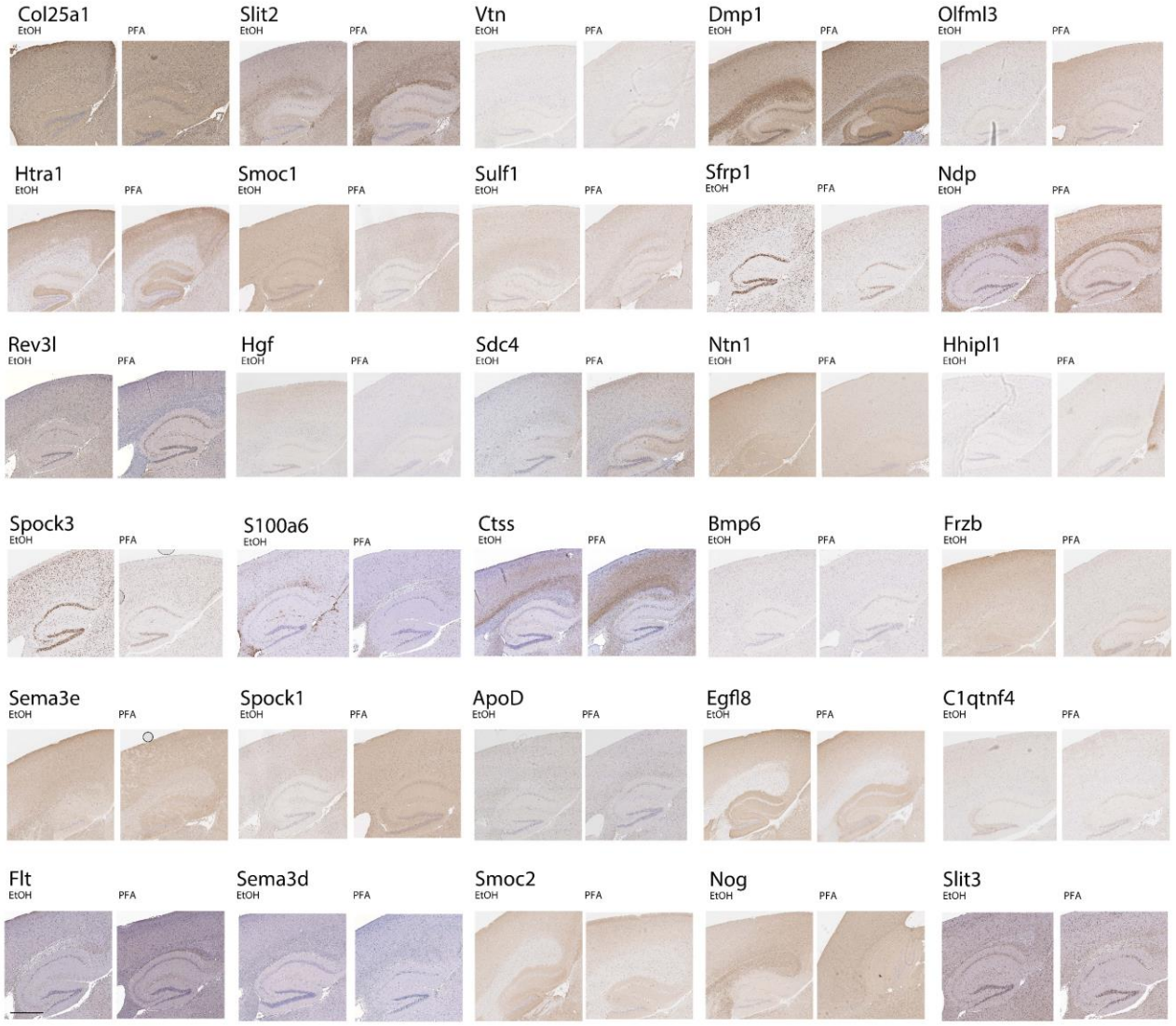

Figure S7A. Non-Tg staining, fixation effects, co-localization, and astrocyte staining.

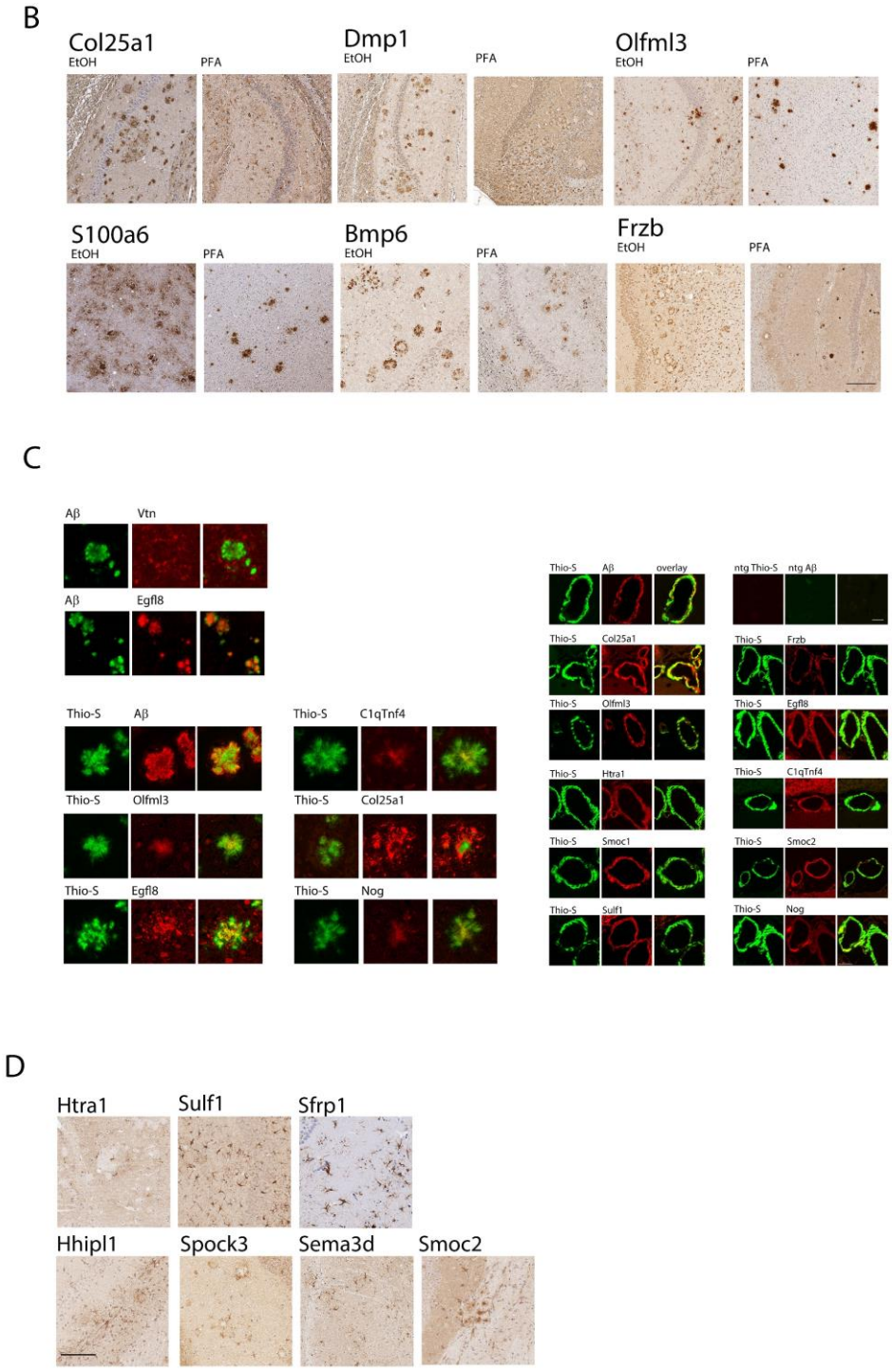

Figure S7B-D. non-Tg staining, fixation effects, co-localization, and astrocyte staining.

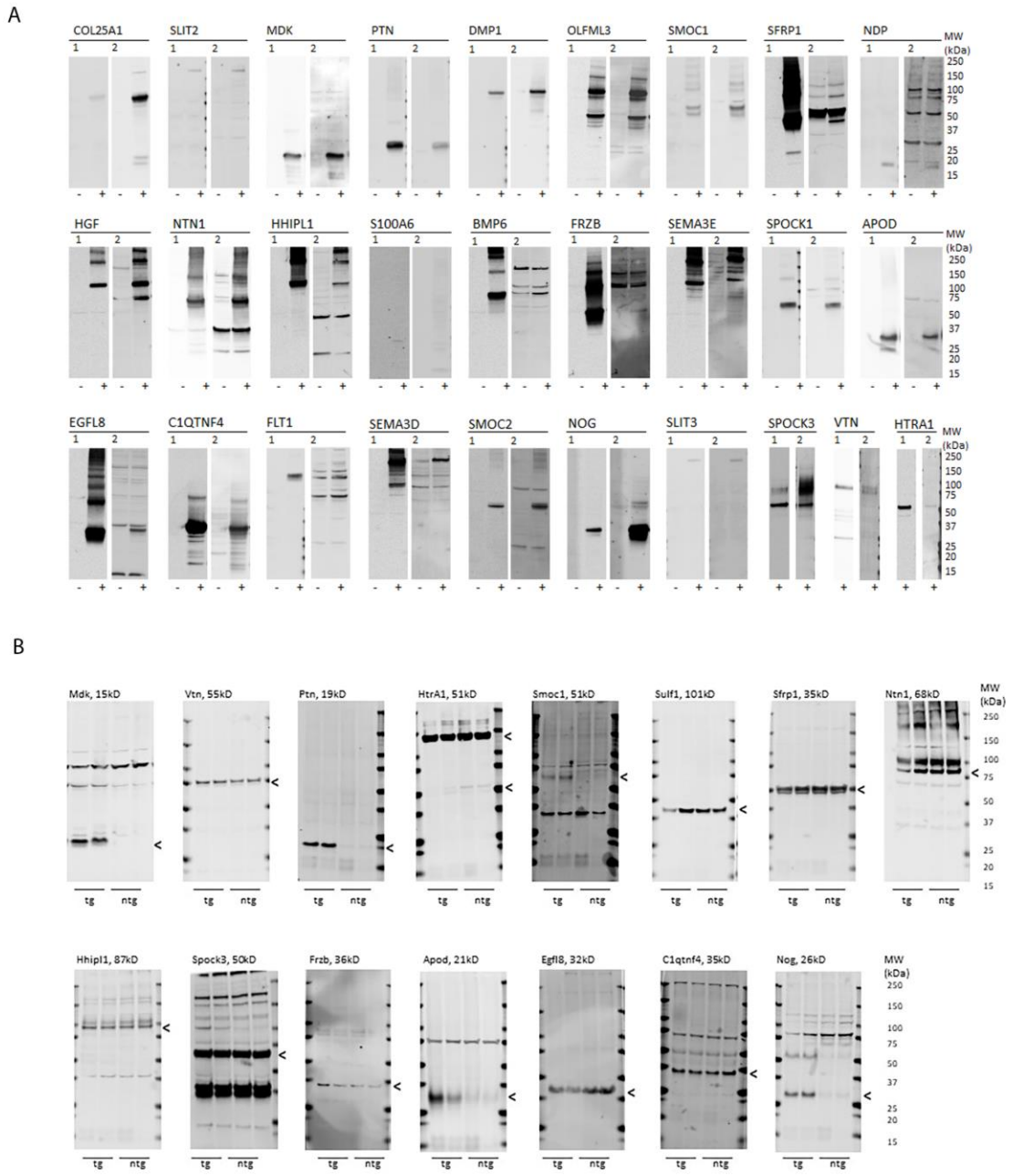

Figure S8. Antibody validation studies and additional DEPS validated by Western blotting.

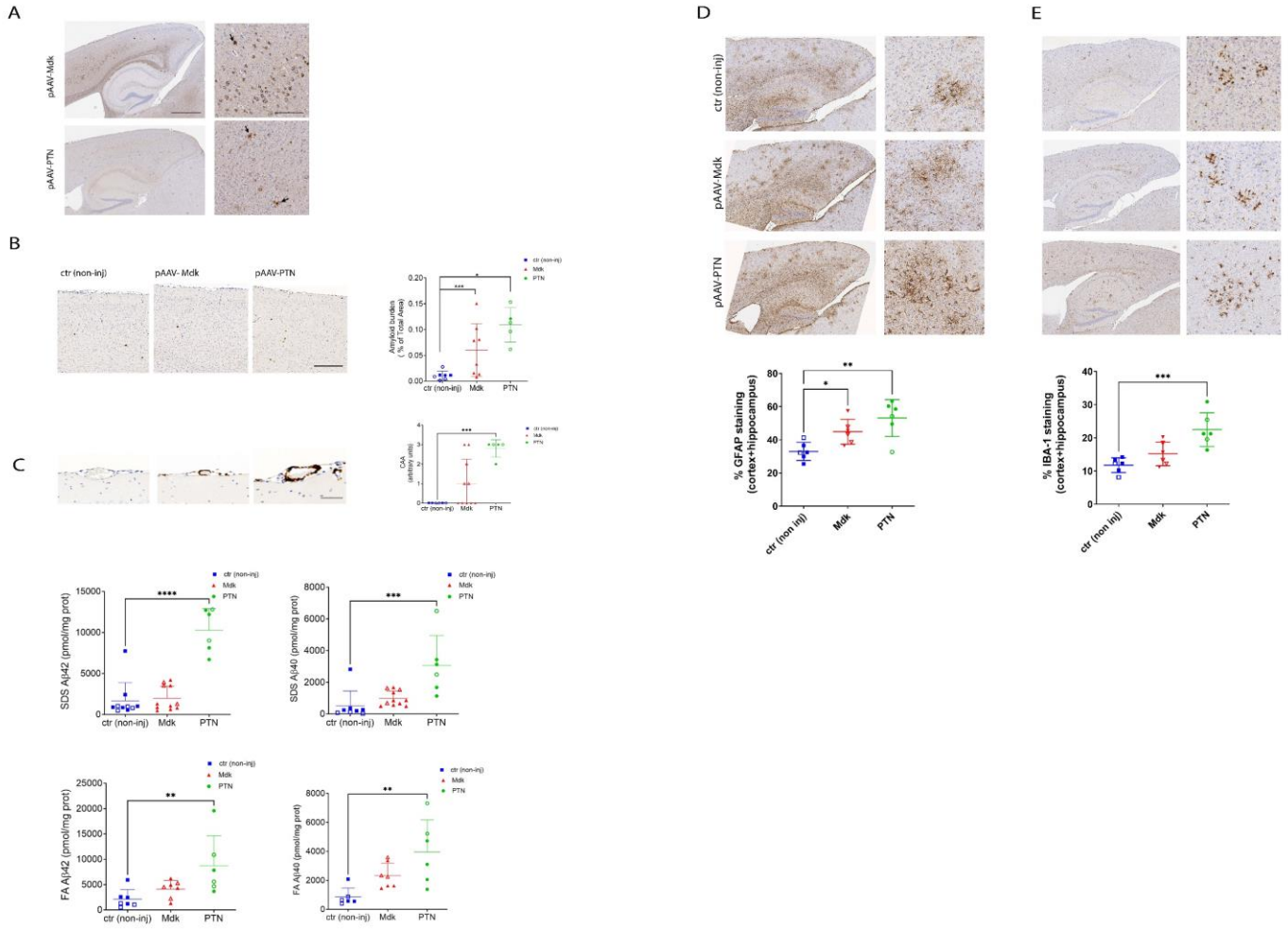

Figure S9. Midkine and Pleiotrophin overexpression increase formation of Aβ amyloid deposition and CAA in 3M CRND8 mice and 6M mouse data on gliosis.

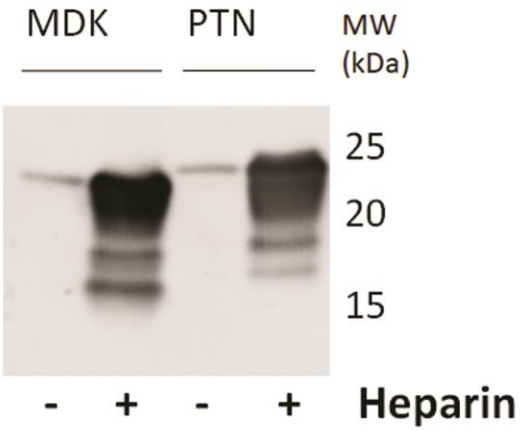

Figure S10. Mdk and PTN interact with heparin.

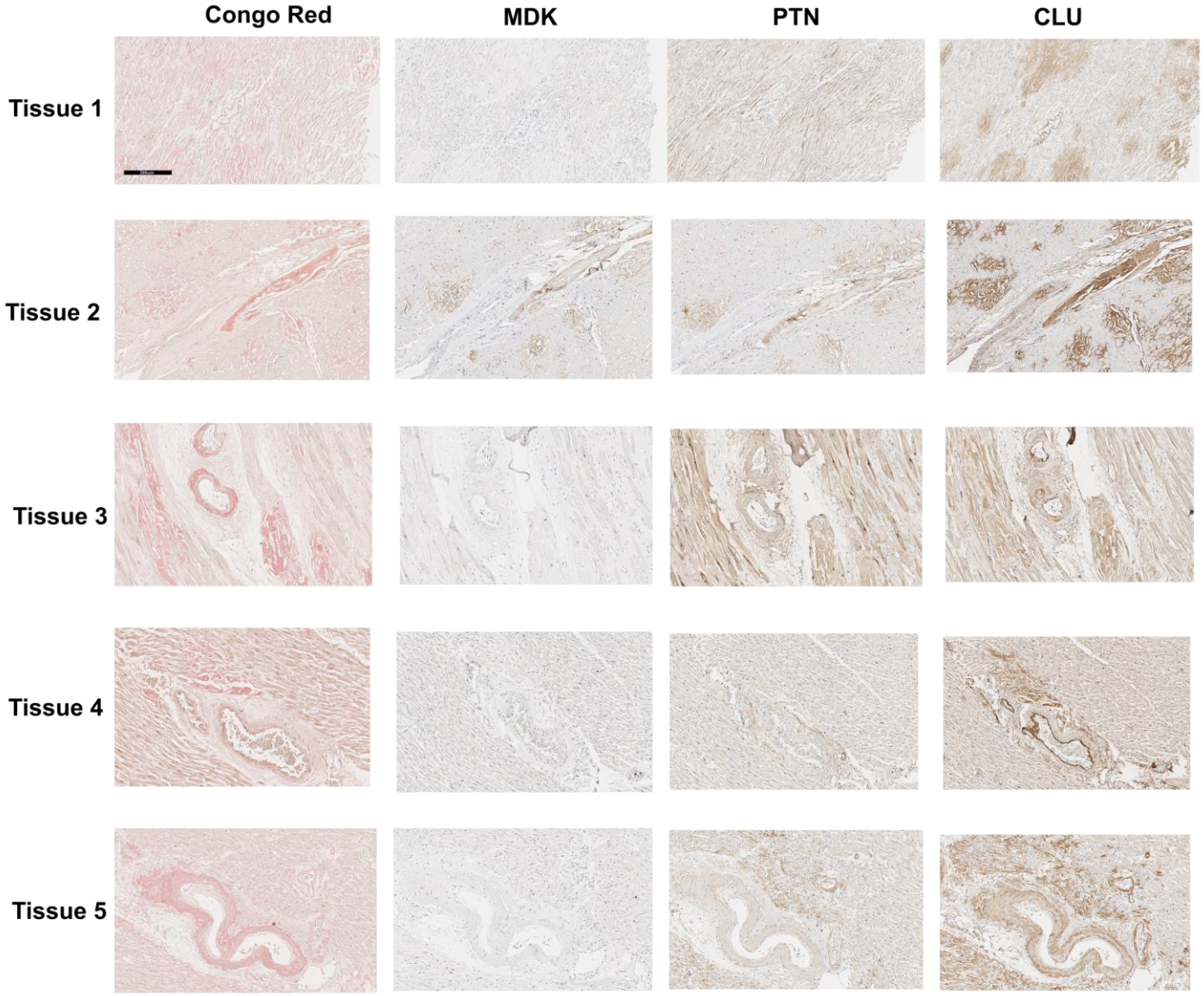

Figure S11. Human heart tissues stained with Congo red, MDK, PTN and CLU.

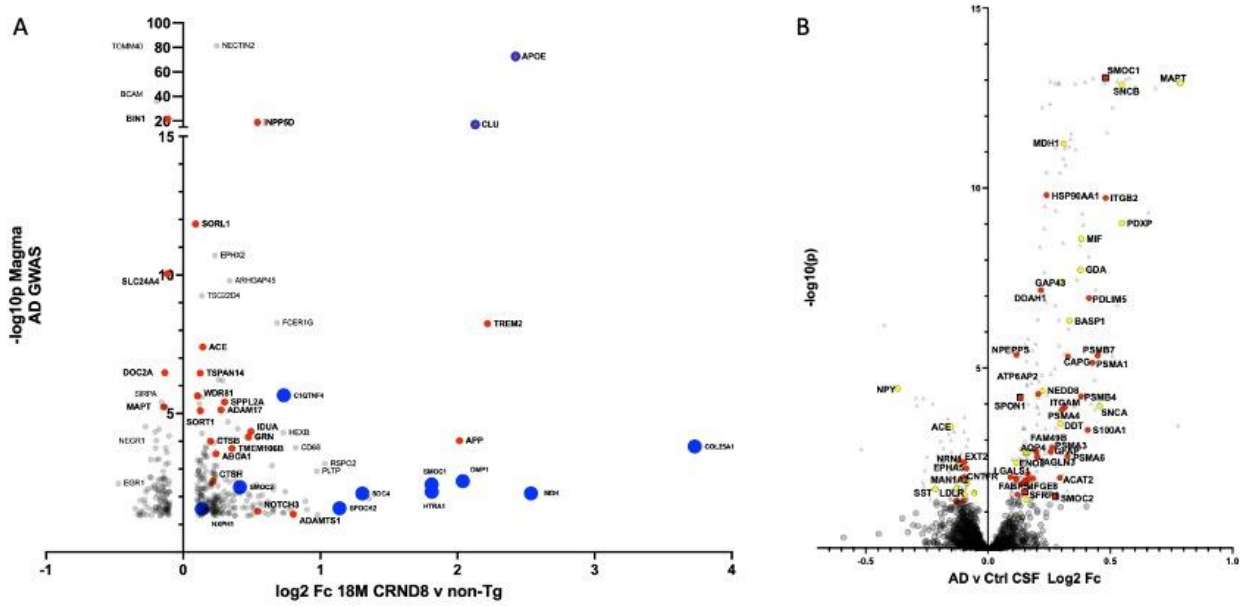

Figure S12. Contextualization of CRND8 18M proteome by integration with AD GWAS MAGMA p values and AD CSF proteomic changes

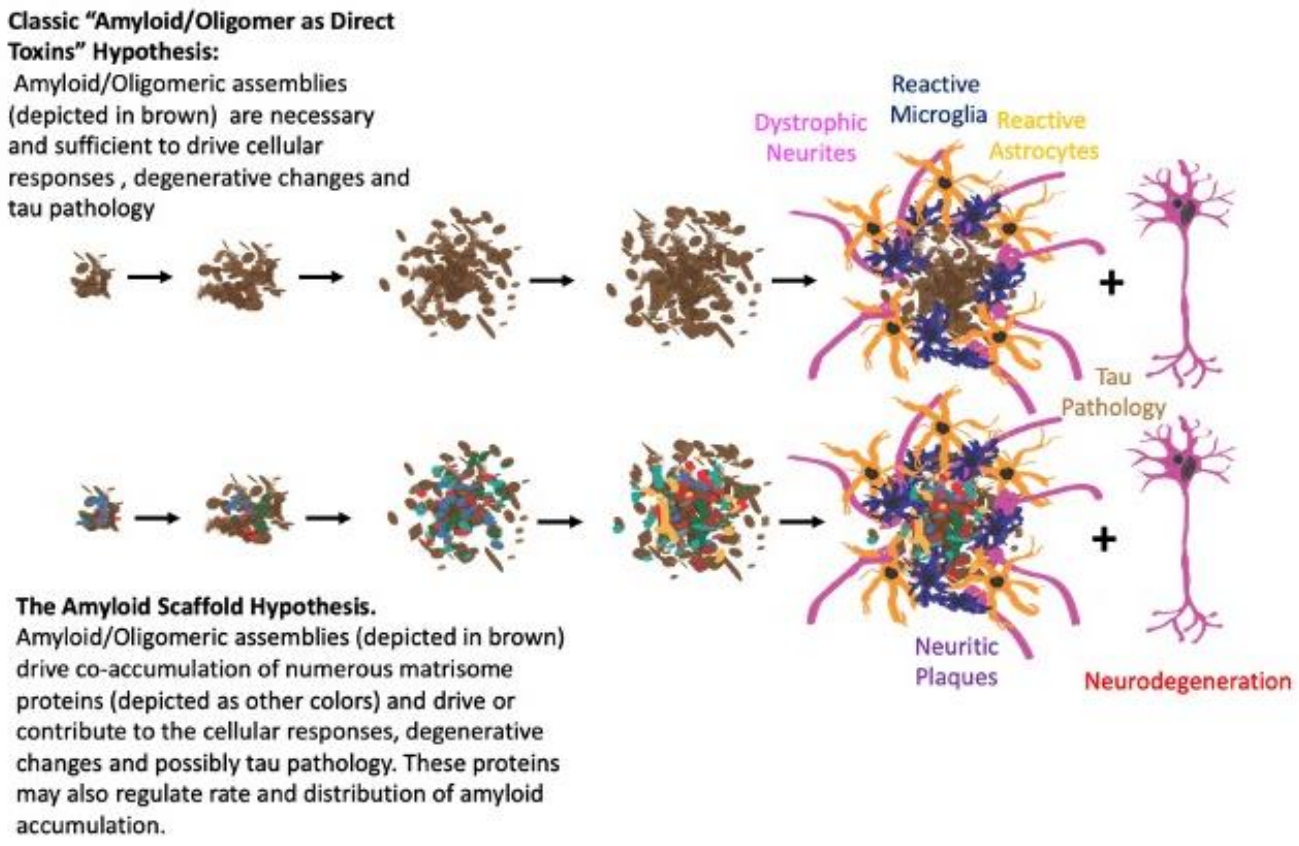

Figure S13. A schematic illustrating the amyloid scaffold hypothesis.